Hydrodynamic Design Optimization and Wave Tank Testing of a Self-Reacting Two-Body Wave Energy Converter

Dillon Martin

Thesis submitted to the faculty of the Virginia Polytechnic Institute and State University
in partial fulfillment of the requirements for the degree of

Master of Science
In
Mechanical Engineering

Lei Zuo, Chair
Robert G. Parker
Danesh K. Tafti

October 3rd, 2017
Blacksburg, VA

Keywords: ocean wave energy harvesting, wave energy converter, point absorber, two-body, hydrodynamics, power optimization, shape optimization

Hydrodynamic Design Optimization and Wave Tank Testing of a Self-Reacting Two-Body Wave Energy Converter

Dillon Martin

ABSTRACT

As worldwide energy consumption continues to increase, so does the demand for renewable energy sources. The total available wave energy resource for the United States alone is 2,640 TWh/yr; nearly two thirds of the 4,000 TWh of electricity used in the United States each year. It is estimated that nearly half of that available energy is recoverable through wave energy conversion techniques. In this thesis, a two-body 'point absorber' type wave energy converter with a mechanical power-takeoff is investigated. The two-body wave energy converter extracts energy through the relative motion of a floating buoy and a neutrally buoyant submerged body. Using a linear frequency-domain model, analytical solutions of the optimal power and the corresponding power-takeoff components are derived for the two-body wave energy converter. Using these solutions, a case study is conducted to investigate the influence of the submerged body size on the absorbed power of the device in regular and irregular waves. Here it is found that an optimal mass ratio between the submerged body and floating buoy exists where the device will achieve resonance. Furthermore, a case study to investigate the influence of the submerged body shape on the absorbed power is conducted using a time-domain numerical model. Here it is found that the submerged body should be designed to reduce the effects of drag, but to maintain relatively large hydrodynamic added mass and excitation force. To validate the analytical and numerical models, a 1/30th scale model of a two-body wave energy converter is tested in a wave tank. The results of the wave tank tests show that the two-body wave energy converter can absorb nearly twice the energy of a single-body 'point absorber' type wave energy converter.

Hydrodynamic Design Optimization and Wave Tank Testing of a Self-Reacting Two-Body Wave Energy Converter

Dillon Martin

GENERAL AUDIENCE ABSTRACT

As worldwide energy consumption continues to increase, so does the demand for renewable energy sources. The total available wave energy resource for the United States alone is 2,640 TWh/yr; nearly two thirds of the 4,000 TWh of electricity used in the United States each year. It is estimated that nearly half of that available energy is recoverable through wave energy conversion techniques. By absorbing the motion of a wave, wave energy converters can turn that energy into useful electricity. A single-body 'point absorber' type wave energy converter consists of a floating buoy connected to the seabed by a mechanism called the power-takeoff. The power-takeoff converts the up and down motion of the floating buoy into rotation. A generator is connected to the power-takeoff, which produces useful electricity from the rotation. Issues with the size of the floating buoy, as well as connecting the floating buoy to the seabed, make this design economically impractical. Instead of connecting the floating buoy to the seabed, the floating buoy can be connected to an additional submerged body. In this thesis, optimization strategies were employed on the size and shape of the submerged body to determine theoretical power limits. Here it is found that an optimal mass ratio between the submerged body and floating buoy exists for a given wave profile. It is also found that the optimal shape of the submerged body is long cylindrical body, having a small surface area normal to the motion. A scale model experiment of a two-body wave energy converter was conducted to validate our theoretical models. The results of this experiment are in good agreement with the models, showing that an optimal mass ratio exists for a given wave profile, and that the two-body wave energy converter can absorb nearly twice the energy of a single-body 'point absorber' type wave energy converter.

Acknowledgements

First, I would like to thank my advisor, Dr. Lei Zuo, for his support and guidance throughout my graduate career. His encouragement and instruction showed me what it means to perform meaningful research. I have learned a lot from my studies under him and will carry this knowledge throughout my entire career.

Secondly, I would like to thank my lab partners; Changwei Liang, Xiaofan Li, Adam Wise, Eric Dupius, David Kennedy, Chien-An Chen, and Jedhathai Bootanom. You have all provided help and support throughout my time here and have been indispensable resources.

I would like to thank Dr. Parker and Dr. Tafti for serving on my thesis committee. Your time reviewing this thesis is greatly appreciated.

I would like to thank the U.S. Department of Energy and the National Science Foundation for their financial support, as well as the staff at the University of Maine's Alfond W^2 Ocean Engineering Lab for their help and support of our experimental testing.

I would like to thank the staff members of the Energy Harvesting and Mechatronics Research Lab, Lauren Mills and Mandy McCoy. Your help and support is greatly appreciated.

I would like to thank my friends outside of the lab; John Gill, Ben Brainard, Jami Forrest, Travis Phillips, and Jordan Frate. You guys have kept me grounded throughout my time here.

I would like to thank my girlfriend, Jennifer Cobb, and our dogs, Maisie and Harper, for their love and support. You have been my lifeline. From bringing me food and coffee, to staying up late with me writing, you have supported me and I couldn't have written this without you.

Finally, I would like to thank my parents Joseph and Diann Martin, and my siblings Corbin and Jordan Martin, for their love and support. Though I don't say it enough, my parents have provided me countless opportunities throughout my entire life and provided their support in whichever endeavor I have chosen to take, and for that, I am truly grateful. I love you all.

Table of Contents

List of Figures

List of Tables

1. Introduction

1.1 Wave Energy

As worldwide energy consumption continues to increase, so has the need for sustainable energy sources. With concerns over climate change [1] and the limited source of supply, the reliance on fossil fuels has become less desirable. Renewable power generation saw its largest annual increase ever in 2016, increasing by nearly 9% from 2015, when renewables contributed 23.7% of the total global energy capacity [2]. With the increasing demand for renewable energy as a sustainable energy source, research and development of varying technologies has been conducted to increase the capacity factor, the ratio of actual electrical energy to the maximum possible energy, for multiple renewable resources. The capacity factor for multiple renewable energy sources can be found in Table 1.1.

Table 1.1 Capacity factors for renewable utility scale generators [3]

Renewable Resource	Capacity Factor
Hydropower	38.0%
Wind	34.7%
Solar PV	27.2%
Geothermal	74.2%
Landfill Gas/Municipal Waste	70.7%
Other Biomass (including wood)	46.7%

A renewable resource that is typically overlooked is ocean wave energy. While it dates back to 1799 [4], wave energy technology development hasn't taken off like other renewable resources have. A renewed interest in 1973, in response to the oil crisis, spiked funding in northern European countries, however, as oil prices declined in the 1980s, so did the funding. Now, as the publics support of funding renewable energy technologies grows, so have the opportunities for wave energy development.

Ocean waves are the result of wind blowing over the ocean, and are thus an indirect form of solar energy and the rotational energy of the earth. While the capacity factor for wave energy is smaller than wind energy, around 30% [5], the energy density of ocean waves is much higher than wind. The theoretical potential for worldwide wave energy

capture is 29,500 TWh/year [6]. The total available wave energy resource for the United States alone is 2,640 TWh/yr; nearly two thirds of the 4,000 TWh of electricity used in the United States each year [7]. It is estimated that nearly half of that available energy is recoverable through wave energy conversion techniques [7]. Figure 1.1 shows the estimation of wave power levels along the coast. As roughly 40% of the world's population lives within 20km of the coast [6], the usefulness of this energy source is abundant.

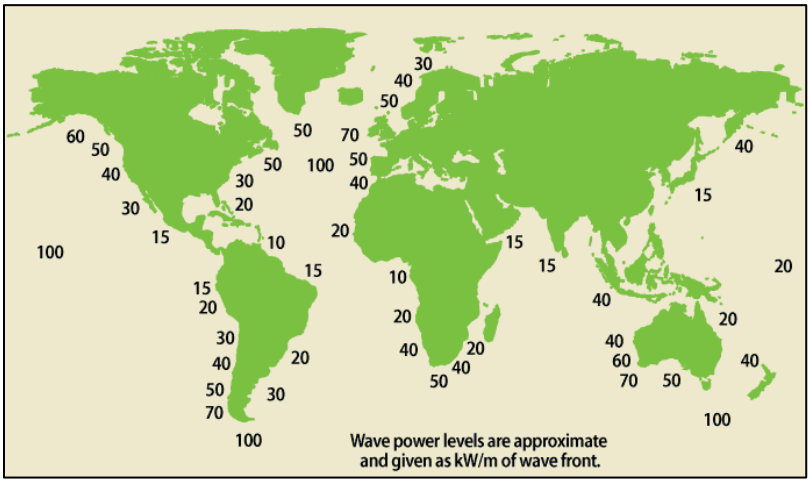

Figure 1.1 Estimation of global distribution of coastal wave power [8]

1.2 Wave Energy Conversion

The first record of wave energy conversion is dated back to July, 12th 1799, when a father and son named Girard filed the first-ever patent for a wave energy device [4]. "The motion and successive inequality of waves, which after having been elevated like mountains fall away in the following instant, take into their motion all bodies which float on them. The enormous mass of a ship of the line, which no other known force is capable of lifting, responds to the slightest wave motions. If for a moment one imagines this vessel to be suspended from the end of a lever, one has conceived the idea of the most powerful machine which has ever existed" [4]. While no outcome seems to have come from this patent, it's innovation has been the influence of many others. In 1889, Thomas Edison proposed the idea of using moored dynamos powered by waves to provide warning lights [9]. Like the Girards', nothing amounted to Edison's idea. It wasn't until the early 1970s before wave energy development began to take off. The 1973 oil crisis, brought upon by the oil embargo in retaliation to the Yom Kippur War [10], brought the public's attention to the increasing price of energy and their reliance on oil from the middle-east. In response

to the oil crisis, many countries began funding research into renewable energies. In particular, the countries surrounding the North Sea (UK, Norway) initiated extensive research into wave energy [11]. Since then, thousands of patents have been filed as wave energy converters (WECs). A classification method proposed by António Falcão [12], shown in Figure 1.2, categorizes WECs into three main categories based on working principle; overtopping, oscillating water column, and oscillating bodies. Each of the three WEC classifications are further defined by their operational style (fixed, floating or submerged).

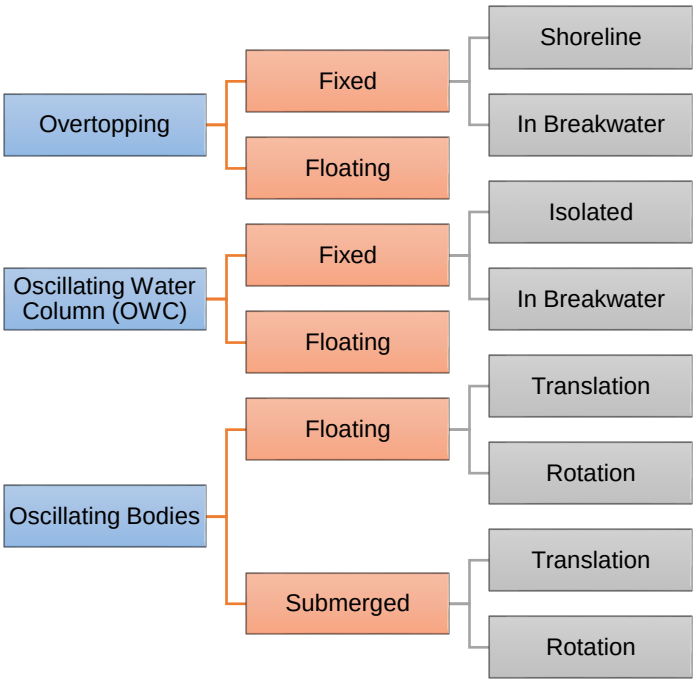

Figure 1.2 WEC classification methodology [12]

Various power takeoff (PTO) designs, which is the mechanism that transmits the primary input power source of the device, are used in each WEC configuration. Falcão describes the PTO as "the single most important element in wave energy technology" [12], as it is responsible for converting the wave energy into usable electricity. The following sections detail the three main categories of WECs and typical PTOs used for each.

1.2.1 Overtopping Devices

The overtopping device captures water in a reservoir through the waves overtopping phenomenon at the wave crest. The incident wave overtops a sloped wall or ramp and fills a reservoir with water at a higher level than the surrounding sea. By allowing the water to

fall through the reservoir into a set of hydraulic turbines, the potential energy of the water is converted into electricity. Overtopping devices can be fixed into the shoreline/breakwater, or can be floating. An example of a fixed shoreline device is the Tapchan (Tapered Channel Waver Power Devices), shown in Figure 1.3, which was developed and built in Norway in the 1980s [14].

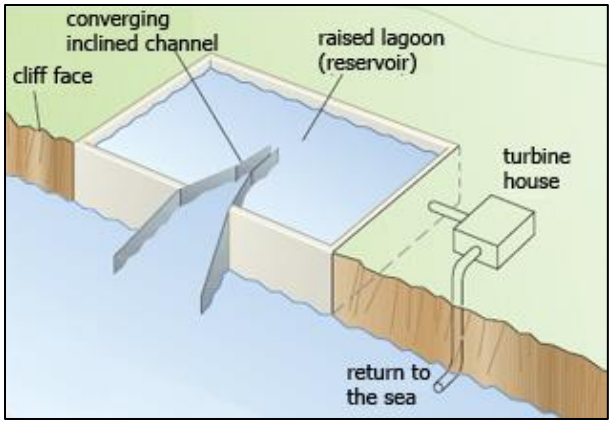

Figure 1.3 Schematic representation of the Tapchan [14]

1.2.2 Oscillating Water Columns

The oscillating water column (OWC) comprises of a partially submerged structure with an air chamber and a bi-directional turbine. The structure is open below the water free surface, trapping air in the chamber. As the wave crest passes through the OWC, the water in the column rises, compressing the air. The compressed air goes through the bi-directional turbine, generating electricity. As the water level falls, air re-enters through the turbine. Typically, a Wells Turbine, developed in the late 1970s by Alan Wells, is used as the bi-directional turbine [15]. Like the overtopping device, the OWC can be fixed into the shoreline/breakwater, or can be floating. Figure 1.4 shows a schematic of a fixed OWC.

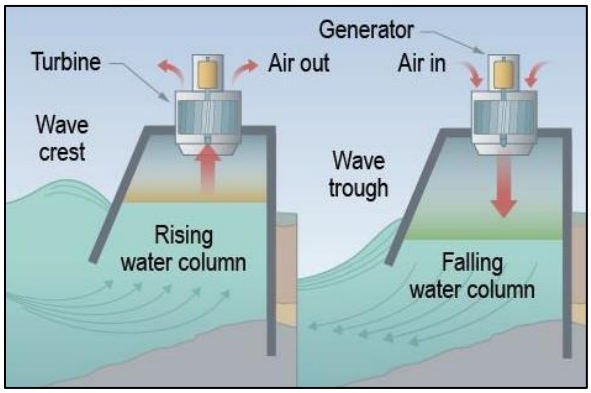

Figure 1.4 Schematic representation of an OWC [16]

1.2.3 Oscillating Body Devices

Oscillating body devices encompass a large variety of offshore wave energy converters. While their design & dynamics may differ, their main working principle is the same, which is to generate electricity through the relative translational, or rotational, motion induced by the wave. Different from the previous two wave energy converter classifications, which used turbines as the PTO, oscillating body devices use various PTOs, including electromagnetic, hydroelectric, mechanical and pneumatic systems. The most common types of oscillating body wave energy converters are heaving systems, the simplest of which is a single-body point absorber [17]. A single-body point absorber consists of a heaving buoy reacting against a fixed reference (the seabed), as shown in Figure 1.5. Typically, the buoys horizontal dimensions are much smaller than the wavelength. It can be viewed as a 'point' along a waves oscillation, hence the name point absorber [17]. Difficulties arise when implementing these devices in more energetic waves, as the size of the buoy must be quite large to achieve resonance in regular waves and distance between the buoy and the seabed becomes challenging. To overcome these challenges, two-body point absorbers were developed, where the energy is captured through the relative motion of the two bodies [18]. Falnes found two advantages for the two-body WEC, the first of which is the possibility of an increased equivalent excitation force on the WEC, which would produce more power, and the second of which is the possibility of an additional resonance frequency [18]. The Reference Model Project (RMP), sponsored by the U.S. Department of Energy (DOE), was an effort to develop and benchmark varying WECs [19]. Reference Model 3, which is a two-body point absorber inspired by the Ocean Power Technology's PowerBuoy [20], uses a heave plate to maintain a relatively stationary position (producing a reaction force similar to the ocean floor). While this design is simple to manufacture, it does not utilize the additional resonance frequency, as the drag on the plate would overdamp the plates response. Another example of a two-body point absorber that does take advantage of the two-body dynamics is the Wavebob [21], which uses a neutrally buoyant cylindrical tank with tapered ends as a reaction mass.

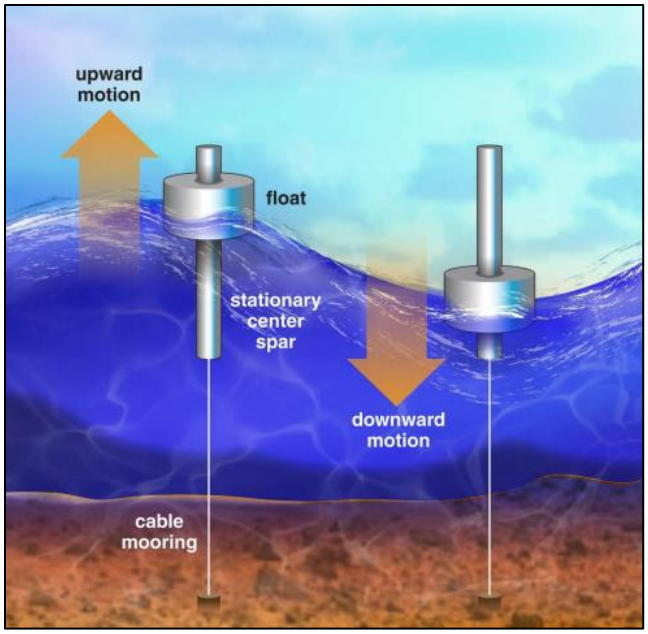

Figure 1.5 Schematic representation of a heaving point absorber [22]

1.3 Objectives

The overall objective of this thesis is to investigate and optimize configurations of the reacting body for a resonant two-body WEC. In order to address this, three objectives must be met. First, through the use of frequency domain analysis, the dynamics of a single-body point absorber and two-body point absorber are analyzed and their performance are compared. Here, the size of the reacting body for the two-body system is studied and optimized to achieve resonance and improve energy absorption. The second objective is to optimize the shape of the submerged body through time domain analysis. A more comprehensive non-linear dynamic model can be studied through the time domain and the shape of the body will have more of an impact on the energy absorption. Lastly, an experimental scaled model is used to compare a single-body WEC to a two-body WEC in hopes of validating our models. The scaled model experiments will be advantageous in the design and deployment of a full scale model.

1.4 Organization

The organization of this thesis is as follows. Chapter 2 will present the theoretical background of wave energy and the hydrodynamics on the wave energy converters. Chapter 3 will present the dynamics and design of a single body point absorber and two

two-body point absorbers designs, as well as frequency domain analysis of each device. Chapter 4 will present the time-domain analysis of the varying two-body point absorbers to determine the optimal shape and size for a certain wave profile. Chapter 5 will present the wave tank experimental setup and results. Chapter 6 concludes the thesis and outlines the future work to be completed.

2. Theoretical Background

This chapter discusses the theoretical background needed to understand the modeling of ocean waves and their interaction with floating devices. The chapter has four parts, covering; the basic properties of waves, the hydrodynamics involved in modelling ocean waves, the interaction between a floating body and the wave, and the software tool used to model the wave-body interaction.

2.1 Wave Properties

2.1.1 Coordinate System

The motion of an object floating in water is defined by six degrees of freedom; the translation of the object about the axes x, y and z, and the rotation about those axes. As shown in Figure 2.1, the translational motions can be defined as $surge\ (x)$, $sway\ (y)$ and $heave\ (z)$, and the rotations as $roll\ (x)$, $pitch\ (y)$ and $yaw\ (z)$. In this coordinate system, the incident wave direction will be in the positive x – direction.

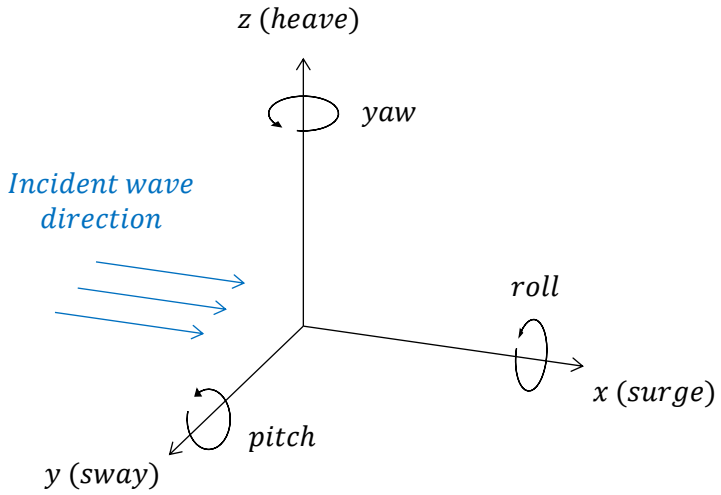

Figure 2.1 Coordinate system of WEC

2.1.2 Regular Waves

Regular surface waves are progressive waves that are caused by wind blowing over the ocean for long periods of time over a large area. Regular waves are considered two-dimensional, propagating along x with time, t. The surface elevation of a regular wave, η, can be defined as a harmonic function:

$$\eta(t,x) = \frac{H}{2}\cos(kx - \omega t) \tag{2-1}$$

where H is the wave height, k is the wave number, which is defined as:

$$k = \frac{2\pi}{\lambda} \tag{2-2}$$

and ω is the wave frequency, which is derived from the linear dispersion relation:

$$\omega^2 = gk\tanh(kh) \tag{2-3}$$

where g is the acceleration due to gravity and h is the water depth. Figure 2.2 represents a regular surface wave with the physical descriptions just described. Here, z, is defined as the water level, where $z = 0$ is the defined as the still water level.

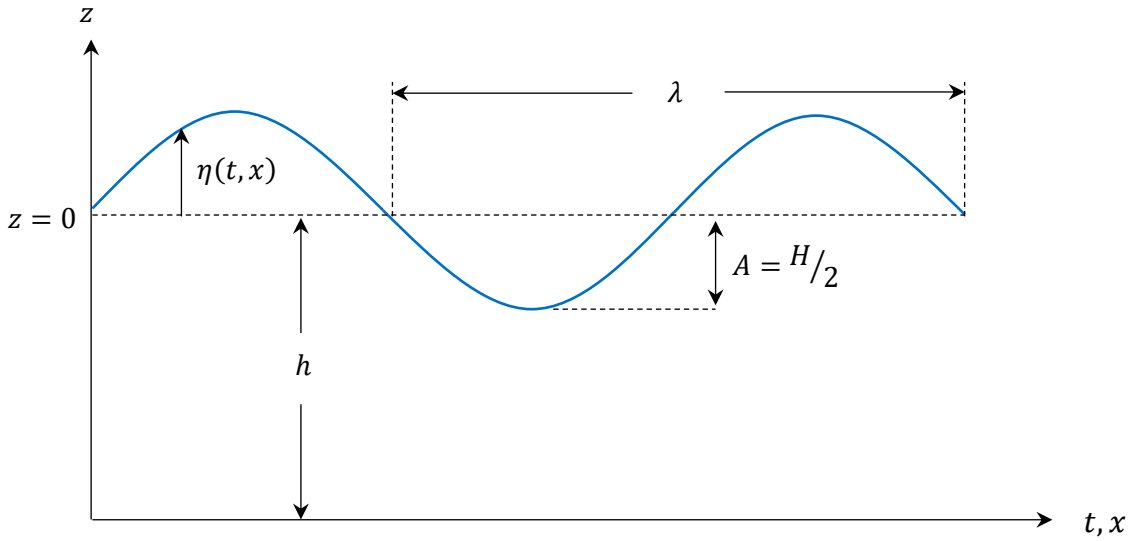

Figure 2.2 Regular wave surface profile

2.1.3 Irregular Waves

Real sea waves are typically very irregular due to the irregularity of the wind energy. These irregular sea states can be seen as a superposition of multiple regular harmonic waves, each with their own set of wave height, wave period, wavelength and wave heading (the waves may not follow along $y = 0$, as was assumed in the previous section). To analyze irregular sea states, this superposition of regular waves may be characterized in the frequency domain by a wave spectrum. One of the simplest wave spectra used is the Pierson-Moskowitz spectrum, which describes a fully develop sea [23]. A fully developed sea assumes after a steady blow of wind over a long period of time (roughly 10,000 periods), over a large area (roughly 5,000 wavelengths), the wind transfers its maximum

energy to the waves. The Pierson-Moskowitz spectrum is a one parameter spectrum and can be defined as:

$$S(\omega) = \frac{\alpha g^2}{(2\pi)^4} {H_s}^2 \frac{1}{f^5} exp\left\{-\frac{5}{4}\left(\frac{f_p}{f}\right)^4\right\} \tag{2-4}$$

where f is frequency, H_s is the significant wave height, and f_p is the peak frequency. The significant wave height is defined as the average height of the highest one-third waves in a sea state [24]. It can be calculated using:

$$H_s = 4\sqrt{m_0} \tag{2-5}$$

where m_0 is the total variance of the wave record, which is the sum of the variance of the individual spectral components:

$$m_0 = \sum_{\omega_l}^{\omega_h} S(\omega) d\omega \tag{2-6}$$

The α is typically 0.0081, however to represent it in terms of the wave height, it can be calculated as [25]:

$$\alpha = \frac{{H_s}^2}{16 \int_0^\infty \left[\frac{g^2}{(2\pi)^4} {H_s}^2 f^{-5} exp\left\{-\frac{5}{4}\left(\frac{f_p}{f}\right)^4\right\}\right] df} \tag{2-7}$$

2.2 Hydrodynamics

The two equations that describe the motion of a fluid are the continuity equation, derived from conservation of mass, and the Navier-Stokes equations, derived from conservation of momentum. The Navier-Stokes equations consist of coupled non-linear partial differential equations, making them difficult and time-consuming to solve. Linear wave theory, also known as Airy wave theory, has been extensively used in describing the wave-body interaction [26, 27] and has been validated [28] and experimentally verified [29]. Linear wave theory assumes the interacting fluid is: incompressible, inviscid, and irrotational. Linear wave theory also makes the assumption that the wave elevation, H, is small compared to the wavelength, λ.

Ocean waves can be classified as shallow water waves, intermediate depth waves and deep water waves, depending on the ratio of the wave length, λ, and the water depth, h. Figure 2.3 shows the applicability of various wave theories. For deep water waves, which

is where the WEC will be deployed, linear wave theory is valid up to a wave steepness (ratio of wave height to wavelength) of 1:25.

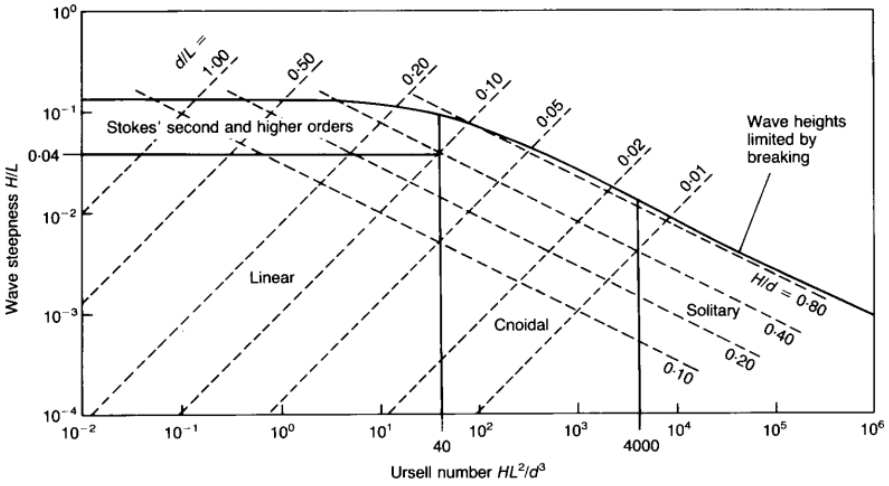

Figure 2.3 Applicability of various wave theories [30].

2.2.1 Continuity Equation

The velocity vector of a fluid particle is defined as: $\vec{V} = [u, v, w]$, where u, v and w are the velocities of the x, y and z coordinates, respectively. For incompressible fluids, the divergence of velocity is zero:

$$\nabla \cdot \vec{V} = \frac{\partial u}{\partial x} + \frac{\partial v}{\partial y} + \frac{\partial w}{\partial z} = 0 \tag{2-8}$$

Since the flow is assumed to be irrotational, which occurs when the cross gradient of the velocity is zero, i.e. $\nabla \times \vec{V} = 0$, the velocity vector can be written as the gradient of the velocity potential, ϕ:

$$\vec{V} = \nabla\phi \tag{2-9}$$

Substituting (2-9) into (2-8) yields the Laplace equation:

$$\nabla^2\phi = \frac{\partial^2\phi}{\partial x^2} + \frac{\partial^2\phi}{\partial y^2} + \frac{\partial^2\phi}{\partial z^2} = 0 \tag{2-10}$$

2.2.2 Navier-Stokes Equations

For inviscid fluids, the Navier-Stokes equations can be simplified into the Euler equations:

$$\nabla\left(\frac{\partial\phi}{\partial t} + \frac{(\nabla\phi)^2}{2} + \frac{p}{\rho} + gz\right) = 0 \tag{2-11}$$

where p is the pressure of the fluid, ρ is the density of the fluid, g is the acceleration due to gravity, and z is the displacement from the free surface of the water $\eta(x, y, t)$. Integrating (2-11) yields the Bernoulli equation:

$$\frac{\partial \phi}{\partial t} + \frac{(\nabla \phi)^2}{2} + \frac{p}{\rho} + gz = c \tag{2-12}$$

Eliminating the high order terms, $(\nabla \phi)^2$, and rearranging results in:

$$p = -\rho \frac{\partial \phi}{\partial t} - \rho g z + c \tag{2-13}$$

The pressure at the free surface, $z = 0$, is the atmospheric pressure (p_{atm}). Solving (2-13) for the static case, when $\frac{\partial \phi}{\partial t} = 0$, results in $c = p_{atm}$. The linearized Bernoulli equation can now be written as:

$$p = -\rho \frac{\partial \phi}{\partial t} - \rho g z + p_{atm} \tag{2-14}$$

The pressure consists of two parts: the hydrostatic part, defined by $-\rho g z$, and the hydrodynamic part, defined by $-\rho \frac{\partial \phi}{\partial t}$. To determine the hydrodynamic pressure, the velocity potential must satisfy two boundary conditions: the kinematic boundary condition and the dynamic boundary condition.

2.2.3 Kinematic Boundary Conditions

At a fixed boundary, the normal velocity of a fluid particle must be equal to zero:

$$\frac{\partial \phi}{\partial n} = 0 \tag{2-15}$$

This is particularly true on the seabed, where:

$$w|_{z=-h} = \left.\frac{\partial \phi}{\partial z}\right|_{z=-h} = 0 \tag{2-16}$$

On the free surface, where $z = \eta(t, x, y)$, the variation of z with respect to time is calculated by the total derivative, due to the indirect dependencies of x and y:

$$\frac{dz}{dt} = \frac{\partial \eta}{\partial t} + \frac{\partial \eta}{\partial x}\frac{dx}{dt} + \frac{\partial \eta}{\partial y}\frac{dy}{dt} \tag{2-17}$$

where:

$$\frac{dx}{dt} = u = \frac{\partial \phi}{\partial x}; \qquad \frac{dy}{dt} = v = \frac{\partial \phi}{\partial y}; \qquad \frac{dz}{dt} = w|_{z=\eta} = \left.\frac{\partial \phi}{\partial z}\right|_{z=\eta}$$

The kinematic free surface boundary condition can be written:

$$\left.\frac{\partial \phi}{\partial z}\right|_{z=\eta} = \frac{\partial \eta}{\partial t} + \frac{\partial \eta}{\partial x}\frac{\partial \phi}{\partial x} + \frac{\partial \eta}{\partial y}\frac{\partial \phi}{\partial y} \tag{2-18}$$

Since linear wave theory assumes the wave elevation is small compared to the wave length, it is also assumed that the particle velocity components along x and y are small compared to the wave velocity. Therefore, the derivatives of these components are negligible, resulting in the linearized kinematic free surface boundary condition:.

$$\left.\frac{\partial \phi}{\partial z}\right|_{z=\eta} = \frac{\partial \eta}{\partial t} \tag{2-19}$$

2.2.4 Dynamic Boundary Condition

The dynamic free surface boundary relies on the assumption that the pressure outside the fluid is constant, that is:

$$\left.\frac{dp}{dt}\right|_{z=\eta} = 0 \tag{2-20}$$

From (2-14), the linearized Bernoulli equation at the free surface results in:

$$\eta = -\frac{1}{g}\left.\frac{\partial \phi}{\partial t}\right|_{z=\eta} \tag{2-21}$$

Since linear wave theory assumes the wave amplitude is small compared to the wave length, the free surface boundary conditions (both kinematic and dynamic) can be applied at the still water level ($z = 0$).

$$\left.\frac{\partial \phi}{\partial z}\right|_{z=0} = \frac{\partial \eta}{\partial t} \tag{2-22}$$

$$\eta = -\frac{1}{g}\left.\frac{\partial \phi}{\partial t}\right|_{z=0} \tag{2-23}$$

Taking the derivative of (2-23) with respect to time gives:

$$\frac{\partial \eta}{\partial t} = -\frac{1}{g}\left.\frac{\partial^2 \phi}{\partial t^2}\right|_{z=0} \tag{2-24}$$

Equating (2-22) and (2-24), the dynamic free surface boundary condition becomes:

$$\left.\frac{\partial^2 \phi}{\partial t^2}\right|_{z=0} + g\left.\frac{\partial \phi}{\partial z}\right|_{z=0} = 0 \tag{2-25}$$

2.2.5 Solution of Velocity Potential in Regular Waves

The velocity potential of an incident regular wave must satisfy the Laplace equation (2-10) and the boundary conditions at the seabed, (2-16), and the free surface, (2-19). The solution, which we call the incident wave potential, has been derived in many reference works, [31] and [32], and can be defined as:

$$\phi_I = \frac{gH}{2\omega}\frac{\cosh[k(z+h)]}{\cosh(kh)}\sin(kx-\omega t) \tag{2-26}$$

Plugging (2-26) back into the Laplace equation and the linearized Bernoulli equation, the dynamic wave pressure and fluid particle velocities from the wave can be obtained.

2.2.6 Power in Regular Waves

The energy flux, defined as the mean power per unit crest length, from an incident wave is found from the time averaged product of the wave pressure and the fluid particle velocity in the direction of the wave propagation.

$$J = \frac{1}{T}\int_0^T \int_{-h}^{\eta} p\frac{\partial \phi}{\partial x}\, dzdt = \frac{1}{2}\rho g A^2 c_g \tag{2-27}$$

where ρ is the fluid density, g is the acceleration due to gravity, H is the wave height, and c_g is the group velocity, defined by:

$$c_g = \frac{1}{2}\frac{\omega}{k}\left(1+\frac{2kh}{\sinh(2kh)}\right) = \frac{g}{2\omega}D(kh) \tag{2-28}$$

Plugging (2-28) into (2-27), the energy flux can be calculated as:

$$J = \frac{\rho g^2 A^2 D(kh)}{4\omega} \tag{2-29}$$

The function $D(kh)$ is the depth function, defined by:

$$D(kh) = \left[1+\frac{2kh}{\sinh(2kh)}\right]\tanh kh \tag{2-30}$$

and is represented in Figure 2.4. $D(kh)$ can be approximated in deep water ($kh \to \infty$) as 1, and in shallow water ($kh \to 0$) as $2kh$.

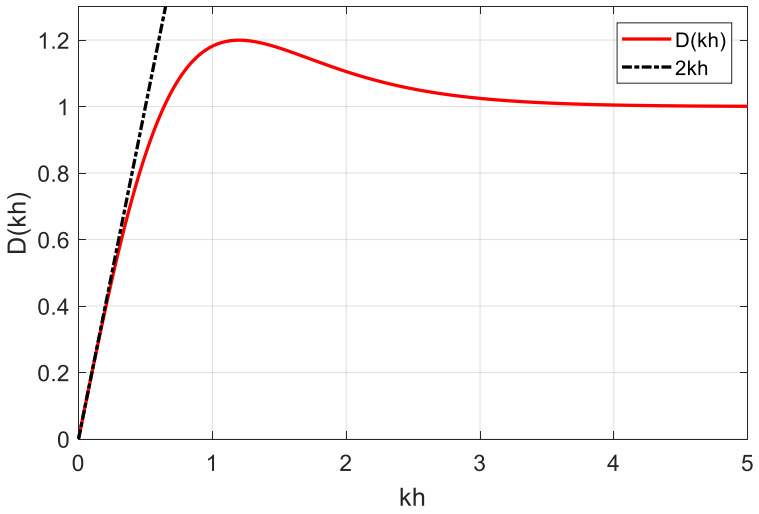

Figure 2.4 Graphical representation of the depth function

2.3 Wave-Body Interaction

When considering wave-body interactions, the velocity potential must not only satisfy the Laplace equation (2-10), the boundary condition and the seabed (2-16) and the boundary condition at the free surface (2-19), but the boundary condition on the submerged portion of the body as well, S_b. The velocity potential can be separated into three problems: the incident problem (Section 2.2.5), the diffraction problem and the radiation problem.

$$\phi = \phi_I + \phi_D + \phi_R \tag{2-31}$$

The incident potential, ϕ_I, defines the flow of an incident wave when no buoy is present. The diffraction potential, ϕ_D, defines the flow of the diffracted waves from the presence of a fixed body in the incident wave. The radiation potential, ϕ_R, defines the flow of radiated waves due to an oscillating body in still water.

As we defined earlier in (2-15), at a fixed boundary, the normal velocity of a fluid particle must be equal to zero. Since the diffraction potential defines the flow of diffracted waves while the body is kept fixed, the sum of the incident and diffraction potentials must fulfill the bodies boundary condition:

$$\left.\frac{\partial \phi_D}{\partial n}\right|_{S_b} = -\left.\frac{\partial \phi_I}{\partial n}\right|_{S_b} \tag{2-32}$$

To solve for the radiation potential, an additional boundary condition is needed when the body is in motion. As no flow is permitted to penetrate the bodies surface, the fluid

velocity perpendicular to the surface must be equal to the normal velocity component of the body, u_n.

$$\left.\frac{\partial \phi_R}{\partial n}\right|_{S_b} = u_n \tag{2-33}$$

If the body is not constrained, this boundary condition must be solved in all six degrees of freedom. Using the coordinate system defined in Section 2.1.1, we define **u** as the generalized velocity vector for a floating body:

$$\vec{u} = \vec{U} + \vec{\Omega} \times \vec{r} \tag{2-34}$$

$$\vec{r} = [x, y, z] \tag{2-35}$$

$$\vec{U} = \left[U_x, U_y, U_z\right] = [u_1, u_2, u_3] \tag{2-36}$$

$$\vec{\Omega} = \left[\Omega_x, \Omega_y, \Omega_z\right] = [u_4, u_5, u_6] \tag{2-37}$$

where $\vec{r}$ is the position vector, $\vec{U}$ defines the translation velocities in the x, y and z directions, and $\vec{\Omega}$ defines the rotational velocities about x, y and z. The subscripts 1 – 6 define the mode for each motion, which are summarized in Table 2.1.

Table 2.1 Modes of motion

Mode #	Mode	Velocity
1	Surge	$u_1 = U_x$
2	Sway	$u_2 = U_y$
3	Heave	$u_3 = U_z$
4	Roll	$u_4 = \Omega_x$
5	Pitch	$u_5 = \Omega_y$
6	Yaw	$u_6 = \Omega_z$

Applying the six degrees of freedom to (2-28), the boundary condition becomes:

$$\left.\frac{\partial \phi_R}{\partial n}\right|_{S_b} = \sum_{i=1}^{6} u_i n_i = \vec{u}^T \mathbf{n} \tag{2-38}$$

where u_i and n_i are the velocity and normal vector of the i-th mode, respectively, and **n** is the generalized normal vector:

$$\mathbf{n} = [\vec{n}, \vec{r} \times \vec{n}] \tag{2-39}$$

$$\vec{n} = \left[n_x, n_y, n_z\right] = [n_1, n_2, n_3] \tag{2-40}$$

$$\vec{r} \times \vec{n} = [n_4, n_5, n_6] \tag{2-41}$$

When the velocity potentials are solved for each problem, the total velocity potential for a regular harmonic time varying wave can be expressed as:

$$\phi(t,\vec{r}) = Re\left[\hat{\phi}(\vec{r}) \cdot e^{j\omega t}\right] \tag{2-42}$$

where ω is the angular frequency of the wave, t is the time, and $\hat{\phi}$ represents the complex amplitude of the velocity potential. Plugging (2-42) into the linearized Bernoulli equation (2-14), and assuming the buoy is initially at its equilibrium position (p_{atm} cancels out), we solve for the pressure of the fluid around the body:

$$p = -\rho Re\left[j\omega\hat{\phi}(\mathbf{r}) \cdot e^{j\omega t}\right] - \rho g z \tag{2-43}$$

The hydrodynamic and hydrostatic forces and moments are obtained by integrating (2-43) over the wetted surface area of the body, S_b.

$$\vec{F} = \iint_{S_b} p\vec{n}dS \tag{2-44}$$

$$\vec{M} = \iint_{S_b} p(\vec{r}\times\vec{n})dS \tag{2-45}$$

where $\vec{F}$ is the force vector in all six modes, and $\vec{M}$ is the moment vector in all six modes. By considering a generalized force vector, **F**, the generalized force can be written as:

$$\mathbf{F} = \iint_{S_b} p\mathbf{n}dS \tag{2-46}$$

$$\mathbf{F} = \left[\vec{F}, \vec{M}\right] \tag{2-47}$$

The hydrodynamic forces and moments can be broken up into two parts: the excitation force and the radiation force.

2.3.1 Hydrodynamic Forces

The excitation force is the force from an incident wave acting on a fixed body. It is calculated from (2-46) where only the incident and diffraction potentials from (2-42) are considered.

$$\mathbf{F}_e = -\rho \iint_{S_b} Re\left[j\omega\left(\hat{\phi}_I + \hat{\phi}_D\right) \cdot e^{j\omega t}\right]\mathbf{n}dS \tag{2-48}$$

The radiation force is the force that generates waves from the oscillation of a body in still water. It is calculated from (2-46), where only the radiation potential from (2-42) is considered.

$$\mathbf{F}_r = -\rho \iint_{S_b} Re\left[j\omega\left(\hat{\phi}_R\right) \cdot e^{j\omega t}\right]\mathbf{n}dS \tag{2-49}$$

Since the complex radiation potential is the sum of the wave potentials in all six modes, the radiation potential can be expressed as:

$$\hat{\phi}_R = \sum_{i=1}^{6} \hat{u}_i \hat{\phi}_i \tag{2-50}$$

The complex velocity can be expressed in terms of displacement as:

$$\hat{u}_i = j\omega \hat{q}_i \tag{2-51}$$

Plugging (2-51) into (2-50), the radiation force can be expressed as:

$$\mathbf{F}_r = \rho\omega^2 \iint_{S_b} Re\left[\sum_{i=1}^{6} \hat{q}_i \hat{\phi}_i \cdot e^{j\omega t}\right]\mathbf{n}dS \tag{2-52}$$

The radiation force for each mode, j, can be further simplified to:

$$F_{r,j} = \sum_{i=1}^{6} -A_{ji}(\omega)\frac{\partial^2 q_i}{\partial t^t} - b_{ji}(\omega)\frac{\partial q_i}{\partial t} \tag{2-53}$$

Here, A_{ji} and b_{ji} are the frequency dependent 'added mass' and 'radiation damping' coefficients, where the index ji denotes the coefficient in the j-th mode which is induced by oscillation in the i-th mode.

2.3.2 Hydrostatic Force

The hydrostatic force, also called gravitational restoring force or buoyancy, comes from the integration of the hydrostatic pressure, $p = -\rho g z$, in (2-42). Integration of the hydrostatic pressure yields a 6×6 matrix, $\mathbf{K}_h$, called the hydrostatic stiffness matrix. The hydrostatic force is proportional to the displacement of the body, $\vec{q}$, from its equilibrium:

$$\mathbf{F}_h = -\rho g \iint_{S_b} z\mathbf{n}dS = -\mathbf{K}_h\vec{q} \tag{2-54}$$

2.3.3 Total Wave Force

The total wave force on a floating body is the sum of the excitation force (2-48), the radiation force (2-49), and the hydrostatic force (2-54).

$$\mathbf{F}_{wave} = \mathbf{F}_e + \mathbf{F}_r + \mathbf{F}_h \tag{2-55}$$

Expanding the hydrodynamic and hydrostatic forces out, the wave force in the j-th mode can be expressed as:

$$F_{wave,j} = \hat{F}_{e,j} e^{j\omega t} + \sum_{i=1}^{6} -A_{ji}(\omega)\frac{\partial^2 q_i}{\partial t^t} - b_{ji}(\omega)\frac{\partial q_i}{\partial t} - k_h q_i \qquad (2\text{-}56)$$

To calculate the frequency dependent wave force of varying floating structures, the software tool WAMIT [33] was used.

2.4 WAMIT

WAMIT (WaveAnalysisMIT) is a frequency-domain boundary element method (BEM) software tool that solves the linear radiation/diffraction problem, described in section 2.3, for various types of floating and submerged structures [33]. Structures are created in the computer aided design (CAD) software tool, MultiSurf [34], and can be analyzed by WAMIT through geometric data files. WAMIT solves the radiation/diffraction problem for the designated geometries, as well as for given frequencies, and outputs the first order hydrostatic and hydrodynamic properties.

2.4.1 MultiSurf

MultiSurf is a CAD software tool that is used to generate three-dimensional discretized body surfaces. Using a low-order method, the body surface is represented by a mesh of flat, quadrilateral panels. The low order method assumes the velocity potentials for each panel are piecewise constant values. MultiSurf is a convenient tool because it can be accessed by WAMIT to avoid user development of the panel files, which can be long and cumbersome.

2.4.2 WAMIT Input

The two principal subprograms of WAMIT are POTEN and FORCE. POTEN, which solves for the velocity potential on the surface of the body, has two primary user input files: the Potential Control file (POT) and the Geometric Data file (GDF). The POT file specifies parameters such as fluid depth, wave periods, wave headings, the number of bodies to be analyzed, and the GDF files of those bodies. The GDF file specifies the discretized surface of the analyzed geometry, which are defined and created in MultiSurf. FORCE, which solves for the force and motion coefficients, has one primary user input file, the Force

Control file (FRC). The FRC file specifies which hydrodynamic parameters are to be evaluated and output from the program, as well as the bodies center of gravity and radii of gyration.

An additional user input file is needed to run WAMIT called the Configuration file (CFG). The CFG file is where the user specifies various parameters and computational options. This ranges from how the program is run (direct vs. iterative solver), to how the output is displayed, and more.

2.4.3 WAMIT Output

WAMIT outputs normalized forms of the hydrodynamic parameters we specify to be returned. The output parameters we specified were the added mass (A_{ij}) and radiation damping coefficients (b_{ij}), and the excitation force (F_{ei}). The normalized parameters are defined by the following equations:

$$\bar{A}_{ij} = \frac{A_{ij}}{\rho L^k} \tag{2-57}$$

$$\bar{b}_{ij} = \frac{b_{ij}}{\rho \omega L^k} \tag{2-58}$$

$$\bar{F}_{ei} = \frac{F_{ei}}{\rho g A L^m} \tag{2-59}$$

where,

- A_{ij} is the added mass in the i-th mode, induced by motion in the j-th mode
- b_{ij} is the radiation damping in the i-th mode, induced by motion in the j-th mode
- F_{ei} is the excitation force in the i-th mode
- A is the wave amplitude
- L is the characteristic length, which is defined as $1m$
- $k = 3$ for $(i, j = 1,2,3)$
- $k = 4$ for $(i = 1,2,3,\ j = 4,5,6)$ or $(i = 4,5,6,\ j = 1,2,3)$
- $k = 5$ for $(i, j = 4,5,6)$
- $m = 2$ for $(i = 1,2,3)$
- $m = 3$ for $(i = 4,5,6)$

3. Dynamics and Design of a Self-Reacting Resonant Wave Energy Converter

3.1 Motivation

The simplest type of point absorber is the single body wave energy converter (WEC), which has been studied extensively [17,35,36]. The single body WEC typically consists of a floating buoy connected to the seabed with a linear power takeoff system (PTO). The forced harmonic excitation from the wave drives the buoy up and down (heave) and the single body WEC is designed to achieve resonance at this harmonic wave frequency. Characteristic wave periods usually vary between four seconds and fifteen seconds [24], which equate to very small wave frequencies (0.07 – 0.25 Hz). Early research showed that small buoy point absorbers would perform poorly in this range of frequencies. As Falcão points out [12], for a wave period of ten seconds, the radius of the floating buoy must be 26.2m to achieve resonance; too large to be practical. Another method of developing a resonant WEC is a self-reacting two-body point absorber. The two-body WEC uses the relative motion between a floating buoy and a submerged body to capture energy. Advantages of a two-body WEC include easier ocean implementation (mooring, generator installment, etc.) and dynamic performance (parameter optimization). Early research of two-body WECs, which mainly focused on regular wave excitation, showed that the optimal power for a floating buoy could be achieved through PTO parameter optimization [18]. Further research [37] showed that by adjusting the position of the two-body WEC, as well as the device dimensions, the amplitude response and power could be adjusted as well. In this chapter, through the use of frequency domain analysis, the dynamics of a single-body point absorber and two-body point absorber are analyzed and their performance are compared. Here, the size of the reacting body for the two-body system is studied and optimized to improve wave energy conversion performance.

3.2 Single Body Resonant Wave Energy Converter

The simplest type of point absorber is the single body WEC. The single body WEC, shown on the left in Figure 3.1, consists of a floating buoy connected to the seabed by a linear power takeoff device (PTO). Energy is extracted by the PTO through the oscillating heave motion of the floating buoy when subjected to an incident wave. In this case, the reacting force is provided by the seabed.

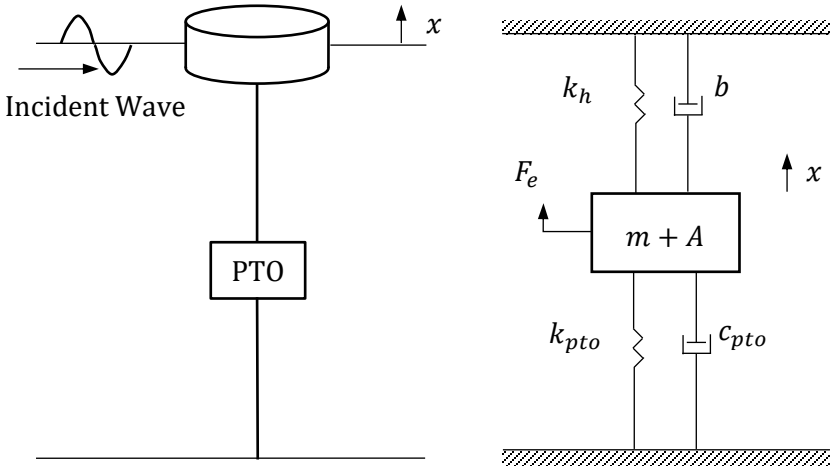

Figure 3.1 Schematic representation and equivalent dynamic model of a single-body point absorber

The equation of motion for such a device can be written as:

$$m\ddot{x} = F_{wave} - F_{pto} \tag{3-1}$$

As described in section 2.3.3, the wave force from the incident wave can be split into three parts; excitation force, radiation force and hydrostatic force:

$$m\ddot{x} = F_e + F_r + F_h - F_{pto} \tag{3-2}$$

Using the hydrodynamic properties described in section 2.3, the single body, single degree of freedom system can be characterized by the vibration system on the right of Figure 3.1, with the following equation of motion:

$$(m + A)\ddot{x} + \left(c_{pto} + b\right)\dot{x} + \left(k_{pto} + k_h\right)x = F_e \tag{3-3}$$

where,

- x is the vertical coordinate (heave) of the buoy
- m is the dry mass of the buoy
- A is the frequency dependent heave induced added mass
- b is the frequency dependent heave induced radiation damping coefficient
- F_e is the frequency dependent heave induced excitation force

- k_h is the hydrostatic stiffness
- c_{pto} is the PTO linear damping coefficient
- k_{pto} is the PTO linear spring stiffness

Under regular wave excitation, which is described in section 2.1.2, the excitation force can be represented by the harmonic forcing function $F_e = f_e e^{j\omega t}$, where f_e is the amplitude, j is the imaginary unit, and ω is the wave frequency. Using the method of undetermined coefficients, we assume that the particular solution takes the same form as the forcing function. That is, $x = Xe^{j\omega t}$, where X is the amplitude of the response. Substituting the solution into (3-1), we obtain:

$$-\omega^2 X(m + A) + j\omega X\left(c_{pto} + b\right) + X\left(k_{pto} + k_h\right) = f_e \tag{3-4}$$

Solving for X, we obtain:

$$X = \frac{f_e}{-\omega^2(m + A) + j\omega\left(c_{pto} + b\right) + \left(k_{pto} + k_h\right)} \tag{3-5}$$

The average absorbed power of the PTO is defined as the time averaged integral of the product of the PTO force and the velocity of the buoy:

$$P_{ave} = \frac{1}{T}\int_0^T F_{pto}\dot{x}dt = \frac{1}{T}\int_0^T c_{pto}(\dot{x})^2 dt \tag{3-6}$$

The average absorbed power of the PTO can be further defined as:

$$P_{ave} = \frac{1}{2}\omega^2 c_{pto}|X|^2 \tag{3-7}$$

To generate maximum power, the complex magnitude of the response, $|X|$, needs to be maximized, which occurs at resonance. Resonance occurs when the wave frequency, ω, is equal to the natural frequency, ω_n. The natural frequency of the system is defined as:

$$\omega_n = \sqrt{\frac{k_{pto} + k_h}{m + A}} \tag{3-8}$$

Substituting (3-5) and (3-8) into (3-7) yields:

$$P_{ave} = \frac{1}{2} c_{pto} \frac{{f_e}^2}{\left(c_{pto} + b\right)^2} \tag{3-9}$$

Taking the derivative of (3-9) with respect to c_{pto} yields an optimal value of $c_{pto} = b$. Substituting that back into (3-9) yields the maximum average absorbed power of the buoy:

$$P_{max} = \frac{1}{8b}|f_e|^2 \tag{3-10}$$

The capture width, which is the width of wave front that contains the same amount of power as absorbed by the WEC, is used to characterize the performance of WECs in waves. It is defined as, $\mu = P/J$, the ratio of the output power of the WEC and the energy flux from the wave, (2-29). The maximum capture width of a resonating point absorber, (3-10), is $\lambda/2\pi$ (in units of m), which is consistent with the results found in [17,35,36].

While (3-10) proves that a maximum average absorbed power exists, attaining a natural frequency that matches the incident wave frequency is impractical. Typical incident wave frequencies are very low, ranging between 0.07 Hz and 0.25 Hz [24]. From (3-8), that would require either an extremely small value of $k_{pto} + k_h$, or a very large value of $m + A$. In section 2.3.2, the hydrostatic stiffness, k_h, was defined as (2-47). Increasing the radius of the buoy would not only increase $m + A$, but would increase k_h as well. Falcão found that for a hemispherical buoy, the optimal radius to achieve resonance in regular waves for an incident wave frequency of 0.1 Hz was 26.2 m, which is economically impractical [12]. A more practical method of achieving resonance is to add an additional submerged mass. This method increases $m + A$ without increasing k_h. Difficulties of implementing these devices in more energetic waves still arise, where distance between the buoy and the seabed becomes challenging.

3.3 Two-Body Wave Energy Converter - Submerged Mass

Another method of developing a resonant WEC is a self-reacting two-body point absorber. The two-body point absorber uses the relative motion between the floating buoy and a submerged body to capture energy. Unlike the single body point absorber, where the reacting force comes from the seabed, the reacting force of the two-body point absorber comes from the submerged body, hence self-reacting.

3.3.1 Dynamics of the Two-Body Wave Energy Converter

The two-body WEC, shown on the left in Figure 3.2, consists of two axisymmetric masses, a floating buoy and a submerged body, subjected to an incident wave. The floating buoy and submerged body are connected through a linear PTO and energy is extracted from the relative motion of both masses.

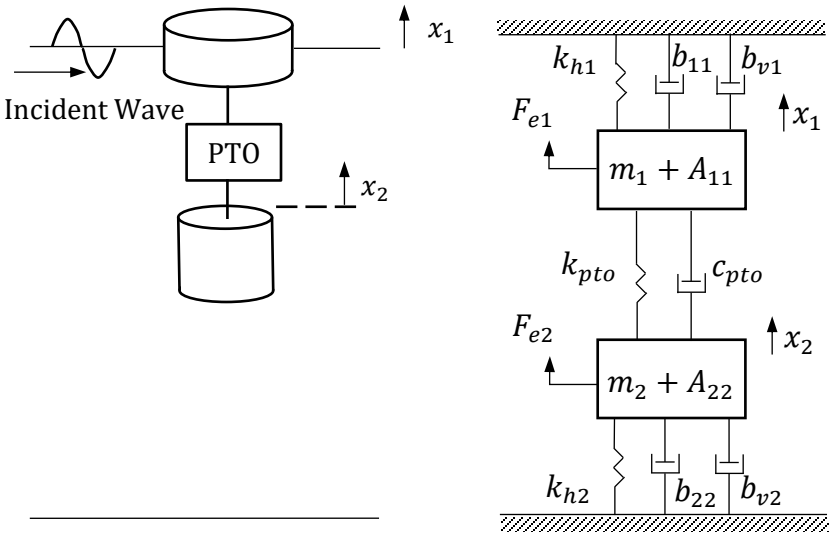

Figure 3.2 Schematic representation and equivalent dynamic model of a two-body point absorber

The equations of motion for such a device can be written as:

$$m_1\ddot{x}_1 = (F_{wave})_1 - F_{pto} - (F_{vis})_1 \tag{3-11}$$

$$m_2\ddot{x}_2 = (F_{wave})_2 + F_{pto} - (F_{vis})_2 \tag{3-12}$$

where the subscripts 1 and 2 represent the floating buoy and submerged body, respectively. As was done in the single body analysis, the wave force from the incident wave can be broken up into three parts; excitation force, radiation force and hydrostatic force. In addition to the wave force, a viscous drag force has been included in the model. While linear wave theory assumes the fluid to be inviscid, adding viscous effects to the equations of motion has been shown to increase the accuracy of the model [22]. To keep the force linear in the frequency domain, the quadratic viscous drag force can be linearized [18]. Applying the hydrodynamic coefficients of the wave force to (3-11) and (3-12), the two-body, two degree of freedom system can be characterized as the vibration system on the right of Figure 3.2 and by the following equations of motion:

$$\begin{aligned}(m_1 + A_{11})\ddot{x}_1 + A_{12}\ddot{x}_2 + \left(c_{pto} + b_{11} + b_{v1}\right)\dot{x}_1 + \left(b_{12} - c_{pto}\right)\dot{x}_2 \\ + \left(k_{pto} + k_{h1}\right)x_1 - k_{pto}x_2 = F_{e1}\end{aligned} \tag{3-13}$$

$$(m_2 + A_{22})\ddot{x}_2 + A_{21}\ddot{x}_1 + (c_{pto} + b_{22} + b_{v2})\dot{x}_2 + (b_{21} - c_{pto})\dot{x}_1 + (k_{pto} + k_{h2})x_2 - k_{pto}x_1 = F_{e2} \tag{3-14}$$

where,

- x_1 and x_2 are the respective vertical coordinates of the buoy and submerged body
- m_1 and m are the respective dry masses of the buoy and submerged body
- A_{11} and A_{22} are the respective added masses of the buoy and submerged body
- A_{12} and A_{21} are the coupled added masses
- b_{11} and b_{22} are the respective radiation damping coefficients
- b_{12} and b_{21} are the coupled radiation damping coefficients
- F_{e1} and F_{e2} are the respective excitation forces
- k_{h1} and k_{h2} are the respective hydrostatic stiffness's
- b_{v1} and b_{v2} are the respective linearized viscous damping coefficients
- c_{pto} and k_{pto} are the linear PTO damping coefficient and spring stiffness

Under regular wave excitation, the excitation force on each body can be represented by the harmonic forcing functions $F_{e1}(t) = F_1 e^{j\omega t}$ and $F_{e2}(t) = F_2 e^{j\omega t}$, where f_{e1} and f_{e2} are the amplitudes on the buoy and submerged body, respectively. As was done for the single body case, we assume the solutions of the equations of motion are $x_1(t) = X_1 e^{j\omega t}$ and $x_2(t) = X_2 e^{j\omega t}$, where X_1 and X_2 are the response amplitudes on the buoy and submerged body, respectively. Substituting the solutions into (3-13) and (3-14), we obtain:

$$-\omega^2(m_1 + A_{11})X_1 - \omega^2 A_{12}X_2 + j\omega(c_{pto} + b_{11} + b_{v1})X_1 + j\omega(b_{12} - c_{pto})X_2 + (k_{pto} + k_{h1})X_1 - k_{pto}X_2 = F_{e1} \tag{3-15}$$

$$-\omega^2(m_2 + A_{22})X_2 - \omega^2 A_{21}X_1 + j\omega(c_{pto} + b_{22} + b_{v2})X_2 + j\omega(b_{21} - c_{pto})X_1 + (k_{pto} + k_{h2})X_2 - k_{pto}X_1 = F_{e2} \tag{3-16}$$

Equations (3-15) and (3-16) can be written into matrix form as:

$$(-\omega^2\mathbf{M} + j\omega\mathbf{C} + \mathbf{K})\mathbf{X} = \mathbf{F} \tag{3-17}$$

with the following matrices:

$$\mathbf{M} = \begin{bmatrix} m_1 + A_{11} & A_{12} \\ A_{21} & m_2 + A_{22} \end{bmatrix},\ \mathbf{C} = \begin{bmatrix} c_{pto} + b_{11} + b_{v1} & b_{12} - c_{pto} \\ b_{21} - c_{pto} & c_{pto} + b_{22} + b_{v2} \end{bmatrix}$$

$$\mathbf{K} = \begin{bmatrix} k_{pto} + k_{h1} & -k_{pto} \\ -k_{pto} & k_{pto} + k_{h2} \end{bmatrix},\ \mathbf{X} = \begin{bmatrix} X_1 \\ X_2 \end{bmatrix},\ \mathbf{F} = \begin{bmatrix} F_1 \\ F_2 \end{bmatrix}$$

We can define the terms in parentheses in (3-17) as the impedance matrix **Z**:

$$\mathbf{Z}(j\omega) = -\omega^2\mathbf{M} + j\omega\mathbf{C} + \boldsymbol{K} = \begin{bmatrix} Z_{11} & Z_{12} \\ Z_{21} & Z_{22} \end{bmatrix} \tag{3-18}$$

the elements of which are:

$$Z_{11} = -\omega^2(m_1 + A_{11}) + j\omega\left(c_{pto} + b_{11} + b_{v1}\right) + k_{pto} + k_{h1} \tag{3-18a}$$

$$Z_{12} = -\omega^2 A_{12} + j\omega\left(b_{12} - c_{pto}\right) - k_{pto} \tag{3-18b}$$

$$Z_{21} = -\omega^2 A_{21} + j\omega\left(b_{21} - c_{pto}\right) - k_{pto} \tag{3-18c}$$

$$Z_{22} = -\omega^2(m_2 + A_{22}) + j\omega\left(c_{pto} + b_{22} + b_{v2}\right) + k_{pto} + k_{h2} \tag{3-18d}$$

Solving for **X**, the solution of (3-17) is:

$$\mathbf{X} = \mathbf{Z}^{-1}\mathbf{F} \tag{3-19}$$

X_1 and X_2 are the respective responses of the buoy and submerged body:

$$X_1 = \frac{Z_{22}F_1 - Z_{12}F_2}{Z_{11}Z_{22} - Z_{12}Z_{21}} \tag{3-19a}$$

$$X_2 = \frac{Z_{11}F_2 - Z_{21}F_1}{Z_{11}Z_{22} - Z_{12}Z_{21}} \tag{3-19b}$$

The average absorbed power of the PTO is defined as the time averaged integral of the product of the PTO force and the relative velocity between the buoy and submerged body:

$$P_{ave} = \frac{1}{T}\int_0^T F_{pto}(\dot{x}_1 - \dot{x}_2)dt = \frac{1}{2}\omega^2 c_{PTO}|X_1 - X_2|^2 \tag{3-20}$$

Applying (3-19) to (3-20) the average absorbed power takes the closed-form solution:

$$P_{ave} = \frac{1}{2}\omega^2 c_{PTO}\left|\frac{p + jq}{(a + jb)c_{PTO} + (c + jd)k_{PTO} + e + jf}\right|^2 \tag{3-21}$$

where,

$$p = (-\omega^2(m_2 + A_{22} + A_{21}) + k_{h2})F_1 + (\omega^2(m_1 + A_{11} + A_{12}) - k_{h1})F_2 \tag{3-21a}$$

$$q = \omega(b_{22} + b_{21} + b_{v2})F_1 - \omega(b_{11} + b_{12} + b_{v1})F_2 \tag{3-21b}$$

$$a = -\omega^2(b_{11} + b_{22} + b_{12} + b_{21} + b_{v1} + b_{v2}) \tag{3-21c}$$

$$b = -\omega^3(m_1 + A_{11} + A_{12} + m_2 + A_{22} + A_{21}) + \omega(k_{h1} + k_{h2}) \tag{3-21d}$$

$$c = b/\omega = -\omega^2(m_1 + A_{11} + A_{12} + m_2 + A_{22} + A_{21}) + (k_{h1} + k_{h2}) \tag{3-21e}$$

$$d = -a/\omega = \omega(b_{11} + b_{12} + b_{v1} + b_{22} + b_{21} + b_{v2}) \tag{3-21f}$$

$$e = \omega^4[(m_1 + A_{11})(m_2 + A_{22}) - A_{12}A_{21}] - \omega^2[(m_1 + A_{11})k_{h2} + (m_2 + A_{22})k_{h1} + (b_{11} + b_{v1})(b_{22} + b_{v2}) - b_{12}b_{21}] + k_{h1}k_{h2} \tag{3-21g}$$

$$f = -\omega^3[(m_1 + A_{11})(b_{22} + b_{v2}) + (m_2 + A_{22})(b_{11} + b_{v1}) - A_{12}b_{21} - A_{21}b_{12}] + \omega[k_{s2}(b_{11} + b_{v1}) + k_{h1}(b_{22} + b_{v2})] \tag{3-21h}$$

Taking the derivative of (3-21) with respect to both k_{PTO} and c_{PTO}, the optimal values of each PTO component can be found to maximize the average absorbed power. First, taking the derivative of (3-21) with respect to k_{PTO} yields:

$$k_{pto|opt} = -\frac{ce + df}{c^2 + d^2} \tag{3-22}$$

As there are two degrees of freedom (two bodies constrained in heave), there are two natural frequencies. This equation represents the PTO stiffness that will match one of the natural frequencies to the wave frequency (resonance), based on the parameters of the system. Taking the derivative of (3-21) with respect to c_{PTO} yields:

$$c_{pto} = \sqrt{\frac{e^2 + f^2 + (c^2 + d^2){k_{pto}}^2 + (2ce + 2df)k_{pto}}{\omega^2(c^2 + d^2)}} \tag{3-23}$$

Applying (3-22) to (3-23), the optimal PTO damping coefficient can be further defined:

$$c_{pto|opt} = \frac{1}{\omega}\frac{|cf - de|}{c^2 + d^2} \tag{3-24}$$

Applying both (3-22) and (3-24) to (3-21), the optimal average absorbed power is:

$$P_{ave|opt} = \frac{1}{4}\omega^2 \frac{p^2 + q^2}{|ae + bf| + (ae + bf)} \tag{3-25}$$

3.3.2 Frequency Domain Simulation

To study the influence of the submerged body in the frequency domain, we numerically solve (3-22), (3-24), (3-25) for the optimal case and (3-21) and (3-23) when $k_{pto} \neq k_{pto|opt}$. In particular, we examine the optimal case and the case when $k_{pto} = 0$. In this simulation, we are assuming the submerged body is a shapeless mass that is deep enough where the hydrodynamic radiation damping and excitation force are negligible. As the submerged body is assumed a shapeless mass, the mass in our simulation is considered the total mass, which is the sum of the dry mass and added mass. We also assume that the submerged body is far enough from the top buoy that the cross-coupled hydrodynamic added mass and radiation damping are negligible. The top buoy configuration, Figure 3.3, was created in MultiSurf, and the hydrodynamic parameters, Figure 3.4, were analyzed using WAMIT. The hydrodynamic parameters can be dimensionalized using (2-49), (2-51) and (2-50).

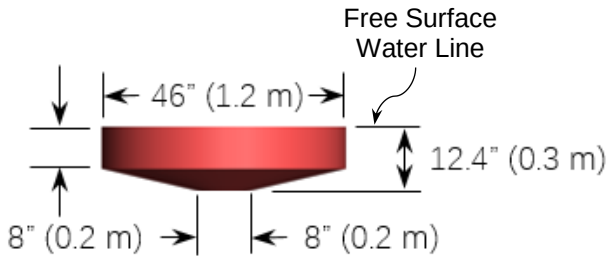

Figure 3.3 Top buoy configuration created in MultiSurf

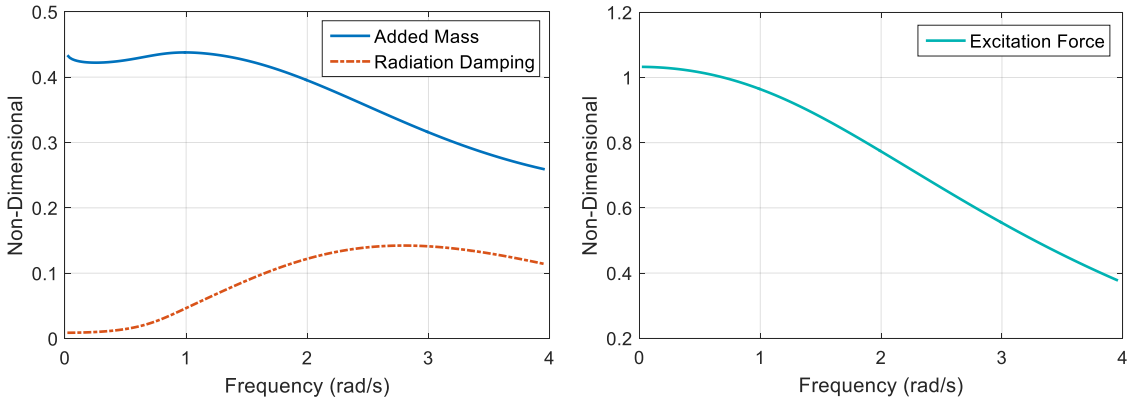

Figure 3.4 Hydrodynamic parameters of the top buoy analyzed using WAMIT

Figures 3.5 through 3.9 show the results of the frequency domain simulation using a wave period of 6s (wave frequency of 1.04 rad/s) and a wave height of 1.5m. Figure 3.5 shows a comparison of the optimal power and the power when $k_{pto} = 0$ of a two-body WEC and a single-body WEC when no viscous damping is considered, $b_{v1} = b_{v2} = 0$. The power is compared with respect to the mass-ratio, which we define as the ratio of the total mass of the submerged body to the dry mass of the top buoy. The optimal power of the two-body WEC reaches the maximum power of the single-body WEC for all mass ratios. In this case, the PTO damping and stiffness are optimized to achieve resonance at each mass ratio. The power for the two-body system when $k_{pto} = 0$ reaches the same maximum power, however only at a certain mass-ratio, which we call the optimal mass-ratio. The power then decreases to the maximum power of a single-body WEC when $k_{pto} = 0$ (it is not clear in the figure, however, as the mass ratio approaches infinity the power reduces to the maximum power for the single-body case when $k_{pto} = 0$).

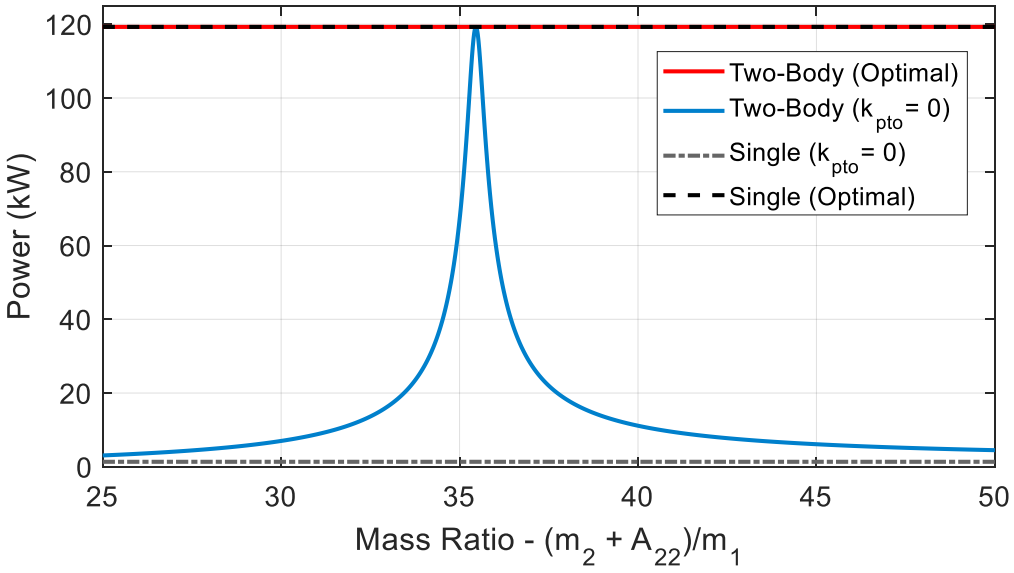

Figure 3.5 Analytically derived powers for a two-body WEC. The optimal power is the same as the optimal power of a single body WEC. Without the inclusion of a PTO stiffness term, the two-body WEC is still able to achieve this optimal power.

In Figure 3.6, we see the optimized PTO stiffness and damping for the optimal case and the optimized PTO damping for the case when $k_{pto} = 0$. The optimal PTO stiffness will become negative when the mass ratio exceeds what we call the critical mass ratio. For the case of no viscous damping, the critical mass ratio is equal to the optimal mass ratio.

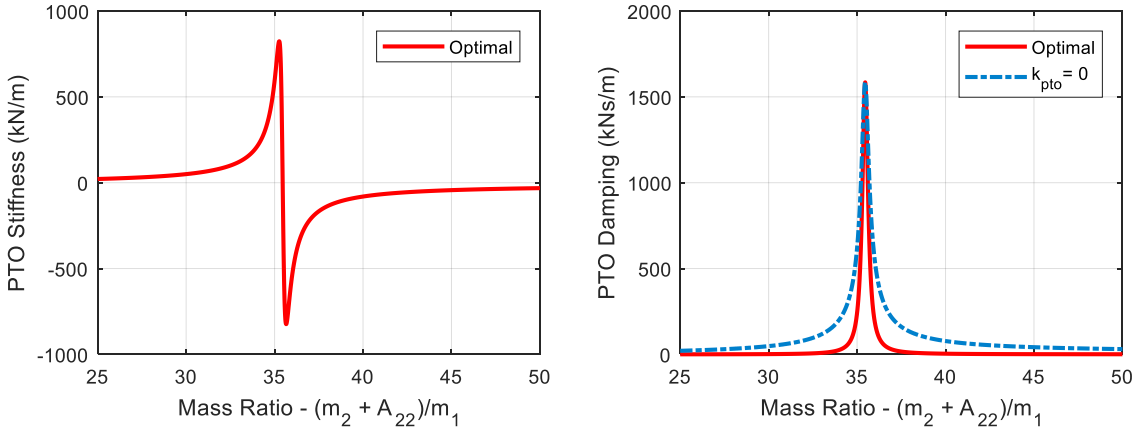

Figure 3.6 Analytical solutions for the optimal PTO stiffness (left) and damping (right).

Figure 3.7 shows the damped natural frequencies of the optimal case and the case when $k_{pto} = 0$. To calculate the damped natural frequencies, we take the determinant of (3-18) and set it equal to zero. Solving for ω results in a set of complex conjugate pole pairs, of

which the magnitudes correspond to the two natural frequencies, and the imaginary terms correspond to the two damped natural frequencies. The damped natural frequency for the optimal case always matches the wave excitation frequency, whereas for the case when $k_{pto} = 0$, the damped natural frequency matches the wave excitation frequency at the optimal mass ratio.

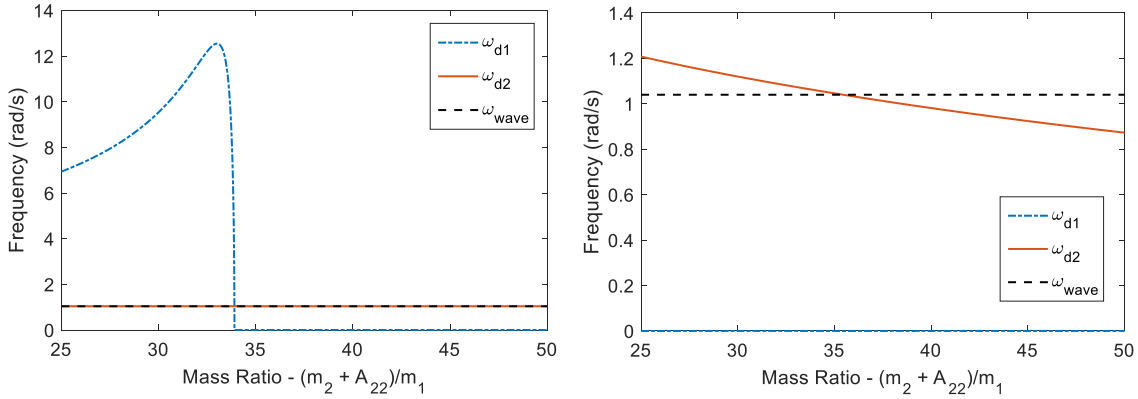

Figure 3.7 Damped natural frequencies of the optimal case (left) and the case with no PTO stiffness (right).

Figure 3.8 shows the displacements and relative displacements of the top buoy and submerged body for both the optimal case and the case when $k_{pto} = 0$. Both cases have very large displacements when comparing to the height of the wave (1.5m). The submerged body displacement for the optimal case increases exponentially as the mass ratio approaches zero. The top buoy displacement for the optimal case reaches a maximum at it's critical mass ratio. For the case when $k_{pto} = 0$, the relative displacement is relatively small, however, both the top buoy and submerged body have large displacements at the optimal mass ratio, when resonance occurs.

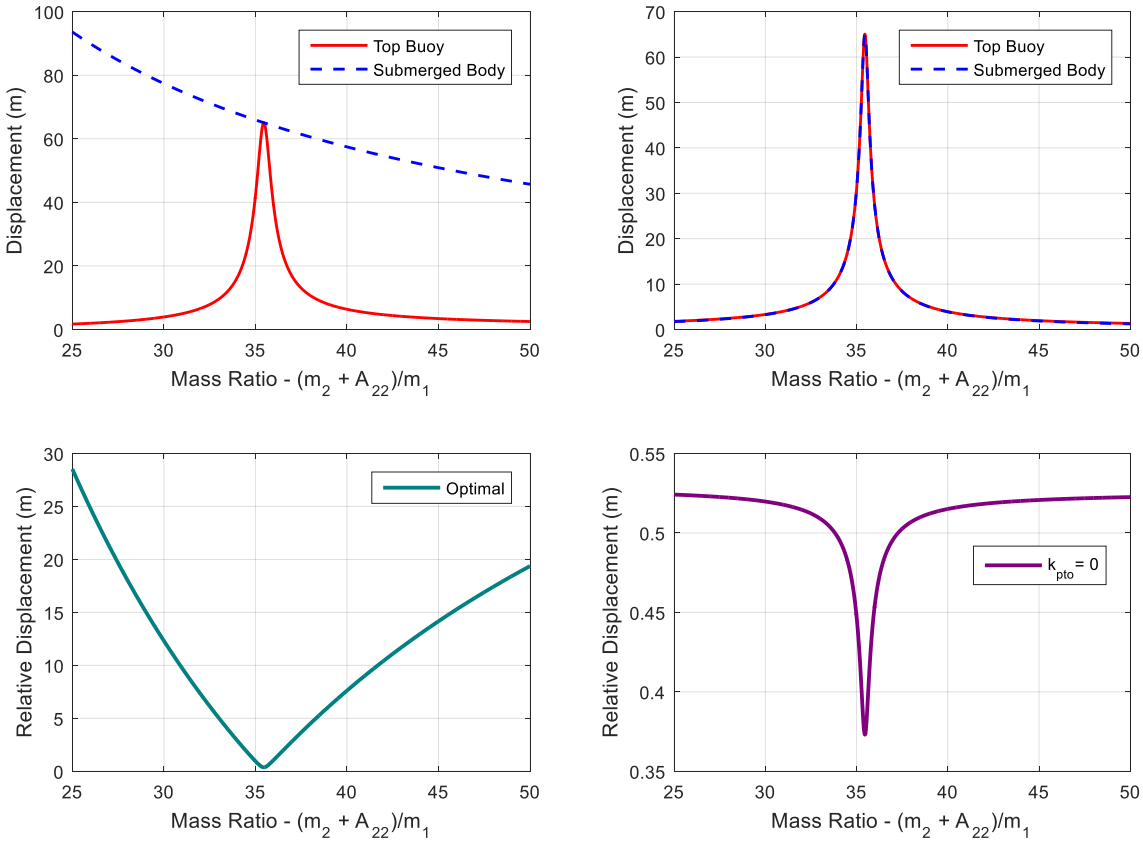

Figure 3.8 Displacements and relative displacements of the WEC for the optimal case and when the PTO stiffness is zero. At resonance, the displacement of the WEC is very large, yet the relative displacement is very small.

As the displacements are unrealistic, we now consider viscous drag damping into our model. From [38], experimental wave tank testing shows that damping on the top buoy is dominated by the radiation damping and drag has minimal effects, thus viscous drag damping is only considered on the submerged body. We also introduce the condition that if the mass ratio exceeds the critical mass ratio, the optimal PTO stiffness will be set to zero. While a negative spring stiffness is achievable [39], the springs are unstable and hard to model. Figure 3.9 shows the comparison of the optimal power and the power when $k_{pto} = 0$ for a two-body WEC when $b_{v2} \neq 0$. As expected, as b_{v2} increases, the power decreases. The power for the optimal case, the dashed red line, is never able to achieve the maximum power of the single-body WEC in Figure 3.5 (120kW). The maximum achievable power, when viscous drag damping is included, occurs at the optimal mass ratio, when $k_{pto} = 0$.

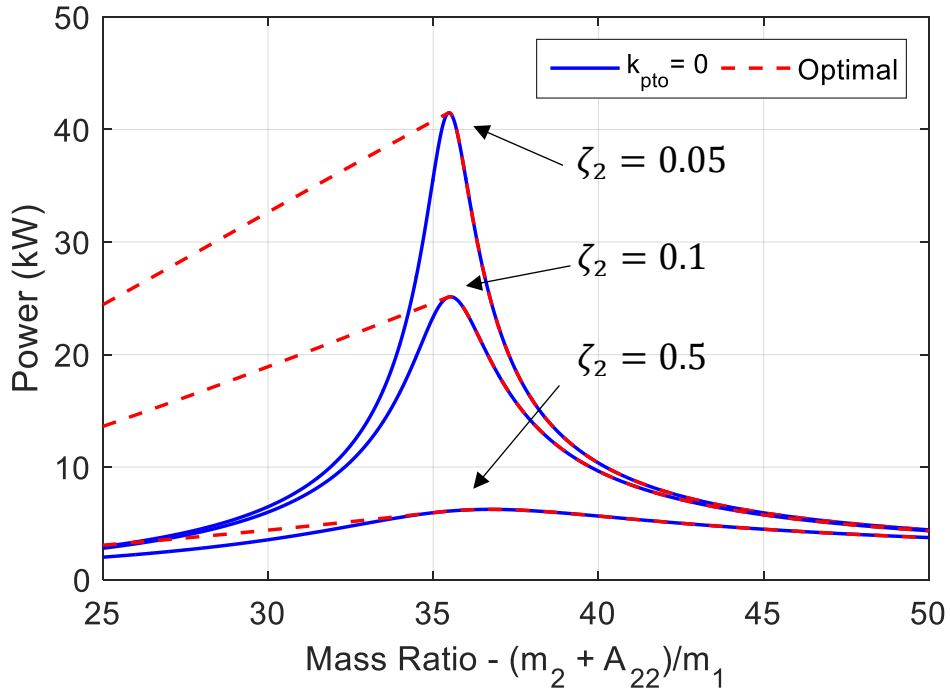

Figure 3.9 Comparison of optimal power and power with no PTO stiffness when linear viscous effects are included.

Real sea waves are typically very irregular and can be seen as a superposition of multiple regular harmonic waves, each with their own set of wave height, wave period, and wavelength. As discussed in section 2.1.3, the Pierson-Moskowitz spectrum, (2-4) is used to define the energy distribution with respect to wave frequency for a fully developed wave. The average absorption power of a WEC in irregular waves can be found through the spectrum integration:

$$\bar{P}_{irr} = \int_0^\infty P_{ave}\left(k_{pto}, c_{pto}, \omega\right) S(\omega) d\omega \tag{3-26}$$

where $P_{ave}\left(k_{pto}, c_{pto}, \omega\right)$ is the absorption power in regular waves defined by (3-21), using the regular wave PTO stiffness and damping values found for each mass-ratio at the peak period (in this case 6s). $S(\omega)$ is the Pierson-Moskowitz spectrum defined by (2-4).

Figure 3.10 shows the comparison of power when k_{pto} is optimized, and when $k_{pto} = 0$. Due to setting $k_{pto|opt} = 0$ when $k_{pto|opt} < 0$, the optimal power never exceeds the power when $k_{pto} = 0$. Having no PTO stiffness will simplify the design of the PTO.

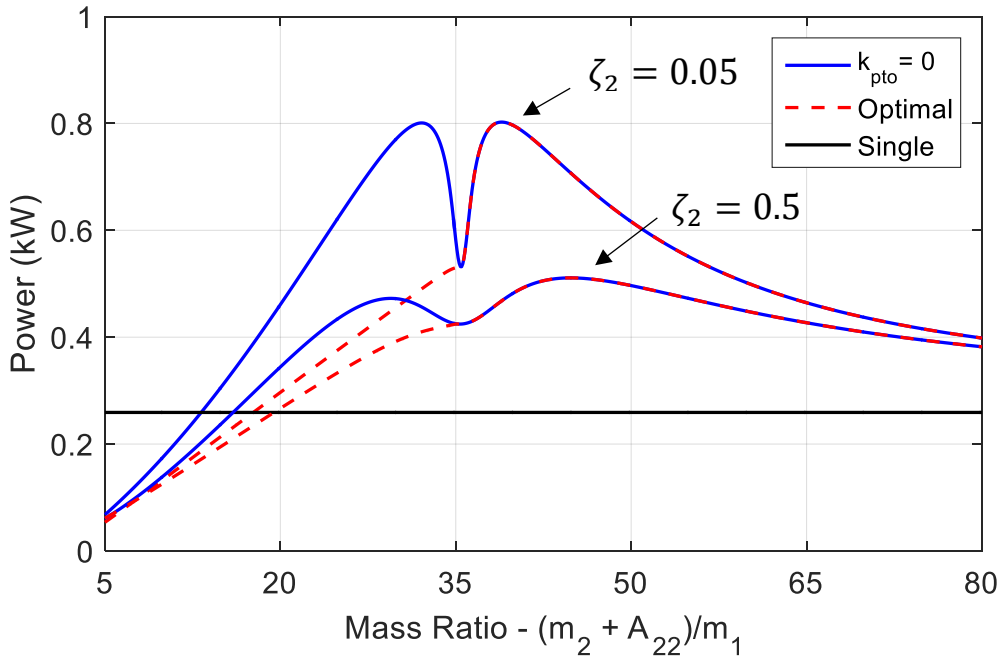

Figure 3.10 Analytically derived optimal powers for irregular sea states using a Pierson-Moskowtiz spectrum.

3.4 Two-Body Wave Energy Converter - Internal Mass

To avoid the negative effects of viscous damping altogether, a two-body wave energy converter with an internal mass is studied. Such configurations have been studied previously [40,41,42]. Both Parks and Korde found that while systems designed with an internal mass can achieve similar powers as the external mass, the internal mass has a smaller power bandwidth of wave periods. Figure 3.11 shows a schematic of the proposed device and the equivalent vibration system. There are no hydrodynamic forces acting on the inner mass, which is now connected to the buoy by the PTO only. In the submerged body case, the submerged body was neutrally buoyant, having the same weight as the displaced water weight, as well as a small hydrostatic force to keep it in equilibrium. Here, to keep the whole system afloat, the weight of the whole system, m_{sys}, must be equal to the displaced water weight of the buoy, i.e. (3-27):

$$m_{sys} = m_1 + m_2 + m_{pto} \leq \rho V_{disp} \tag{3-27}$$

where m_1 is the mass of the buoy, m_2 is the inner mass, m_{pto} is the mass of the PTO assembly, ρ is the density of water and V_{disp} is the displaced volume of water from the buoy.

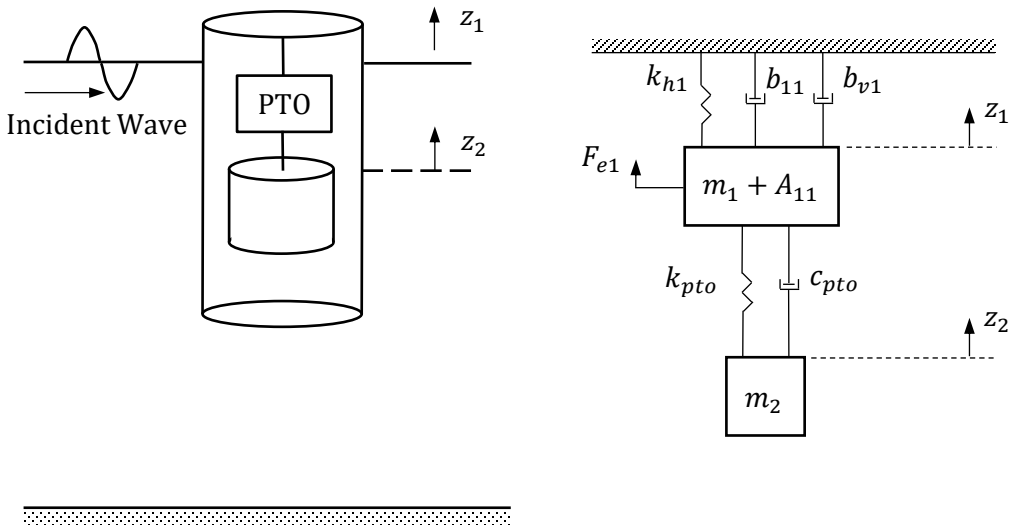

Figure 3.11 Schematic and equivalent dynamic model of the two-body WEC with an internal mass.

Much in the same way the equations of motion were formulated for the submerged two-body WEC, the equations of motion of this device take the same form without wave forces on the internal mass. Removing the wave forces on the internal mass from (3-13) and (3-14), the equations of motion for this device can be written as:

$$(m_1 + A_{11})\ddot{x}_1 + (c_{PTO} + b_{11} + b_{v1})\dot{x}_1 + (k_{PTO} + k_{h1})x_1 - c_{PTO}\dot{x}_2 - k_{PTO}x_2 = F_{e1} \tag{3-28}$$

$$m_2\ddot{x}_2 + c_{PTO}\dot{x}_2 + k_{PTO}x_2 - c_{PTO}\dot{x}_1 - k_{PTO}x_1 = 0 \tag{3-29}$$

Using the same process as the submerged body case, the closed-form solution for the average absorbed power for this device takes the same form as (3-21), where (3-21a) through (3-21h) can be simplified as:

$$p = -\omega^2 m_2 F_1 \tag{3-30a}$$

$$q = 0 \tag{3-30b}$$

$$a = -\omega^2(b_{11} + b_{v1}) \tag{3-30c}$$

$$b = -\omega^3(m_1 + A_{11} + m_2) + \omega k_{h1} \tag{3-30d}$$

$$c = b/\omega = -\omega^2(m_1 + A_{11} + m_2) + k_{h1} \tag{3-30e}$$

$$d = -a/\omega = \omega(b_{11} + b_{v1}) \tag{3-30f}$$

$$e = \omega^2 m_2[\omega^2(m_1 + A_{11}) - k_{h1}] \tag{3-30g}$$

$$f = -\omega^3 m_2(b_{11} + b_{v1}) \tag{3-30h}$$

The optimal solutions for k_{PTO} and c_{PTO} also take the same form as (3-22) and (3-24).

3.4.1 Frequency Domain Simulation

Figures 3.12 and 3.14 show the results of the frequency domain simulation using a wave period of 6s (wave frequency of 1.04 rad/s) and a wave height of 1.5m. Figure 3.12 shows a comparison of the optimal power and the power when $k_{pto} = 700{,}000$. The optimal power of the two-body WEC with the internal mass reaches the same maximum power as the submerged body case. When analyzing power using a constant PTO stiffness however, the bandwidth of power is much smaller. These results are consistent with the results in [40,41,42].

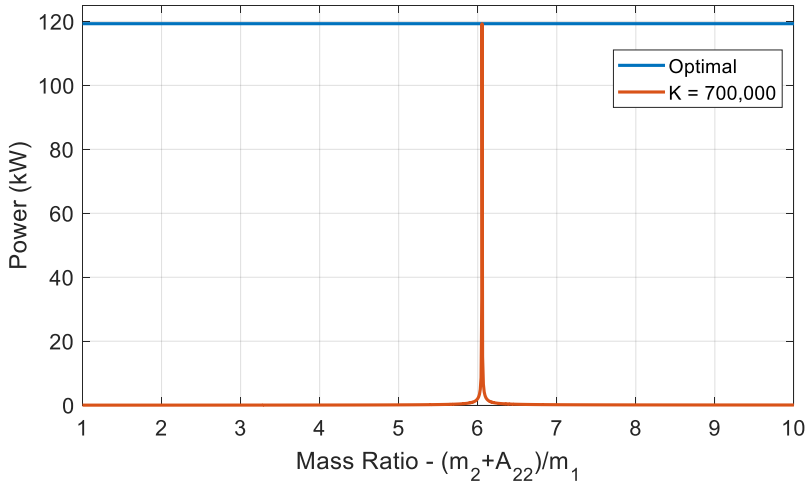

Figure 3.12 Analytically derived powers for a two-body WEC with an internal mass. The optimal power is the same as the optimal power for the submerged body case, however the bandwidth of mass ratios is much smaller.

Figure 3.13 shows the relative displacement between the floating buoy and the internal mass. While the power is optimal, the relative displacement for the WEC is unpractical. From (3-27), the mass of the submerged body can never exceed the mass of the system, so to produce similar powers as the WEC with the submerged body, the response must be large.

In Figure 3.14, we see the optimized PTO stiffness and damping. The optimal PTO stiffness steadily decreases with the mass ratio, while the optimal PTO damping steadily increases. The optimal PTO damping is also much smaller than the submerged body case, which is due to the very large relative displacement (which is due to the relatively small inner mass).

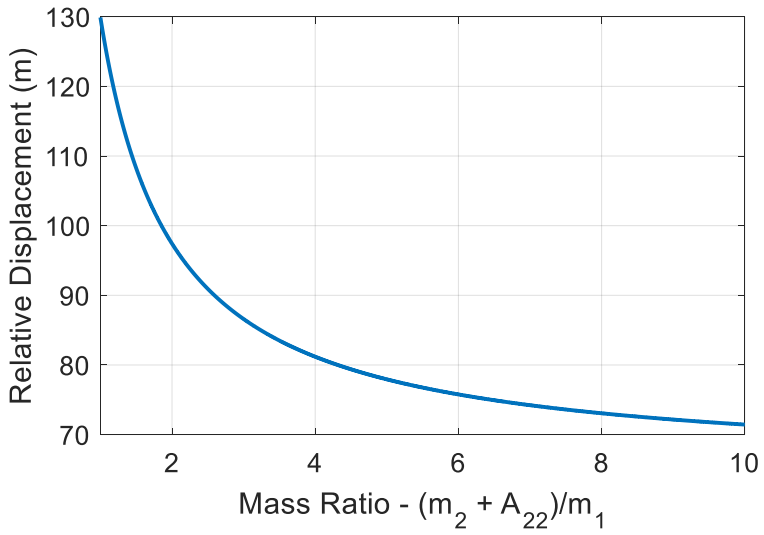

Figure 3.13 Relative displacement of two-body WEC with an internal mass.

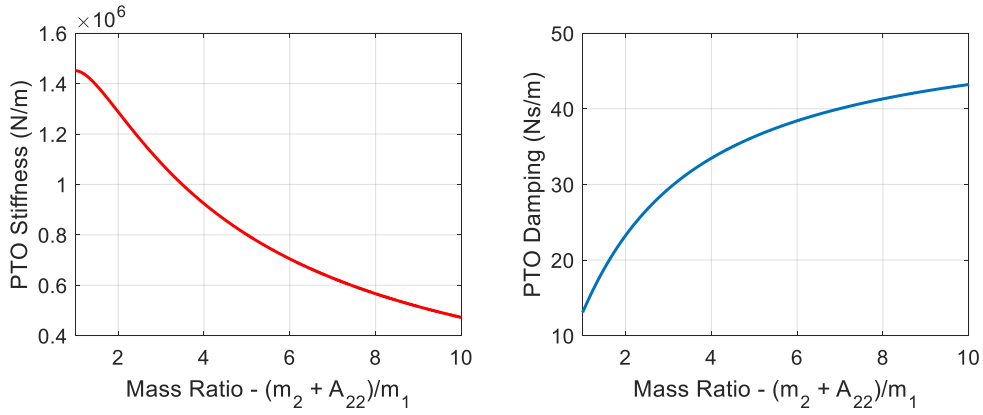

Figure 3.14 Analytically determined optimal PTO stiffness and damping for a two-body WEC with an internal mass.

In order to minimize the large relative displacement, an electromagnetic tuned-mass damper (EMTMD) can be utilized. Figure 3.15 shows the simplified dynamic model of the EMTMD. Here the PTO damping term is replaced by an electromagnetic transducer. The electromagnetic transducer can be modeled as an ideal transducer shunted with an RLC circuit, with a coil resistance R, inductance L, and capacitance C [43-45].

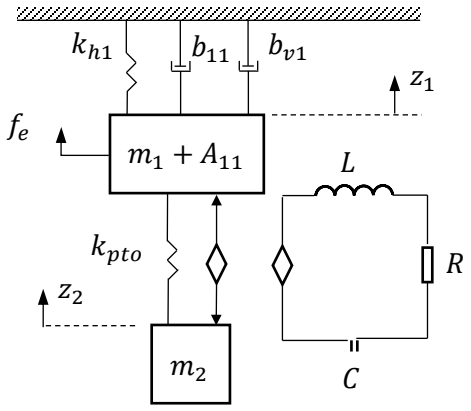

Figure 3.15 Dynamic model of the two-body WEC using an electromagnetic tuned-mass damper (EMTMD).

The relative motion between the floating buoy and inner mass produces an induced voltage:

$$e_{EMF} = k_v(\dot{x}_1 - \dot{x}_2) \tag{3-31}$$

Where the proportional gain, k_v, is the voltage constant of the transducer. The current induced by this voltage will produce a force proportional to the current:

$$F_{EMF} = k_f \dot{q} \tag{3-32}$$

Where the proportional gain, k_f, is the force constant of the transducer. Both constants are determined by the transducer properties, where $k_v = k_f$ for an ideal transducer. In the EMTMD circuit, the closed-loop voltage is zero, according to Kirchhoff's voltage law [46].

$$e_{EMF} + L\ddot{q} + R\dot{q} + \frac{1}{C}q = 0 \tag{3-33}$$

Applying (3-31) and (3-32) to the (3-28) and (3-29), the new equations of motion become:

$$(m_1 + A_{11})\ddot{x}_1 + (b_{11} + b_{v1})\dot{x}_1 + k_f\dot{q} + (k_{PTO} + k_{h1})x_1 - k_{PTO}x_2 = F_{e1} \tag{3-34}$$

$$m_2\ddot{x}_2 + c_{PTO}\dot{x}_2 + k_{PTO}x_2 - k_f\dot{q} - k_{PTO}x_1 = 0 \tag{3-35}$$

with the third equation of motion being (3-33). In [45], Liu found the optimal H_2 optimization for energy harvesting from a force excitation on a structure. His optimization technique showed that the normalized displacement could be reduced by about half. He also found that the bandwidth of optimal power was increased, due to the inductance acting as an inertial term, providing another resonant frequency. While adding an EMTMD is a next step in the inner mass two-body WEC design, reducing the displacement by half still results in relative displacements between 30m – 60m, too large

to be practical for this device. A more practical approach to this problem is to optimize the equations while changing the top buoys dimensions. As this thesis focuses on the submerged body design, this can be considered the next steps in future research work.

3.5 Summary

This chapter aimed to show the feasibility of a self-reacting resonant wave energy converter. Frequency domain models of both a single-body and two-body wave energy converter were used to find analytical solutions for optimal power. A case study for a designed floating buoy subjected to an incident wave with a wave period of 6s and wave height of 1.5m was conducted. It was found that the two-body WEC could achieve the same optimal power as a single-body WEC designed for resonance. The optimal condition, using a PTO spring stiffness, could reach the resonance condition for all sizes of the submerged body. The condition when no PTO spring stiffness was applied resulted in a single point where the system would reach resonance; this point is considered the optimal mass ratio. When applying a linear viscous drag term to the equations of motion, both conditions reach peak power at the same optimal mass ratio. This holds true for irregular waves too, indicating that the PTO spring stiffness can be excluded in the design of the WEC. To avoid the negative influences of drag, a two-body WEC with an inner mass was introduced. While this WEC can achieve the same power as the previous two, it's relative displacement is impractical. To minimize the large displacement, an electromagnetic tuned-mass damper can be utilized. Research has shown that the electromagnetic tuned-mass damper can only decrease the displacement by about half, which is still too large for practical applications. Next steps in the design of the electromagnetic tuned-mass damper include the optimization of the floating buoys structure.

4. Submerged Body Optimization in the Time Domain

4.1 Motivation

As discussed in Chapter 3, an optimal mass ratio between the top buoy and the submerged body exists for a two-body WEC. Previously, we assumed the submerged body was a shapeless mass that was deep enough where the hydrodynamic radiation damping and excitation force were negligible. For actual deployment of the WEC device, a submerged body shape must be selected. Many two-body WECs have been tested and deployed, all with varying designs. Two of the most established WEC devices are the PowerBuoy, developed by Ocean Power Technologies [20], and the Wavebob, developed by Wavebob [21]. Both WECs are similar to our design, in such that they use the relative motion between a floating buoy and a submerged body to generate electricity, however their submerged body designs are built on differing principles. The PowerBuoy uses a heave plate to maintain a relatively stationary position. While this design is advantageous to easy ocean implementation, it is designed to act like a single body WEC, the power of which we'd like to exceed. The Wavebob uses a cylindrical tank with tapered ends. While their ingenuity is not in the design of the shape itself, but their ability to control the inner mass of the tank [47], the shape will have significance to their expected output power. Beatty et al. [38] conducted experimental and numerical comparisons of the PowerBuoy and Wavebob. Their results for added mass and excitation force matched very well with numerical BEM simulations, however the total damping coefficients were much larger in the experiment. The damping component found for the heave plate design (PowerBuoy) was significantly larger than that of the cylinder design (Wavebob), indicating that viscosity plays a significant role in the submerged body design. The objective of this parametric study is to determine the influence the submerged body shape and size has on the absorption power of a two-body WEC.

4.2 Shape Optimization

The optimal mass ratio of a WEC can be achieved by manipulation of dry mass and hydrodynamic added mass of the submerged body. A simple way to achieve an optimal mass ratio is to manipulate the submerged body's added mass, which can be achieved by increasing its cross-sectional area. However, viscous force, which will be further detailed in the following section, is proportional to cross section area. The other method would be to increase the dry mass of the submerged body; however, one must take into consideration the buoyancy of the overall system. For this study, varying shapes and sizes of the submerged body, with neutrally buoyant properties, are investigated to see the influence the submerged body has on the absorption power of a two-body system. A parametric study of the shape and size of the submerged body is conducted in this section. Three shapes are considered (plate, cylinder and sphere), shown in Figure 4.1, with varying sizes to achieve similar mass ratios.

Varying sizes, detailed in Table 4.1, for each submerged body shape were analyzed to achieve a wide range of mass ratios. While the size of each shape changes, the distance between the top buoy and the submerged body remained a constant 200in (5.1m). The top buoy remained the same size for each simulation as well. The system parameters for the two-body WEC are shown in Figure 4.2.

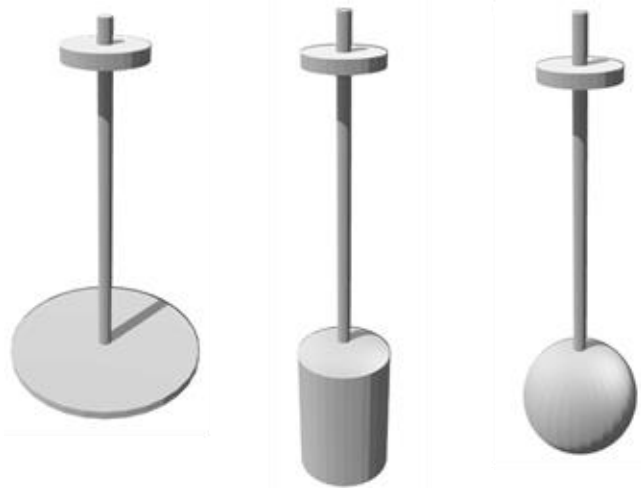

Figure 4.1 Configurations of the WEC using three different submerged body shapes; a plate, a cylinder and a sphere. The top buoy and spar length are the same for all three configurations.

Table 4.1 Submerged body sizes

Plate		**Cylinder**		**Sphere**	
Diameter	Mass	Height	Mass	Diameter	Mass
(in.)	Ratio	(in.)	Ratio	(in.)	Ratio
60	7	30	12	45	5
75	12	60	18	60	11
90	20	90	24	75	22
95	23	105	26	80	26
100	27	120	29	85	31
105	31	135	32	87.5	34
110	36	150	35	90	37
111	37	165	37	92.5	40
115	41	180	40	95	44
120	46	200	44	100	51
125	51	220	48	105	59
135	64	260	55	120	88
180	146	400	81	200	405

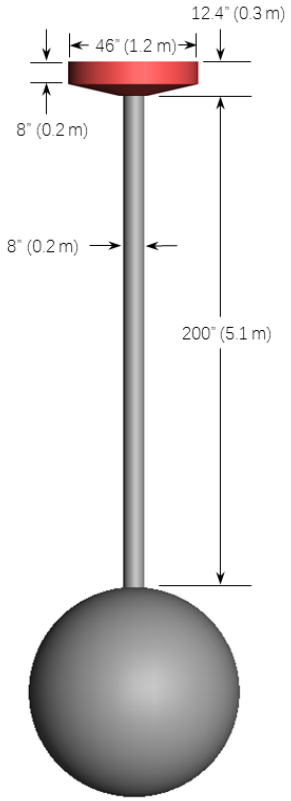

Figure 4.2 Overall two-body WEC design and dimensions with a spherical submerged body.

4.3 WEC-Sim Model

Time domain simulations were completed using the open-source simulation tool, WEC-Sim [48]. WEC-Sim is a code developed by Sandia National Laboratories and the National Renewable Energy Laboratory to model WECs subjected to operational waves in the time domain. WEC-Sims functionality has been verified with code-to-code comparisons of WaveDyn [49], ANSYS-AQWA [50], and OrcaFlex [51], and has been preliminary validated by comparison with experimental wave tank tests [Prelim Ver].

WEC-Sim was developed in MATLAB/Simulink to solve the WECs governing equations using the Cummins time-domain impulse response function formulation in six degrees of freedom [52]. The governing equations that were solved in the previous chapter, (3-11) and (3-12), can be updated to include the new radiation term based on the Cummins equation:

$$F_r(t) = -A_\infty \ddot{x} - \int_0^t K_r(t-\tau)\dot{x}(t)d\tau \tag{4-1}$$

$$K_r = \frac{2}{\pi}\int_0^\infty b_{ij}(\omega)\cos(\omega t)\, d\omega \tag{4-2}$$

where A_∞ is the added mass coefficient at infinite frequency, K_r is the radiation impulse response function, and b_{ij} is the frequency dependent hydrodynamic radiation coefficient described in Chapter 2. The convolution integral formulation of the radiation force includes the fluid memory effect on the system. As the time domain model is now non-linear, the drag force, which was previously modeled using a linear drag coefficient to keep the governing equations linear, can now be modeled using a quadratic drag term:

$$F_d(t) = -\frac{1}{2}\rho C_d A_d \dot{x}|\dot{x}| \tag{4-3}$$

where ρ is the fluid density, C_d is the drag coefficient, and A_d is the characteristic area. Substituting (4-1), (4-2) and (4-3) into (3-11) and (3-12), the governing equations can be re-written as:

$$\begin{aligned}\left(m_1 + A_{11,\infty}\right)\ddot{x}_1 + c_{pto}\dot{x}_1 + \int_0^t K_{11,r}(t-\tau)\dot{x}_1(t)d\tau + \frac{1}{2}\rho C_{1,d}A_{1,d}\dot{x}_1|\dot{x}_1| \\ + k_{h1}x_1 - c_{pto}\dot{x}_2 = F_{e1}\end{aligned} \tag{4-4}$$

$$\left(m_2 + A_{22,\infty}\right)\ddot{x}_2 + c_{pto}\dot{x}_2 + \int_0^t K_{22,r}(t-\tau)\dot{x}_2(t)d\tau + \frac{1}{2}\rho C_{2,d}A_{2,d}\dot{x}_2|\dot{x}_2| - c_{pto}\dot{x}_1 + k_{h2}x_2 = F_{e2} \quad (4\text{-}5)$$

While the quadratic drag equation is the combination of the friction (viscous) drag and form (pressure) drag, it will be dominated by form (pressure) drag. While form drag, induced by the wave profile, is considered when calculating the pressure forces on the shapes in WAMIT, the form drag from the response of the overall system is not. The WEC response will be much larger than the fluid particle response around each body, which is why the response (4-4) and (4-5) only consider the bodies velocities in the drag term.

In this study, we constrained the system to two-degrees-of-freedom (2DOF), constraining the overall system in heave, and allowing translation between the two bodies, as was done in the frequency domain model. The PTO stiffness is also set to zero, as it has no benefit in real sea states, which was determined in the frequency domain simulation. The frequency dependent hydrodynamic parameters used in WEC-Sim are calculated through WAMIT, detailed in Section 2.4. Simulations were run for both regular and irregular waves. All simulations were run using a water depth of 30m.

4.4 Regular Wave Results

In this section, the simulation results of the two-body WEC are presented under regular wave excitation using a wave period and wave height of 6s and 1.5m, respectively. Typically, drag coefficients are determined by experimental data. Without these results, it is difficult to determine an accurate drag coefficient. Therefore, various drag coefficients ($C_d = 0, 0.5, 1, 2$) were selected to investigate the effect of the drag coefficient on the system response and power absorption. Figure 4.3 shows the comparison of the three shapes with the four drag coefficients.

When there is no drag damping on the submerged body ($C_d = 0$), all three shapes have similar profiles. They each reach resonance conditions at a mass ratio of approximately 35. The power at that mass ratio exceeds the maximum power of a single body WEC (using the same top buoy as the two-body WEC). Due to unrealistic WEC motion (close to exceeding the water depth) around resonance, as well as for clarity of other simulation data, the average power is limited to 5 kW. As the mass ratio increases past resonance, the

power decreases below the maximum power of the single body WEC and becomes steady. As the submerged bodies mass increases, its motion converges to the surrounding particle velocity, which is why the power does not converge to the maximum power of the single body WEC. Submerged body frequency dependent hydrodynamic parameters for three mass ratios (26,37 and 44) are shown in Appendix A. We vary the mass ratio of the plate by manipulating the plates diameter. The influence of the increased area, normal to heave, is not only evident by the increase in added mass, but the radiation damping and excitation force as well. This influence is not as prevalent in the sphere and cylinder case, where most of the mass is achieved by increasing the volume of the shape, and thus the dry mass. The spheres diameter changes slightly, which is why we see smaller variations in the radiation damping and excitation force as the size increases, in comparison to the plate. The cylinder diameter does not change at all, which is why changes in the hydrodynamics are smallest.

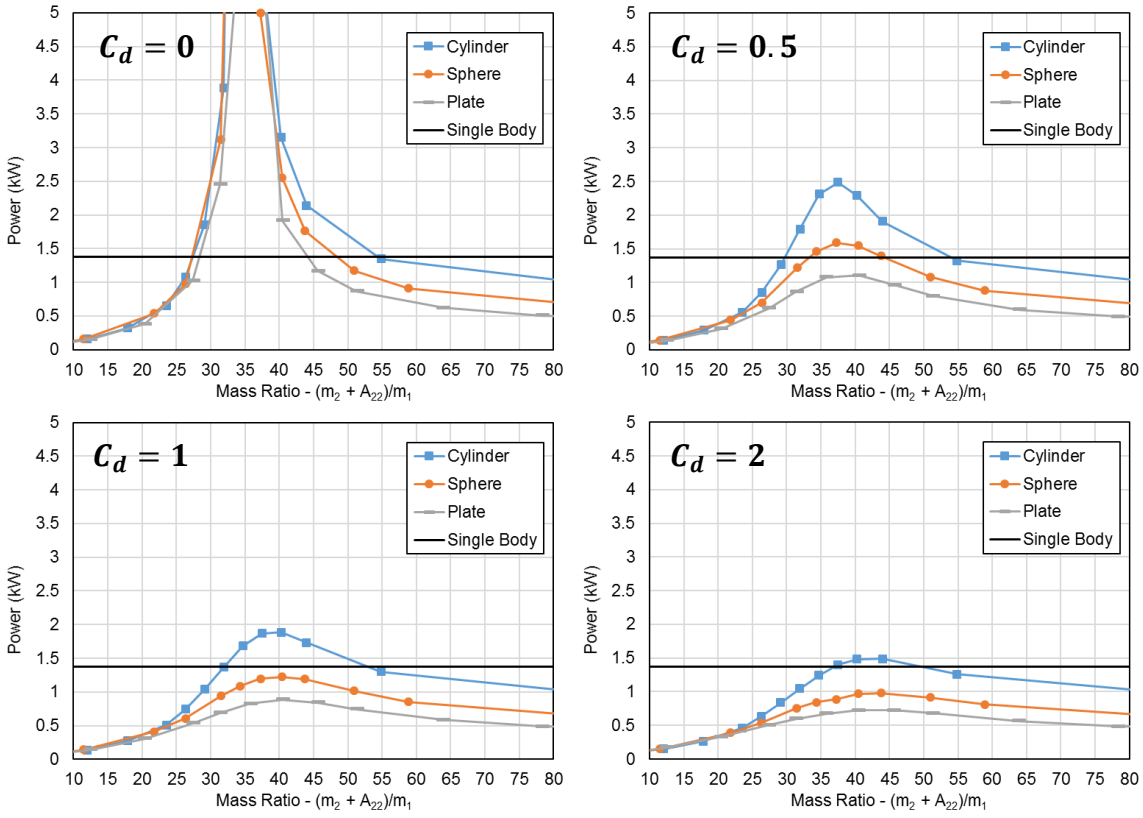

Figure 4.3 Regular wave simulations for all three shapes and comparisons to the single-body WEC power.

Adding drag damping to the submerged body decreases the power significantly. The average power of the plate design does not exceed the single body maximum power for any of the drag cases. From (4-3), not only does the drag coefficient increase the viscous drag force, the characteristic area increases it as well. As the size of the plate increases, the drag force will increase with it.

Unlike the plate, the cylinder's characteristic area remains constant. The average power of the cylinder design achieves a greater average power than the single body design for all drag cases. It is also evident that the damped natural frequency decreases with drag, as the optimal mass ratio increases with an increasing drag coefficient.

While the average power of the sphere design exceeds the single body power at low drag coefficients, it behaves more like the plate than the cylinder. To increase the mass of the sphere, the characteristic area must also increase, which increases the drag force even greater.

As discussed in section 3.2, the capture width is used to characterize the performance of WECs in waves. The capture width, which has units of meters, represents the width of wave front that contains the same amount of power that would be absorbed by the WEC. To make a fair comparison between the WECs, we calculate the hydrodynamic efficiency, or capture width ratio (CWR), obtained by dividing the capture width (μ) by the WEC width (L):

$$\bar{\mu} = \frac{\mu}{L} \tag{4-6}$$

Figure 4.4 shows the comparison of capture width ratios of the three shapes including drag. The capture width ratio of the cylinder submerged body exceeds the single-body capture width ratio for drag coefficients of 0.5 and 1, whereas the sphere and plate submerged bodies do not. What this represents is the two-body WEC with a cylindrical submerged body is more efficiency in capturing the energy from a given wave front. The capture width ratio is important when designing a wave energy farm, where multiple devices will be deployed over a larger wave front.

From the regular wave results, it can be concluded that a cylindrical submerged body, where most of the total mass is from the dry mass, is the optimal shape for a two-body wave energy converter. The cylinder, modelled as a bluff body with a drag coefficient of 2, has an equal maximum average power as the sphere with a drag coefficient of 0.5. Future

work for modelling a streamlined cylinder can be done to increase the accuracy of the model, as well as increase the power further.

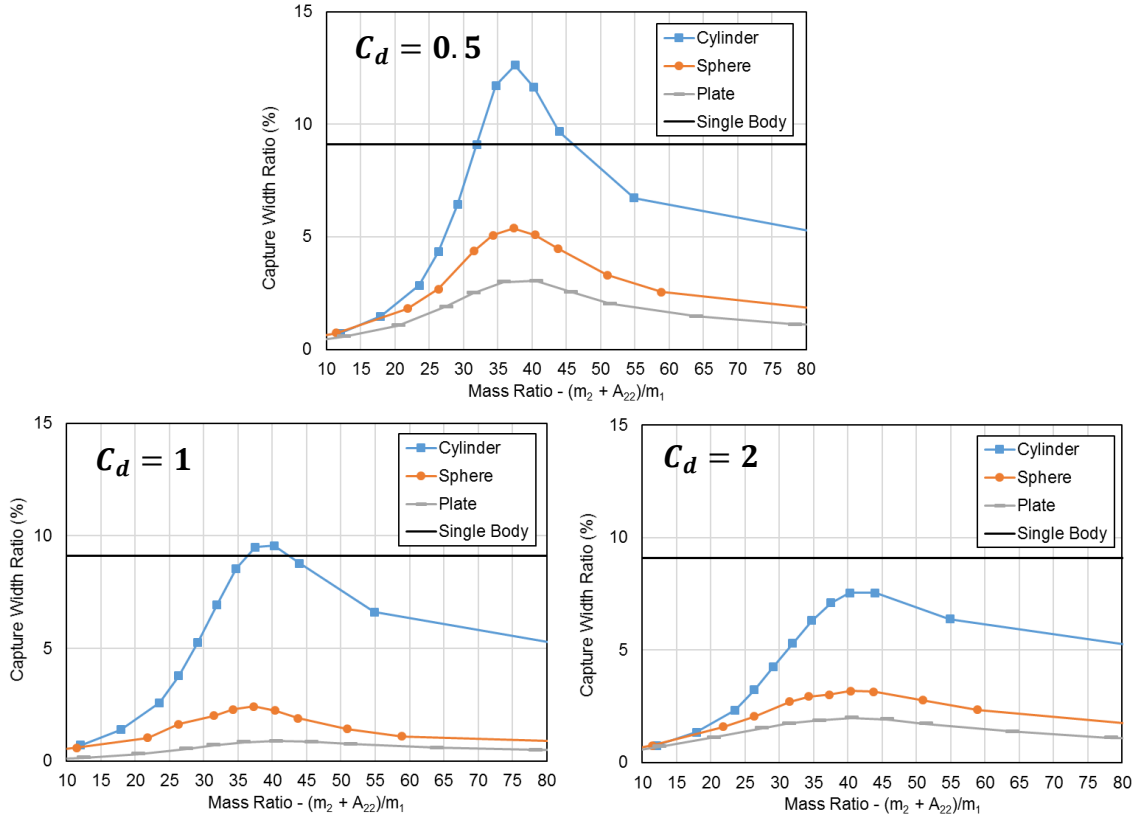

Figure 4.4 Capture width ratios for all three shapes and comparisons to the single-body WEC capture width ratio.

4.5 Irregular Wave Results

To see if our conclusion applies to real wave scenarios, irregular wave simulations using a Pierson-Moskowitz spectrum, defined in Section 2.1.3, with a peak period and significant wave height of 6s and 1.5m, respectively, were conducted. The case for no drag is not analyzed, as it is not realistic and there is no resonance condition to observe due to the spectrum of the irregular wave. WEC-Sim models the free surface elevation of an irregular wave as the linear superposition of a number of regular waves, where the regular wave height and frequency are determined from the wave spectrum. The irregular wave excitation force is calculated by the spectrum integration, whereas in the frequency domain the average power was calculated in this manner.

$$F_e(t) = Re\left[\int_0^{\infty} F_e(\omega) e^{j(\omega t+\phi)} \sqrt{2S(\omega)}\, d\omega\right] \tag{4-7}$$

Figure 4.5 shows the comparison of the three shapes with the three drag coefficients. While the maximum average power decreases in irregular waves, the same trends that appeared in the regular wave analysis are present. The cylinder design has the greatest maximum average power, though it only exceeds the single body power for a drag coefficient of 0.5. The mass ratios are also decreased for irregular wave simulation, the optimal value being in the low to mid 20s. Looking at Appendix A, we see higher frequencies have a greater influence on the submerged body hydrodynamics. As (4-7) is calculated using the spectrum integration over all frequencies, the effects of the higher frequencies will be prevalent in the average absorbed power. While the submerged body has a positive influence in regular waves at a desired frequency, careful consideration of the submerged body design must be considered to have the best influence over the spectrum of wave frequencies.

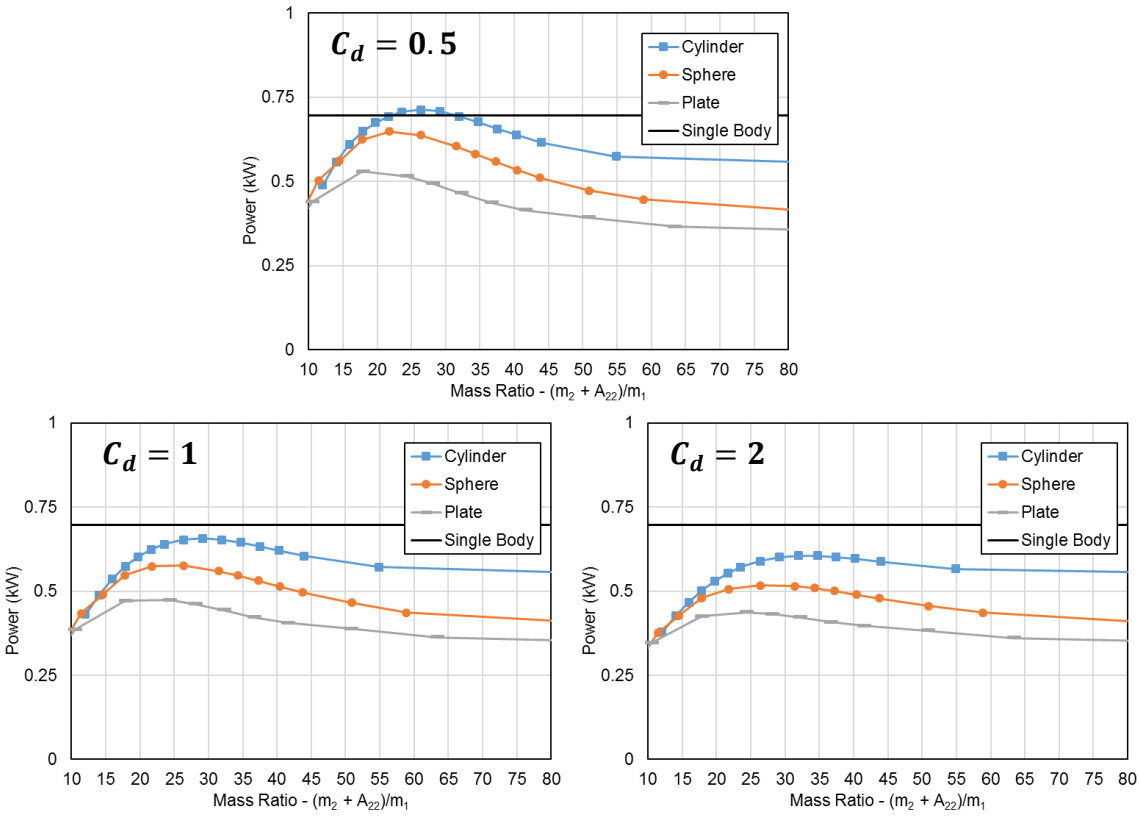

Figure 4.5 Irregular wave simulations for all three shapes and comparisons to the single-body WEC power.

4.6 Summary

The shape of the submerged body on a two-body wave energy converter is studied in this chapter. For this study, varying shapes and sizes of the submerged body were investigated to see the influence the submerged body had on the absorption power of a two-body system. Three different submerged body shapes were investigated; plate, cylinder and sphere. Simulations were completed for both regular and irregular wave conditions. The existence of an optimal mass ratio that was found in the frequency domain has been verified in the time domain simulations as well. For the specified wave energy converter design, the optimal mass ratio in regular waves (period of 6s and wave height of 1.5m) occurred at approximately 35, which is what was found in the frequency domain as well. It is found that when drag is not accounted for, the power of the two-body system will achieve resonance. However, not accounting for drag effects is unrealistic, as the response of the system becomes unstable. Various drag coefficients were selected to investigate the effect of the drag coefficient on the system response and power absorption. It was found that when drag is included in the model, the cylinder design performs the best, exceeding the power of the sphere and plate for all drag cases. It is also evident that the hydrodynamic terms we neglected in the frequency domain for the submerged body do indeed influence the absorption power. The increased area normal to heave not only increases the added mass, but the radiation damping and excitation force as well. This is evident past the optimal mass ratio for the no drag case, where the absorbed powers converge below that of the single body design.

To see the performance in real waves, irregular wave simulations using a Pierson-Moskowitz spectrum were completed. While the maximum average power was decreased in irregular waves, the same trends that appeared in the regular wave analysis were present. Again, the cylinder design performed the best. The optimal mass ratios were also decreased to approximately 20 – 25. From these results, it can be concluded that a cylindrical submerged body, where most of the total mass is from the dry mass, is the optimal shape for a two-body wave energy converter. Future work for modelling and designing a streamlined cylinder can be done to further decrease the drag coefficient, which will increase the accuracy of the model, as well as the average absorbed power.

5. Wave Tank Experimental Testing

5.1 Motivation

Experimental wave tank tests were performed to understand the hydrodynamic and power performance of the wave energy converter and power takeoff system designed by Virginia Tech. The objective of these tests was to provide experimental data to validate and improve our numerical simulations, which is based on linear wave theory.

5.2 Experiment Setup

5.2.1 Wave Basin Setup

The wave tank at the University of Maine's Alfond W2 Ocean Engineering facility, built and commissioned by Edinburgh Designs, was used to perform testing. The wave tank is 30m long, 9m wide and 5m deep. The tank features a 16-paddle flap-type wavemaker and a parabolic beach system designed to minimize wave reflections using minimal space. A bridge on top of the wave tank was used for model setup. Figure 5.1 shows the tank layout and general dimensions. A reference wave probe and the scaled model were placed 4.88m and 11.15m from the wavemaker, respectively. Before testing, waves were calibrated using the reference wave probe and two additional wave probes (in place of the scaled model). Since the wave field in the wave tank is non-uniform, the wave profile is calibrated for a "sweet spot" in the tank (where the model is located). The reference wave probe remains in place during testing to ensure the tests match the calibration, while the two additional wave probes are replaced with the model.

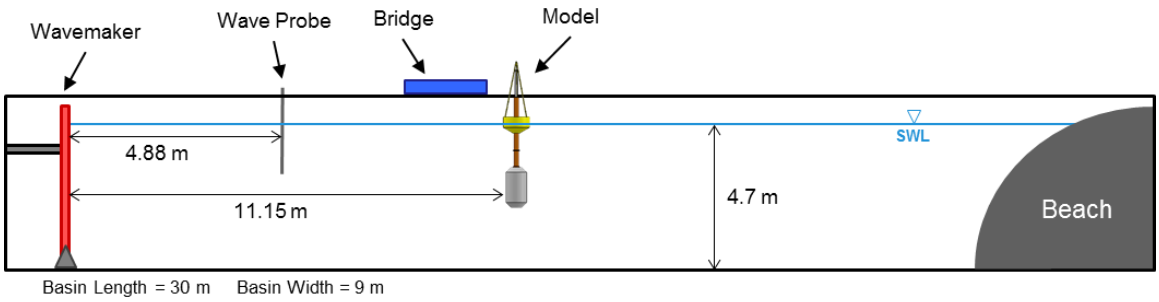

Figure 5.1 Wave tank layout and dimensions

5.2.2 Scaling

As the wave tanks dimensions are limited, a scale model is required to investigate the behavior of the WEC and PTO system. The Froude number is a dimensionless number defined as the ratio between the inertial force and the gravitational force.

$$Fr = \frac{inertial\ force}{gravitational\ force} \propto \frac{\rho U^2 l^2}{\rho g l^3} = \frac{U^2}{gl} \tag{5-1}$$

Since surface waves are gravity driven, ensuring equality of the Froude number will ensure wave forces are properly scaled [53]. Froude scaling assumes the Froude number, Fr, is constant between the model and the full-scale. Using a geometric scale, s, between the model and the full-scale, and assuming the acceleration due to gravity, g, is constant, the particle velocity is scaled by $\sqrt{s}$.

$$\frac{U}{\sqrt{l}} = \frac{U_s}{\sqrt{l_s}} = \frac{U\sqrt{s}}{\sqrt{sl}} \tag{5-2}$$

Other scaled quantities can be found in Table 5.1, which use the same principle as (5-2).

Table 5.1 Froude scaling factors

	Quantity	**Scaling**
Wave	Height and Length	s
	Period	$s^{0.5}$
	Frequency	$s^{-0.5}$
	Power Density	$s^{2.5}$
Model	Linear Displacement	s
	Linear Velocity	$s^{0.5}$
	Linear Acceleration	1
	Mass	s^3
	Force	s^3
	Power	$s^{3.5}$
	Linear Stiffness	s^2
	Linear Damping	$s^{2.5}$

5.2.3 Model Setup

A 1:30 scale model, Figure 5.2, of the proposed WEC and PTO system, designed by Virginia Tech, was tested at the University of Maine's Alfond W^2 Ocean Engineering facility. The 1:30 scale was selected to accommodate the wave tank capabilities, so as to

match the scaled waves with the full-scale waves we wanted tested. The model consists of a floating buoy, a PTO column (which houses the PTO components), and a submerged body, which is connected to the bottom of the PTO column. During setup, additional buoyancy was added to keep the submerged body afloat while additional weight was added to the bottom to stabilize it. All outer components (Buoy, PTO Column and Submerged Body) were built with Aluminum. The device dimensions are shown on the left of Figure 5.2, where the red dot is the center of gravity (CG) of the floating buoy, and the green dot is the CG of the submerged body (including the PTO column). A breakdown of the physical properties for the floating buoy and the submerged body is given in Table 5.2.

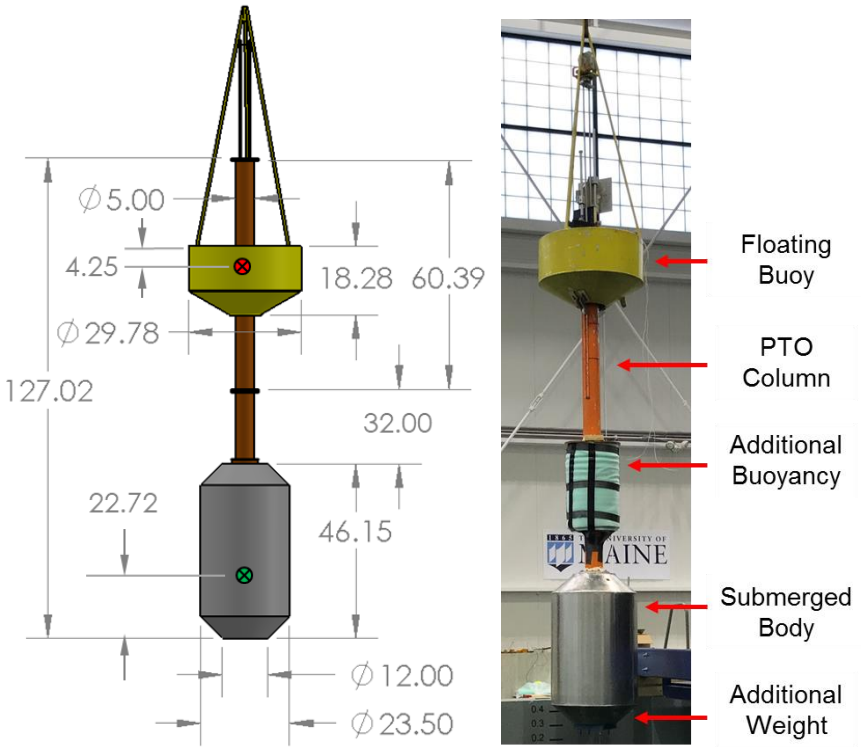

Figure 5.2 Dimensions and layout of the 1:30 scale WEC

Table 5.2 Properties of the 1:30 scale WEC

1/30th Scale Model	Floating Buoy	Submerged Body
Mass (kg)	60.1	334.2
Center of Gravity (in. from bottom)	14.03	22.72
Pitch Period (sec.)	2.87	3.54
Pitch Moment of Inertia (kg-m^2)	29.1	410.7

Three configurations of the 1:30 scale model were tested: a single-body (1DOF) heave only test, a two-body (2DOF) heave only test, and a six degree of freedom (6DOF) test.

5.2.4 Single Heave Only Test

The purpose of the 1DOF test is to measure the PTO performance without any effects from the submerged body. This is to ensure that any irregularities between the experiment and the simulation can be characterized by either PTO behavior or WEC behavior. To achieve heave only testing, the PTO column was clamped to a cross bar above the wave tank and the floating buoy was constrained to heave through linear guide rails along the PTO column. Figure 5.3 shows the layout of the 1DOF model. A potentiometer was used to measure the relative displacement between the buoy and the PTO column. A load cell was used to measure the force exerted by the buoy on the PTO push rods. This force is the PTO force, F_{PTO}, in (3-11) and (3-12). A DC generator, placed at the bottom of the PTO column, generates voltage from the relative motion of the buoy. The generator was connected to a resistive load, which acts as the PTO damping component. The data from the potentiometer, load cell, and generator were then processed by the University of Maine's National Instruments PXI-e chassis data acquisition system (DAQ).

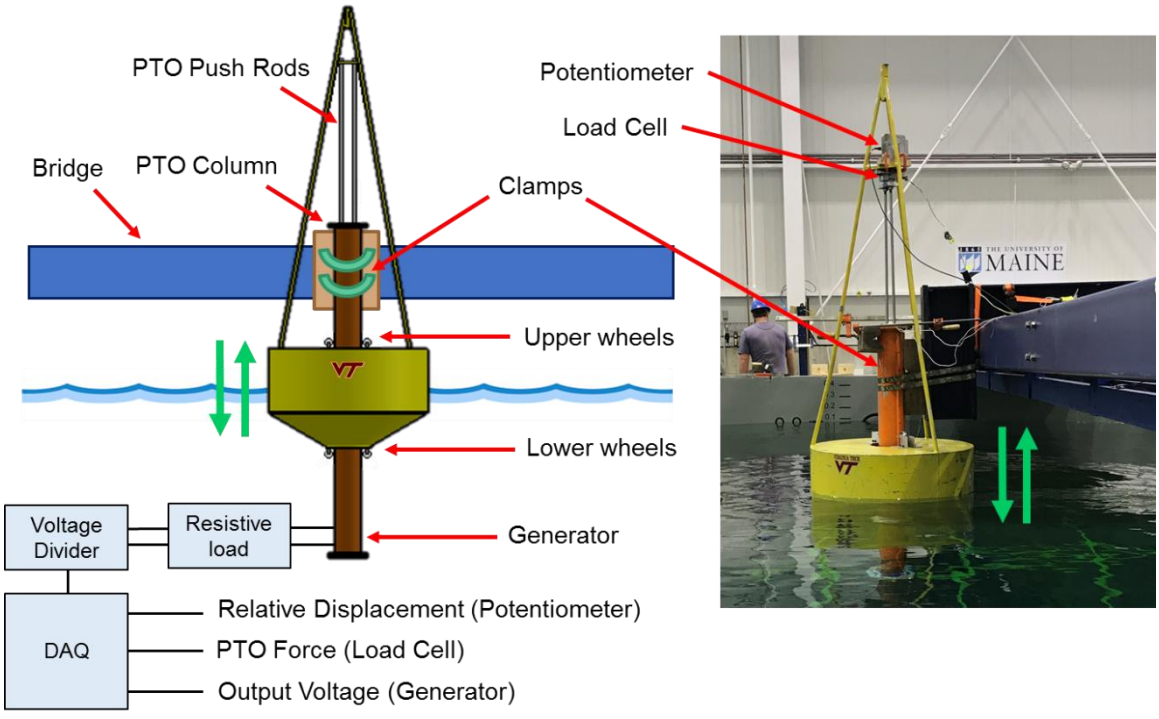

Figure 5.3 Schematic layout and actual deployment of 1DOF model

5.2.4 Two-Body Heave Only Test

The next step is to include the submerged body. Here we will see the effects the submerged body has on the PTO performance. The 2DOF test enables us to measure the performance of the two-body WEC without instability issues. If instability issues are present during 6DOF testing, the 2DOF test allows us to compare the performance between the two configurations. This will be helpful in future designs and in full-scale deployment. To constrain the device to heave only, a linear guide system was designed to constrain the PTO column to heave motion only. Like in the 1DOF model, the floating buoy was constrained to heave through linear guide rails along the PTO column. During testing, it was found the wheels on the top of the buoy were over-constraining the device and were taken off. Both the potentiometer and load cell were used in the 2DOF test to measure relative displacement and force, respectively. In addition to the potentiometer, a Qualisys motion capture system [54] was used to measure the motion of each body. The Qualisys system uses active cameras to measure 6DOF motions of passive markers, which that are placed on the floating buoy and the submerged body. Figure 5.4 shows the layout of the 2DOF model.

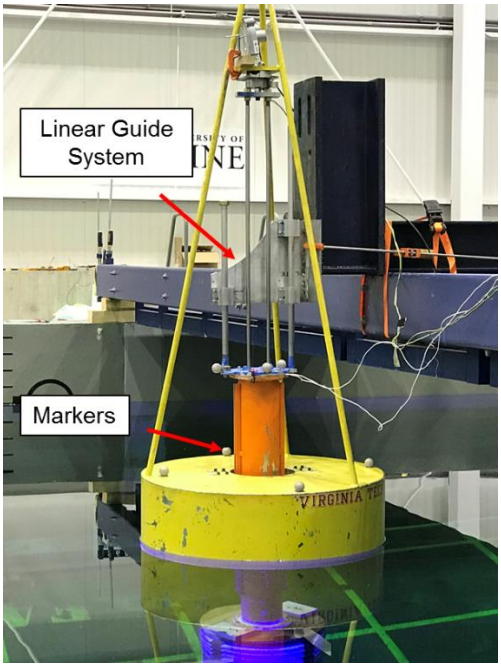

Figure 5.4 Deployment of 2DOF model

5.2.5 Six Degree of Freedom Test

The purpose of two-body 6DOF testing is to measure both WEC and PTO performance in six degrees of freedom (seven degrees of freedom between both bodies). The previous two configurations are good for characterizing the PTO performance, but do not reflect how the overall system will perform in realistic scenarios. The behavior of the WEC in 6DOF is important for full-scale deployment of the device. The mooring system for the 6DOF model can be seen in Figure 5.5. The design of the mooring system used taut lines oriented such that they controlled the mean offset of the model to prevent large motions that may interfere with power cables from the device, as well as prevent collisions with the bridge and tank basin. The three mooring lines, equally spaced ~120° apart, consisted of monofilament lines attached to springs. Each mooring line was then connected to the buoy through a load cell, allowing us to measure the tension on the lines. The picture on the left of Figure 5.5 shows the actually 6DOF buoy setup with the mooring lines highlighted by the yellow lines, while the picture on the right shows an aerial view of the mooring configuration.

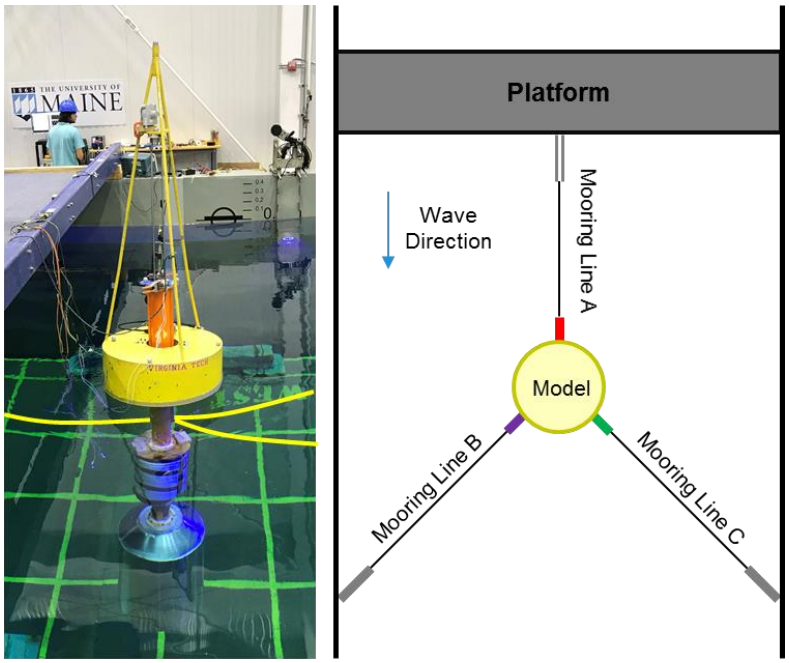

Figure 5.5 Deployment of 6DOF model and schematic layout of the mooring system

5.2.4 Wave Tests

The test waves were adapted from the DOE Wave Energy Prize's [55] 1:50 scale model testing. Taking the full-scale wave conditions, we adapted them based on Froude scaling to match our 1:30 scale model. In total, 10 wave conditions were performed on each condition, 7 of which were regular monochromatic (mono) waves, and 3 of which were irregular polychromatic (poly) waves. The monochromatic waves were kept at a constant wave steepness of 1:80. Each monochromatic test was run for four minutes. The polychromatic waves were created using a Bretschneider spectrum [25], an expansion of the Pierson-Moskowitz spectrum:

$$S(\omega) = \frac{5}{16} {H_s}^2 \frac{{f_p}^4}{f^5} exp\left\{-\frac{5}{4}\left(\frac{f_p}{f}\right)^4\right\} \quad (5\text{-}3)$$

Each polychromatic test was run for thirty minutes. Table 5.3 lists the test cases that were performed on each configuration of the device. Due to internal friction in the model, test runs M1, M2, M3 and P1 resulted in no response.

Table 5.3 Sea states tested

Run	Test Name	Wave Type	Dir. (°)	1/30th Scale		Full Scale	
				Period (s)	Height (m)	Period (s)	Height (m)
1	M1	Mono	0	1.10	0.023	6.00	0.70
2	M2	Mono	0	1.28	0.032	7.00	0.96
3	M3	Mono	0	1.46	0.042	8.00	1.25
4	M4	Mono	0	1.64	0.053	9.00	1.58
5	M5	Mono	0	1.83	0.065	10.00	1.95
6	M6	Mono	0	2.01	0.079	11.00	2.36
7	M7	Mono	0	2.19	0.094	12.00	2.81
8	M8	Mono	0	2.37	0.110	13.00	3.30
9	M9	Mono	0	2.56	0.128	14.00	3.83
10	M10	Mono	0	2.74	0.146	15.00	4.39
1	P1	Poly	0	1.06	0.058	5.80	1.75
2	P2	Poly	0	1.63	0.083	8.95	2.50
3	P3	Poly	0	2.83	0.173	15.50	5.20
4	P4	Poly	0	2.08	0.045	11.40	1.35

5.3 Power Takeoff Design

As described in Section 1.2, the PTO "is the single most important element in wave energy technology" [12]. The key mechanism of the PTO tested here is the mechanical motion rectifier (MMR), which converts the bi-directional linear relative motion of the floating buoy and submerged body into uni-directional rotation [56]. Figure 5.6 shows the configuration of the PTO system. PTO push rods, which are directly connected to a ball nut, transfer the force between the floating buoy and submerged body. The ball nut moves in a bi-directional linear motion and drives a ball screw in a bi-directional rotation. A coupling transfers the ball screws rotation to the input shaft, which is connected to the MMR gearbox. Two one-way bearings are installed in opposite directions around the input shaft, each of which transfers motion in one direction. If the input shaft is rotating in the positive direction, the bottom clutch will engage and the rotation will directly transfer to the output shaft. If the input shaft is rotating in the negative direction, the top clutch will engage, transferring the rotation to a series of bevel gears where the rotation will be rectified to the output shaft. In this way, the generator will rotate in one direction.

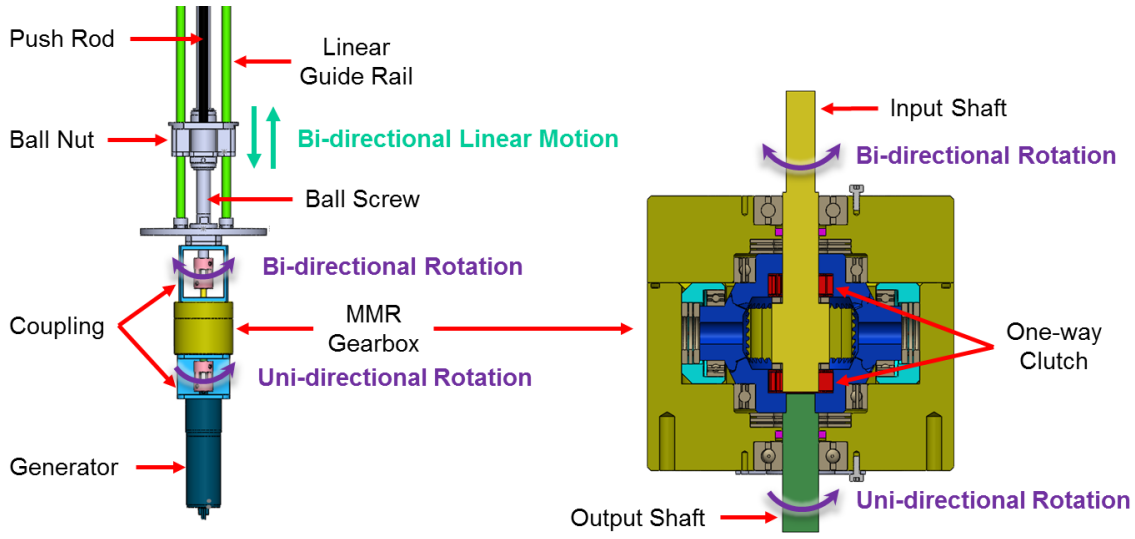

Figure 5.6 Configuration of the PTO system and MMR gearbox

Due to the inertia effect of the generator, there may be times when both clutches are disengaged, leading to a non-linear PTO force term. When the rotation speed of the output shaft is equal to the rotation speed of the input shaft, $\omega_{output} = \dot{x}_{nut} n_g$, the system is considered engaged, and the equation of motion can be express as:

$$(m_{nut} + m_e)\ddot{x}_{nut} = F_{PTO} - c_e\dot{x}_{nut} \tag{5-4}$$

However, when the rotation speed of the output shaft is greater than the rotation speed of the input shaft, $\omega_{output} > \dot{x}_{nut}n_g$, the system is considered disengaged, resulting in two decoupled equations:

$$m_{nut}\ddot{x}_{nut} = F_{PTO} \tag{5-5}$$

$$m_e\dot{\omega}_{output} + c_e\omega_{output} = 0 \tag{5-6}$$

where m_e is the equivalent mass of the generator and c_e is the equivalent damping of the PTO, defined as:

$$m_e = J_g{n_g}^2 \tag{5-7}$$

$$c_e = \frac{k_t k_e {n_g}^2}{(R_i + R_e)} \tag{5-8}$$

where m_{nut} is the mass of the ball nut, x_{nut} is the displacement of the ball nut, F_{PTO} is the PTO force exerted on the ball nut, ω_{output} is the rotational speed of the output shaft, J_g is the moment of inertia of the generator, n_g is the gear ratio of the ball screw, k_t and k_e are generator constants, and R_i and R_e are the internal and external resistances of the generator, respectively. Simulations for the MMR PTO can be seen in Figure 5.7. When disengagement happens, the rotation speed of the output shaft (MMR) is greater than the input shaft (non-MMR), and the PTO force becomes zero. While in reality the PTO force would not be zero due to the inertia of the ball nut, we assume the ball nuts mass is small in the simulation.

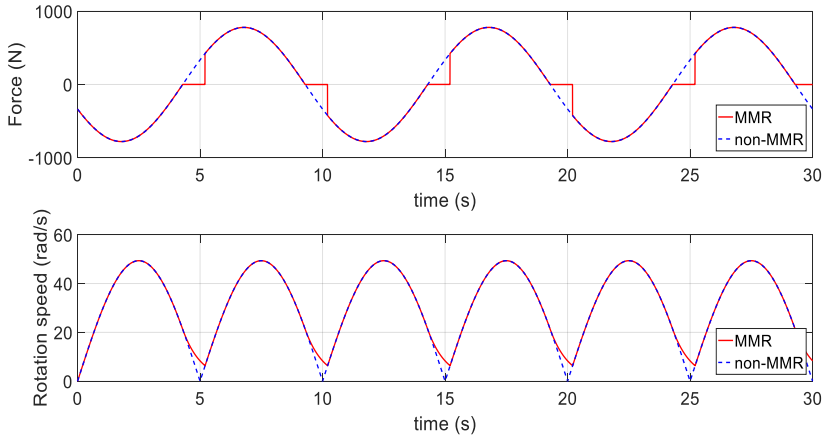

Figure 5.7 Simulation of the disengagement effect of the MMR

To achieve the disengagement effect of the MMR, the equivalent mass must be high enough to achieve a greater inertia than the inertia of the ball nut on the input shaft. This is typically achieved by including a flywheel in the design, however the scale of our model does not allow for the inclusion of said flywheel. During experimental testing, it was noticed that the disengagement effect of the MMR was hard to measure, or simply never occurred. To simplify our simulation of this experiment, we assume the MMR is always engaged (which decreases the run time of the simulation significantly).

5.4 Experimental Results

5.4.1 Data Processing

Before evaluating the test results, the higher frequencies from the DAQ are attenuated from the raw data using a low-pass 4th order Butterworth filter [57], with a cutoff frequency of 20 Hz. After filtering the data, the electrical and mechanical power from the PTO are calculated. Instantaneous electrical power is the power dissipated by the external resistance, R_e, at a specific time, where voltage is constant.

$$P_{elec} = \frac{(V_{out})^2}{R_e} \tag{5-9}$$

Due to the use of a voltage divider, as well as the inner impedance of the DAQ, the voltage supplied to the DAQ, V_{DAQ}, is not the output voltage of the generator. To calculate the output voltage, we can multiple by the voltage divider constant, D.

$$V_{out} = D \cdot V_{DAQ} \tag{5-10}$$

For this circuit, $D = 2.5$. Voltage, however, is a time-varying function, and the average power must be found using the RMS voltage, V_{rms}.

$$V_{rms} = \sqrt{\frac{1}{N}\sum_{n=1}^{N} |V_{out}(t)|^2} \tag{5-11}$$

The average electrical power from the generator can be found by substituting the RMS voltage for the output voltage in (5-9).

$$P_{avg|elec} = \frac{(V_{rms})^2}{R_e} \tag{5-12}$$

Average mechanical power is the time average of the mechanical work done by the PTO force, defined as:

$$P_{avg|mech} = \frac{dW}{dt} = \frac{\int_{T_1}^{T_2} F_{pto}\, dx}{T_2 - T_1} \tag{5-13}$$

This average mechanical power is the power of WEC before running through the PTO. It can be considered the maximum achievable power of the WEC design ($\eta_{PTO} = 100\%$). The overall efficiency of the PTO, η_{PTO}, can be calculated as the ratio between the average electrical power and the average mechanical power.

$$\eta_{PTO} = \frac{P_{avg|elec}}{P_{avg|mech}} \tag{5-14}$$

The PTO efficiency is the product of two efficiencies, the generator efficiency and the MMR efficiency (which includes the ball screw efficiency).

$$\eta_{PTO} = \eta_{gen} \cdot \eta_{MMR} \tag{5-15}$$

The maximum generator efficiency is the ratio of the external resistance and the total resistance (inner and external). While other losses, such as friction and windage losses, can be prevalent in DC generators, they are typically much smaller than the losses due to the internal resistance. Thus, we assume our generator efficiency is:

$$\eta_{gen} = \frac{R_e}{R_i + R_e} \tag{5-16}$$

Due to spacing restrictions inside the PTO column, there was no way to measure the output speed of the MMR gearbox. To find the efficiency of the MMR system (including the ball screw), we take the ratio of the PTO efficiency and generator efficiency.

5.4.2 Decay Tests

Decay tests are performed to determine the hydrodynamic parameters of both the floating buoy and the submerged body. A decay test involves releasing a body (floating buoy or submerged body) from an initial position in still water. From these tests, the added mass and radiation damping coefficient of each body can be found.

Each decay test response is characterized by a free damped oscillation, with the mathematical solution:

$$x(t) = Xe^{-\zeta\omega_n t}\sin(\omega_d t + \varphi) + C \tag{5-17}$$

where X is the amplitude of the response, ζ is the damping ratio, ω_n is the natural frequency, ω_d is the damped natural frequency, φ is the phase, and C is a constant that represents the difference between the data's zero point and the body's equilibrium position. Using MATLAB, the solution for (5-17) is solved for both the floating buoy and submerged body. The added mass and radiation damping coefficient are then determined using the following equations:

$$\omega_n = \sqrt{k_h / m + A} \tag{5-18}$$

$$\zeta = \frac{b}{2\omega_n(m + A)} \tag{5-19}$$

$$\omega_d = \omega_n\sqrt{1 - \zeta^2} \tag{5-20}$$

A sample of the decay tests for the floating buoy and submerged body, compared against their fitted curves based on (5-17), can be seen in Figure 5.8. The hydrodynamic parameters calculated from these tests are tabulated in Table 5.4. The hydrodynamic parameters of the floating buoy match well with the parameters obtained by WAMIT, however the parameters of the submerged body indicate there is additional added mass and radiation damping on the submerged body. The additional added mass is likely due to the uneven layer of foam added to the PTO column. While this geometry was taken into account in the MultiSurf model, it was assumed to be a flat cylinder, whereas the bottom of the foam was uneven and allowed for water to fill between the layers. The increased radiation damping can be attributed to drag damping, which is not assumed in linear wave theory. Because the PTO column has such a small cross-section area at the SWL, the radiated wave calculated by linear wave theory is small.

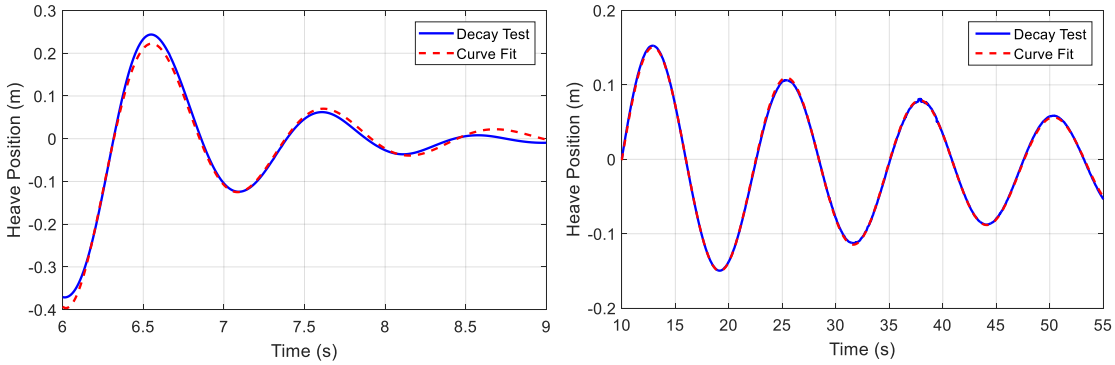

Figure 5.8 Heave decay tests of both the floating buoy (left) and submerged body (right), and their fitted curves

Table 5.4 Hydrodynamic parameters determined from decay test

Body	Parameter	Decay Test	Simulation
Floating Buoy	Added Mass (kg)	50.63	53.94
	Radiation Damping (Ns/m)	248.15	218.73
Submerged Body	Added Mass (kg)	151.55	90.81
	Radiation Damping (Ns/m)	22.78	1.75

5.4.3 Single Degree of Freedom – Regular Waves

The purpose of the single-body heave only testing is to measure the PTO performance without any effects from the submerged body. This is to ensure that any irregularities between the experiment and the simulation can be characterized by either PTO behavior or WEC behavior. Figure 5.9 on the left shows the mechanical power from the tests compared with the optimal analytical and numerical solutions for regular wave tests M4 through M10. Seven different external resistances values, $R_e = [4, 5, 7, 10, 20, 40]$ ohms, were tested for each regular wave run. While the mechanical power of the experiments follows the same trends as both simulation results, the optimal PTO damping values, Figure 5.9 on the right, for the experimental results are much lower. Additional sources of damping must be present in the experiment to overcome the difference in the optimal damping values.

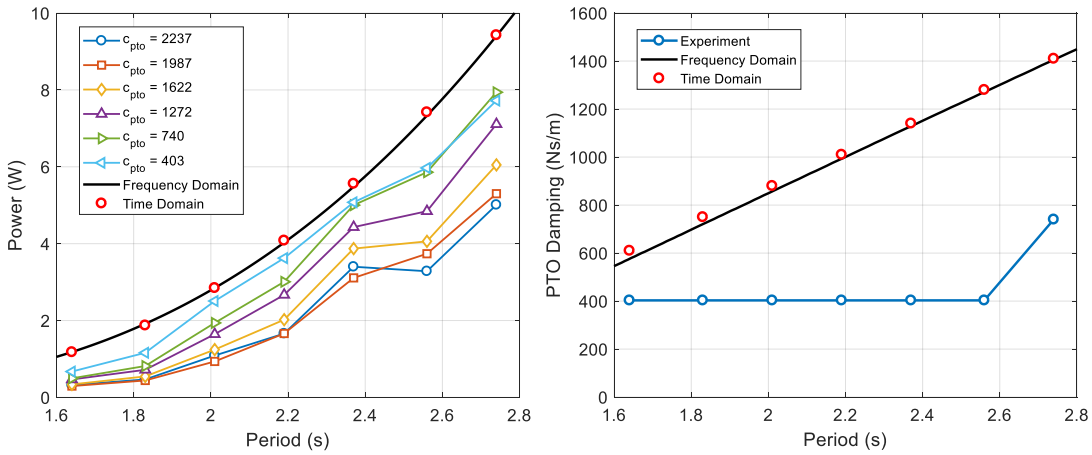

Figure 5.9 Experimental results of 1DOF model compared with frequency domain and time domain simulations. On the left, the mechanical input powers. On the right, the optimal PTO damping values.

To minimize the friction of the initial setup, another set of tests was conducted using a similar setup to the 2DOF test. Instead of using the straps to clamp the PTO column to the bridge, the PTO column was held stationary using stoppers on the linear guide system

of the 2DOF model. In this way, the friction between the spar and the floating buoy is reduced. Figure 5.10 on the left shows the mechanical power from the tests compared with the optimal analytical solutions for regular wave tests M7, M9 and M10. The mechanical power is slightly increased for all cases and now exceeds the optimal power of the simulation. The cause of this increased power is due to friction internal to the PTO.

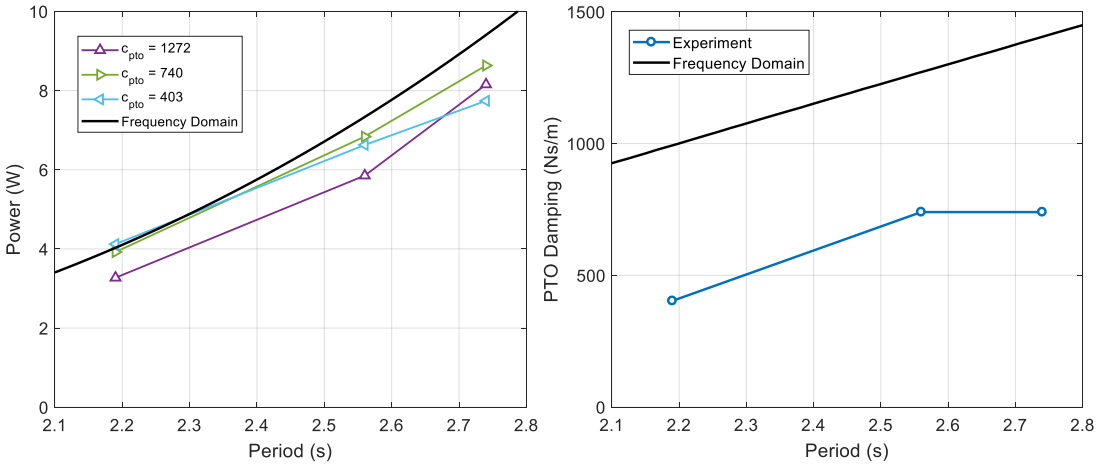

Figure 5.10 Experimental results of second 1DOF model setup compared with frequency domain simulations. On the left, the mechanical input power. On the right, the optimal PTO damping values.

To validate the presence of friction within the PTO, we apply a friction force, F_f, to (5-4), where $sgn(\dot{x}_{nut})$ is the signum function which extracts the sign of the velocity term. In this way, friction is always opposing the direction of motion.

$$F_{PTO} = (m_{nut} + m_e)\ddot{x}_{nut} + c_e\dot{x}_{nut} + F_f \cdot sgn(\dot{x}_{nut}) \qquad (5\text{-}21)$$

While F_f will have a negative impact on (3-2), decreasing the response, it will also have a positive impact on (5-13), increasing the mechanical power observed by the PTO load cell. This force, however, is not absorbed by the generator, (5-12), and will decrease the power out of the generator, as seen in Figure 5.11. The black line represents the optimal power from the generator assuming a maximum generator efficiency of (5-16). Assuming the generator is operating at similar efficiencies during the test, most of the inefficiencies are coming from the MMR, which can be characterized as friction from the ball screw and MMR gearbox.

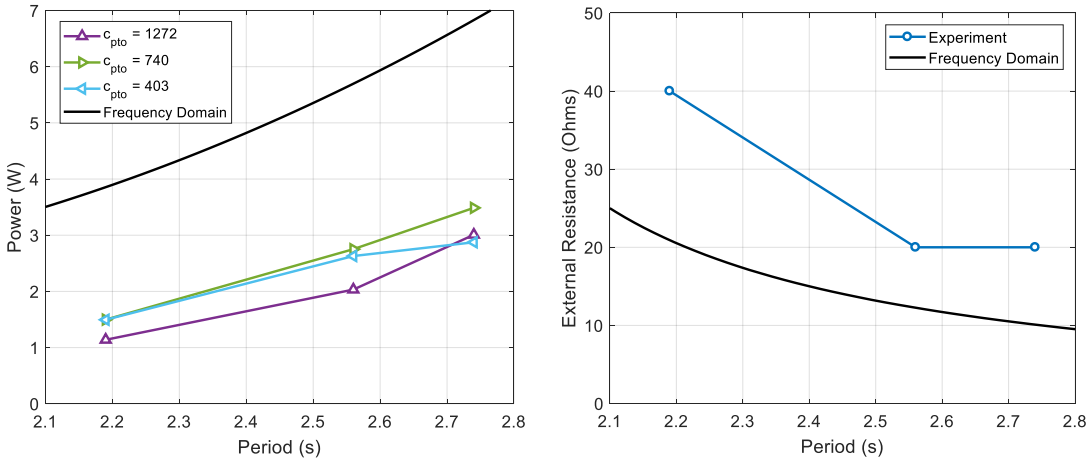

Figure 5.11 Experimental results of second 1DOF model setup compared with frequency domain simulations. On the left, the electrical output power. On the right, the optimal external resistance.

5.4.4 Two Degrees of Freedom – Regular Waves

The next step is to include the submerged body. Here we will see the effects the submerged body has on the PTO performance. A more defined purpose of two-body heave only testing is to measure the two-body PTO performance in waves without the possibility of instability issues. If instability issues are present during multi-degree of freedom testing, the two-body heave only test allows us to compare the performance between the two configurations which will be helpful in future designs and in full-scale deployment. As was done for the 1DOF test, the 2DOF test was run for regular wave tests M4 through M10 using seven different external resistances values, $R_e = [4, 5, 7, 10, 20, 40]$ ohms. During testing, a malfunction occurred in the power electronics causing the power in test M4 for $R_e = 20$ ohms to be exceedingly large and is not included in this analysis. Figure 5.12 on the left shows the mechanical power from the tests compared with the optimal analytical and numerical solutions (both simulations assume no drag). The experimental results match well with the simulations results, with the exception of test M8. Test M8 (period of 2.37s) has a lower power output than test M7 (period of 2.19s) for all cases of damping. Our simulations, however, show that the model should achieve resonance at this period.

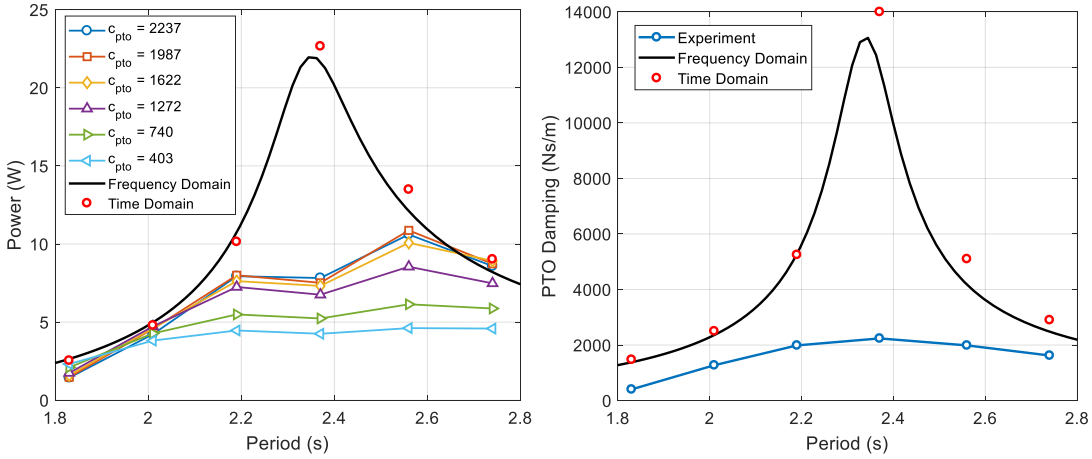

Figure 5.12 Experimental results of 2DOF model compared with frequency domain and time domain simulations. On the left, the mechanical input powers. On the right, the optimal PTO damping values.

Comparing the optimal PTO damping to the experimental PTO damping, Figure 5.12 on the right, we see that the external resistance used is not small enough to achieve the optimal damping from the simulation. Using a constant external resistance in the simulation ($R_e = 5$), and comparing it to the experiment with the same constant resistance, as shown in Figure 5.13, the power still reaches a peak at 2.35s. This indicates that the issue is not caused by the external resistance being too low.

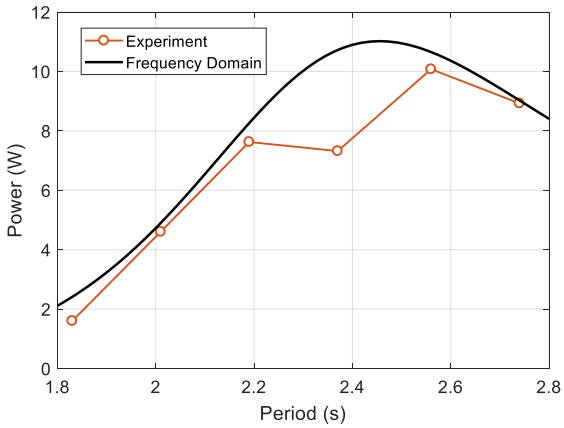

Figure 5.13 Comparison of experiment and frequency domain simulation using a constant external resistance of 5 ohms.

Comparing the displacements of the floating buoy (top) and submerged body (bottom) of the experiment to the simulation, Figure 5.14, we see similar trends as the power curve. At M8, the amplitudes of displacement for both the floating buoy and submerged body are significantly lower than expected, indicating the wave height for test M8 is lower than expected. Simulating the response using the wave height of test M7 and the wave period

of test M8, we get almost identical responses as the experiment. While the generated wave height remains unchanged, the reflections from the side walls may be generating a standing wave at the model. Since M8 is a resonance point, the model will radiate a wave equal to M8's wavelength, approximately 8.8m. Since the wavelength at M8 is approximately 9m, the dimension of the wave tank, a standing wave is possible. While it is not possible to determine if this is the case, the simulation is in agreement that the wave height at the model has been affected for this particular wave period. Future simulation work to characterize this reduction in wave height is suggested, especially the modeling of the side walls, to test the hypothesis of a standing wave.

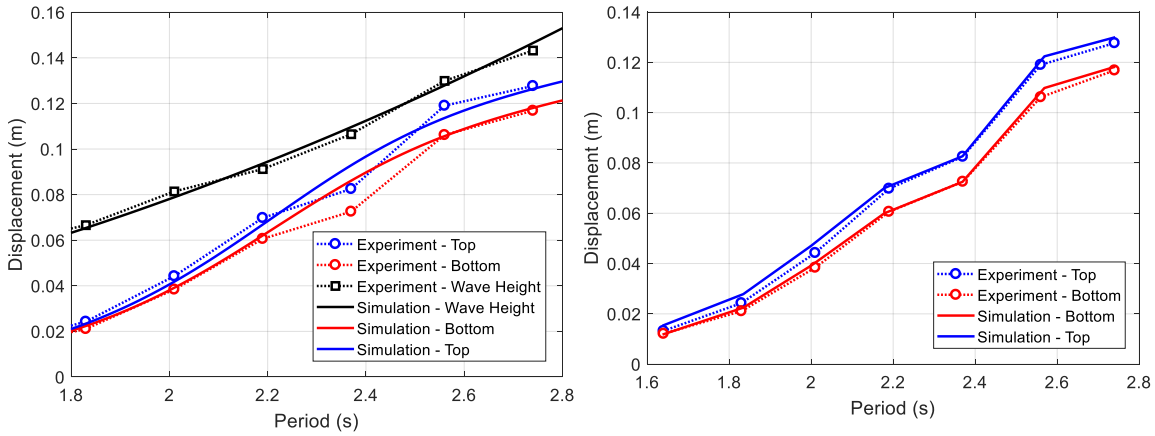

Figure 5.14 Comparison of floating buoy (top) and submerged body (bottom) simulated and experimental displacements. The left plot shows the simulation values assuming a constant steepnes of 1:80. The right plot shows the simulation values replacing M8's height.

The power shown in Figure 5.15 is the mechanical input power to the PTO, which is the maximum capable power of the device, assuming a 100% efficient PTO. The inefficiencies of the PTO and generator will not only have a significant influence on the output electrical power, but on the optimal PTO damping (external resistance). From Figure 5.15, we see that the overall PTO efficiency has an efficiency range of 20% to 45% (which is the product of the generator and MMR efficiencies). Using (5-15), the MMR efficiency is calculated to range between 35% to 60%. Because we cannot measure the actual efficiency of the generator, we assume a maximum generator efficiency of (5-16), meaning the calculated MMR efficiency is its lowest possible efficiency. From [58], dry lab testing showed MMR efficiencies up to 82%. From the efficiencies, we see a design criteria that needs to be met. While small external resistances (4 ohms and 5 ohms) produce the largest mechanical powers and MMR efficiencies, they also have the smallest generator

efficiencies. From (5-16), the generator efficiency is inversely proportional to the sum of the external and internal resistances. The generator internal resistance is 3.9 ohms, so the maximum generator efficiency for a 4 ohm external resistance is ~50%. Looking at the electrical output power, the maximum power does not occur at these low resistances, but instead at external resistance values of 7 ohms and 10 ohms, which have higher overall PTO efficiencies.

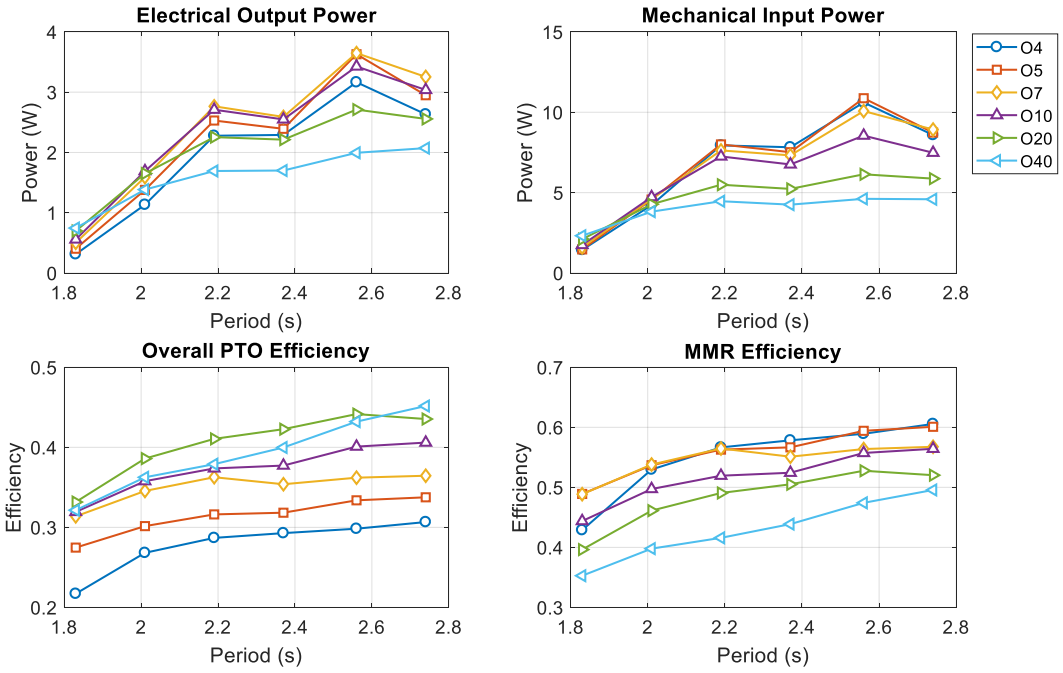

Figure 5.15 Experimental powers and efficiencies for varying external resistances (O4 - 4ohms) for the 2DOF model.

From Section 3, power is proportional to the wave height squared. Since the wave steepness is held constant, the wave height increases with increasing wave period. To make a fair comparison between wave periods, we must normalize the power, scaling it by the square of the wave height.

$$\bar{P} = \frac{P}{H^2} \tag{5-21}$$

To account for the lower wave height experienced during test M8, we use the wave height of test M4 to normalize that power. Figure 5.16 shows the scaled electrical output power from the generator and the scaled mechanical input power to the PTO. Here we see that the optimal period of this device is slightly smaller when accounting for the differences in wave height.

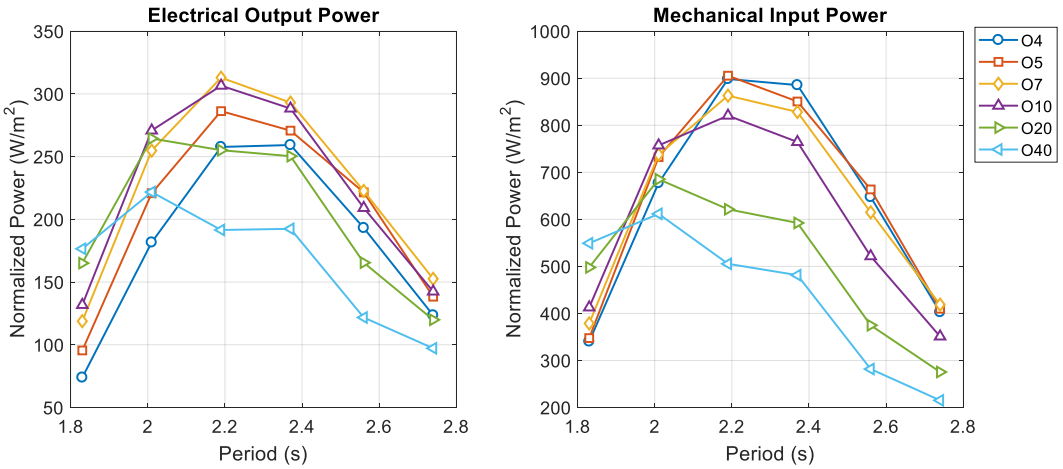

Figure 5.16 Experimental normalized power for the 2DOF model.

Comparing the 2DOF power to the 1DOF power, Figure 5.17, we see that the both the normalized electrical output power and mechanical input power are nearly doubled at the peak period (2.19s) for this device.

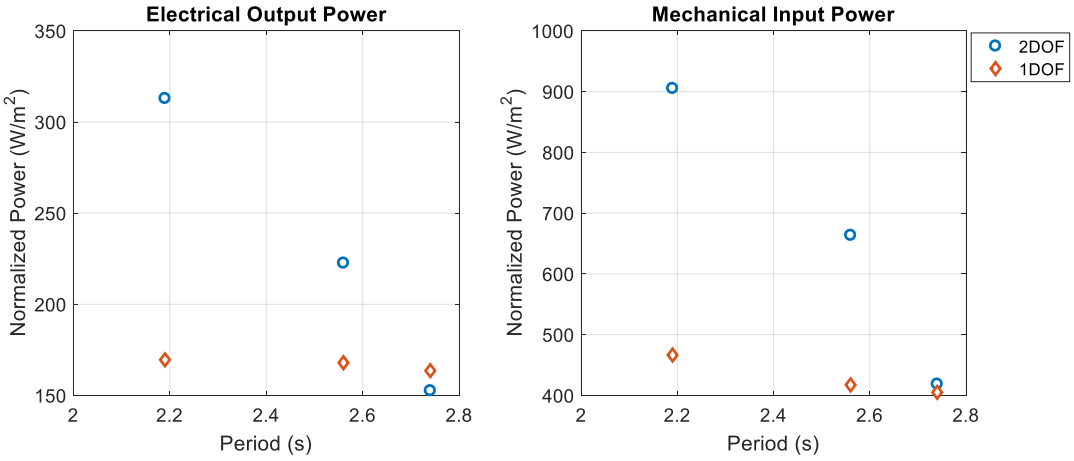

Figure 5.17 Comparison of 2DOF and 1DOF powers for M4, M6 and M7.

5.4.5 Six Degrees of Freedom – Regular Waves

The purpose of two-body 6DOF testing is to measure both WEC and PTO performance in 6DOF. The previous two configurations are good for characterizing the PTO performance, but do not reflect how the overall system will perform in realistic scenarios. The behavior of the WEC in 6DOF is important for full-scale deployment of the device. Figure 5.18 shows the electrical output power, mechanical input power, overall PTO efficiency and MMR efficiency, for the 6DOF testing. As we'd hope, the powers of the 6DOF test are very similar to the 2DOF test, however the efficiencies are much lower.

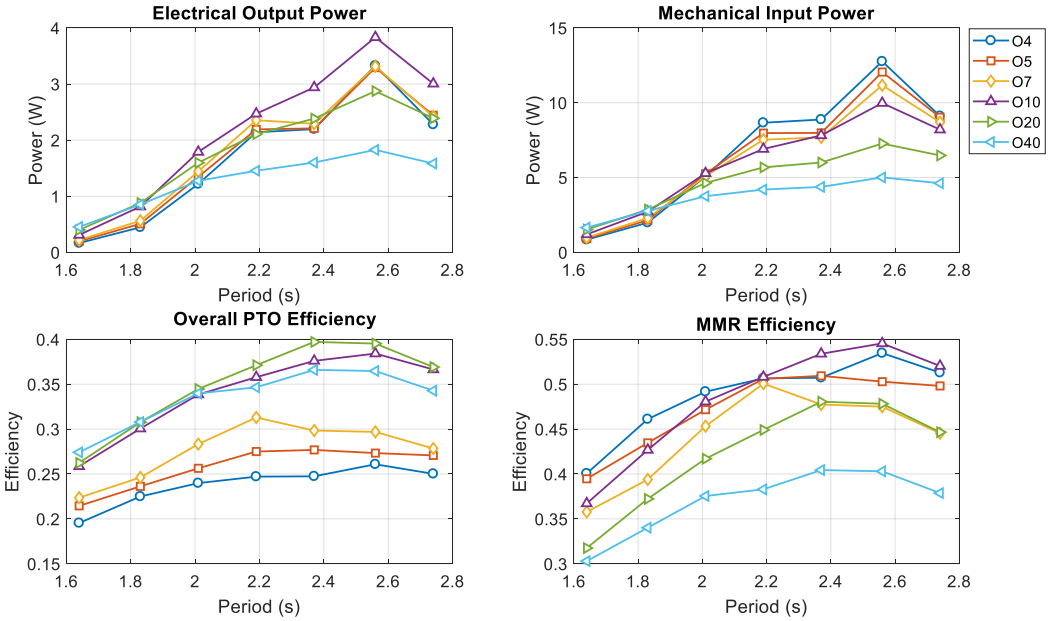

Figure 5.18 Experimental powers and efficiencies for varying external resistances for the 6DOF model.

Comparing the 6DOF power to both the 2DOF power and the 1DOF power, Figure 5.19, we see that the 6DOF normalized mechanical input power is greater than the 2DOF, yet the 6DOF normalized electrical output power is smaller. This indicates that more friction forces are present in the 6DOF model than the 2DOF model. This increased friction is due to the moments (roll, pitch and yaw), induced on the device. The floating buoy is not securely tightened to the PTO column, so as the device rotates, the push rods will twist with the buoy.

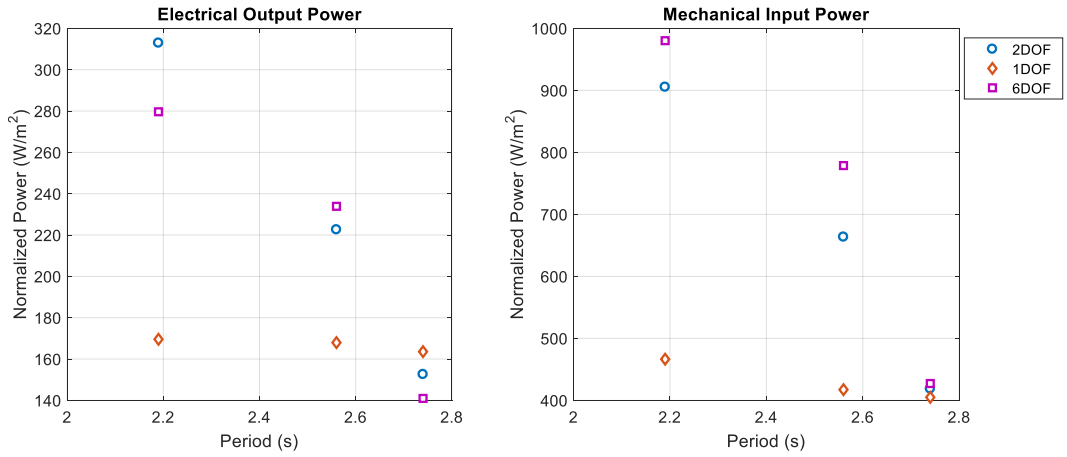

Figure 5.19 Comparison of 6DOF, 2DOF and 1DOF powers for M7, M9 and M10.

Figure 5.20 shows the angular displacements on the device for test M7 using an external resistance of 4 ohms. When designing the full-scale device, one must consider the friction when designing the constrains for 6DOF while making sure not to over-constrain the device. From these figures, we can also see the effect of the mooring lines. When the first wave hits the device, the mooring line springs cause the whole device to oscillate. This oscillation decays over time though, indicating the mooring lines only influence the transient dynamics.

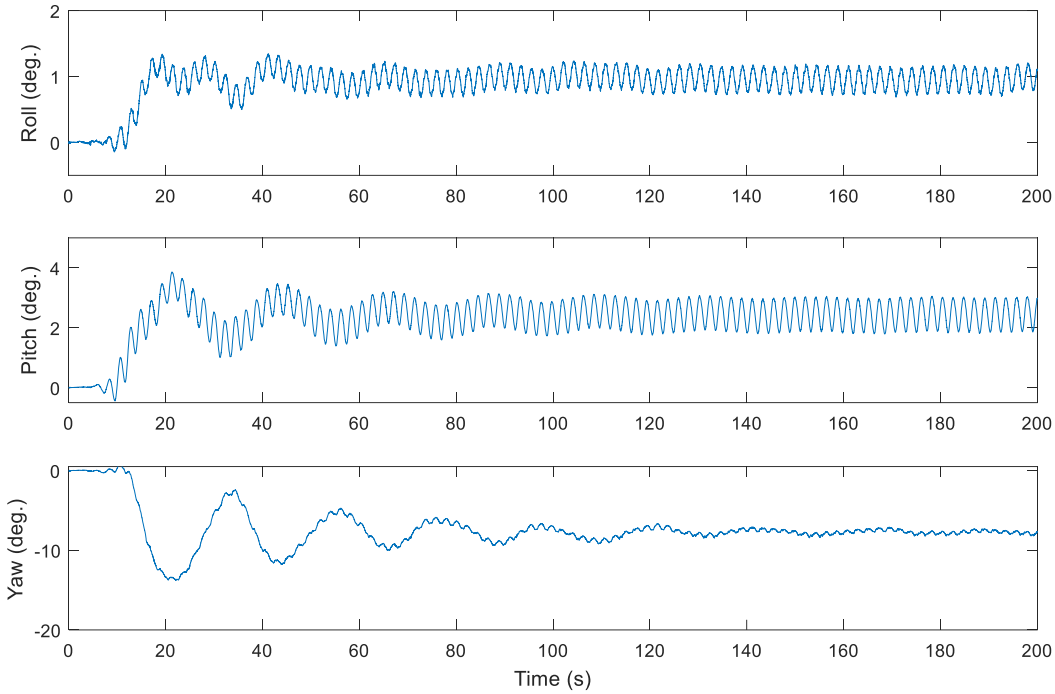

Figure 5.20 Angular displacements for test M7 using an external resistance of 4 ohms.

5.4.6 Capture Width Ratio

As was discussed in section 3.2, the capture width is used to characterize the performance of WECs in regular waves. When designing a wave energy farm, it is important to have a high capture width ratio, (4-6), in order to capture the most energy from the total wave front. The capture width ratio (electrical output power) for the 2DOF model at M7 (an equivalent full-scale wave reference of 91 kW/m) is 19.85%, while the maximum capture width ratio (mechanical input power) for the same setup and test is 57.45%. Typical capture width ratios for two-body heaving devices range from 14 – 51% for wave references of 12 – 26 kW/m [59]. Table 5.5 shows the capture width ratios for test runs M5, M6, M7, M9 and M10, for all setup configurations.

Table 5.5 Experimental capture width ratios (%) using input and output WEC power

Wave	Full-Scale Energy Flux	2DOF		6DOF	
		Elec. Output	Mech. Input	Elec. Output	Mech. Input
M5	36 kW/m	13.32	51.06	15.71	51.06
M6	59 kW/m	18.76	58.69	19.86	58.69
M7	91 kW/m	19.85	57.45	17.48	62.20
M9	196 kW/m	12.12	36.13	12.74	42.40
M10	276 kW/m	7.66	21.01	7.07	21.43

5.4.7 Irregular Waves

Real sea waves are typically very irregular due to the irregularity of the wind energy. The purpose of the irregular tests is to get a broad understanding of the WECs performance (both motion and power) in real seas, especially how the bodies responds to the irregular sea state. Three sets of irregular waves were tested using a Bretschneider spectrum, which is an expansion of the Pierson-Moskowitz spectrum, defined by (5-3). For each of the 1DOF, 2DOF and 6DOF models, only one external resistance value, the external resistance that produced the most output power, was selected. Figures 5.21 through 5.26 show the time history of irregular wave case P3 for the 2DOF model using an external resistance of 7 ohms. In Figure 5.21 and 5.22, the wave elevation is shown together with the measured floating buoy position and the submerged body position, respectively. Here we can see both the floating buoy and submerged body follow the wave quite well and will exceed the given wave height often. Figures 5.23 through 5.26 show the comparison of the experimental data with the simulated data. The experiment follows the simulations very well, however the experiment does not respond to smaller changes in wave height, as the simulation does. This indicates additional damping to the system from internal friction is delaying the response time of the buoy. To increase the accuracy of the model, the internal friction of the WEC should be characterized, which can be done more accurately in dry lab testing. Tables 5.6 and 5.7 display the absorbed powers for each irregular test in each configuration. Table 5.6 compares the mechanical input power of the experiment to the simulation. The irregular run, P3, for the 1DOF test performed as expected, however runs P2 and P4 produced no motion. The irregular runs for the 2DOF test performed slightly worse than the simulations, but followed the trends as the simulations. The slight decrease in performance is expected, as constraining the device to heave only will add external friction to the device. The irregular runs for the 6DOF test performed better than the

simulations. As stated before, there is more internal PTO friction in the 6DOF configuration due to the bending PTO push rods. This is evident in Table 5.7, where the efficiency of the PTO in the 6DOF is lower than the 2DOF efficiency. From these irregular rests, it is clear that the two-body WEC can produce more power (~30%) than the single-body WEC.

Table 5.6 Simulated and experimental mechanical output power for irregular waves

Wave	1DOF (20 ohms)		2DOF (7 ohms)		6DOF (7 ohms)	
	Sim.	Exp.	Sim.	Exp.	Sim.	Exp.
P2	--	--	1.1164	0.7688	0.8971	0.9972
P3	5.2312	5.2456	6.5229	6.4175	6.5204	7.1897
P4	--	--	0.4347	0.3508	0.4502	0.5101

Table 5.7 Electrical input power and overall PTO efficiency for irregular waves

Wave	1DOF (20 ohms)		2DOF (7 ohms)		6DOF (7 ohms)	
	Power	Eff.	Power	Eff.	Power	Eff.
P2	--	--	0.2467	32.09%	0.3157	31.65%
P3	2.0413	38.89%	2.6110	40.69%	2.4847	34.56%
P4	--	--	0.1024	29.19%	0.1449	28.40%

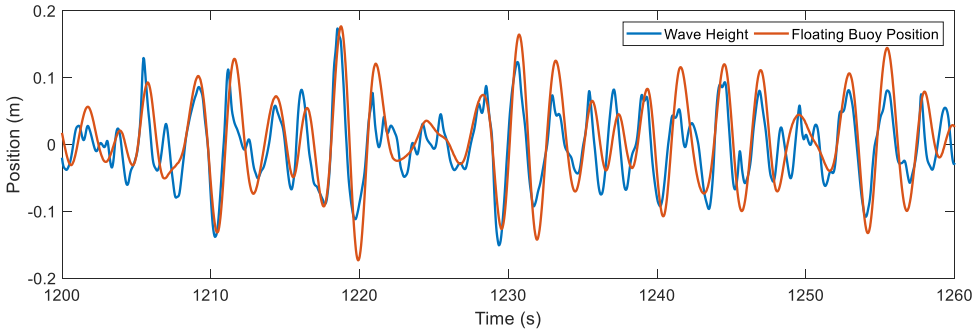

Figure 5.21 Wave height and measured floating buoy position.

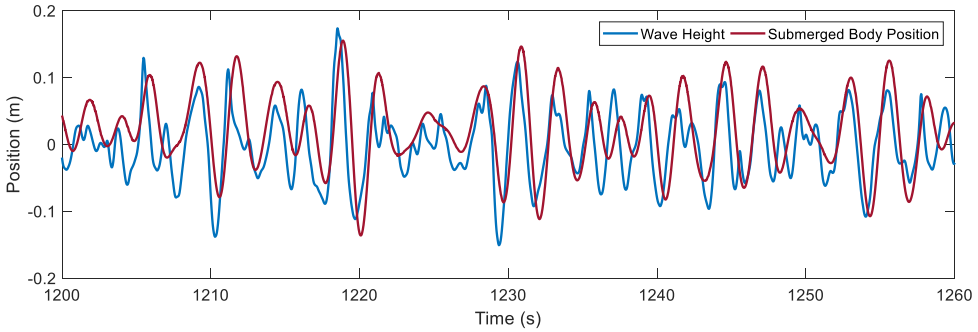

Figure 5.22 Wave height and measured submerged body position.

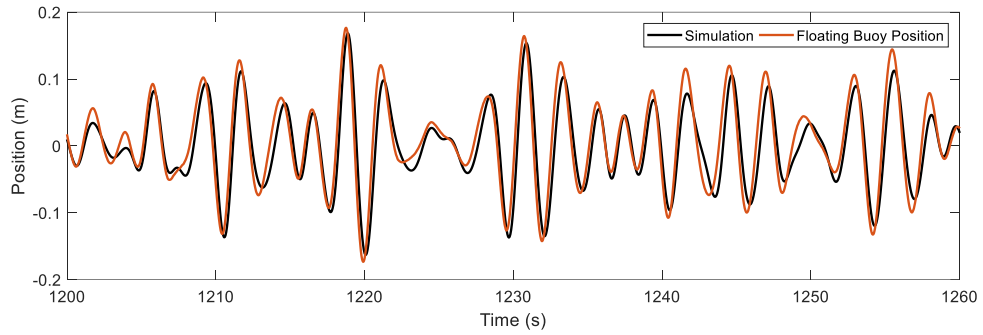

Figure 5.23 Simulated and measured floating buoy position.

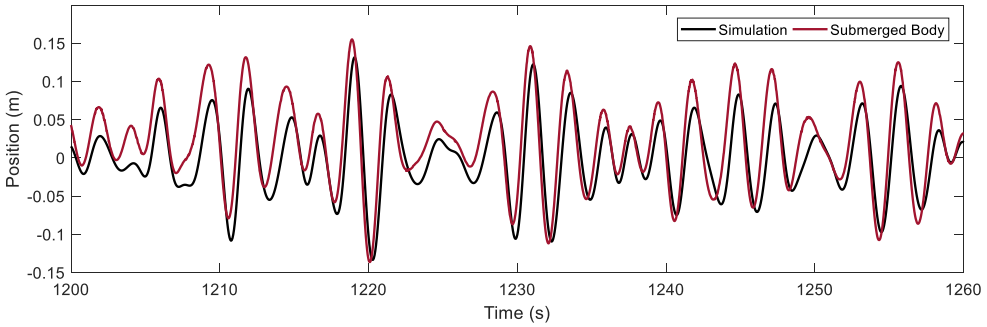

Figure 5.24 Simulated and measured submerged body position.

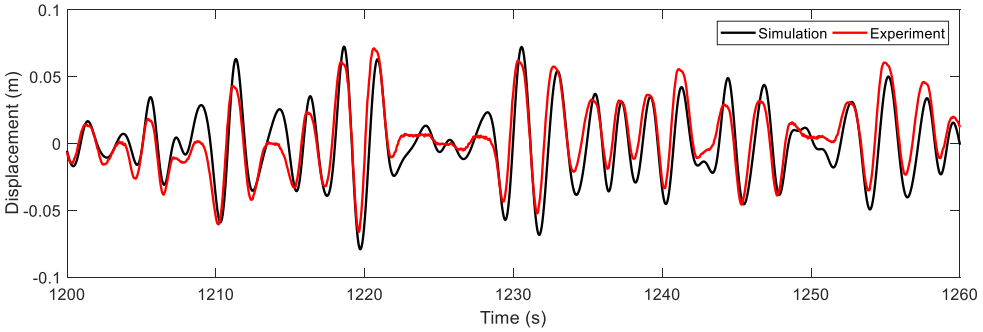

Figure 5.25 Simulated and measured relative displacement of the WEC.

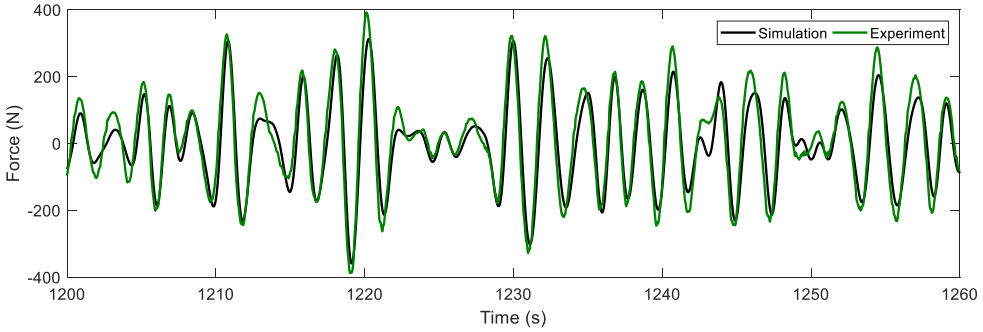

Figure 5.26 Simulated and measured force on the PTO.

5.5 Summary

In this chapter, a 1:30 scale model of the proposed WEC and PTO system, designed by Virginia Tech, was tested at the University of Maine's Alfond W^2 Ocean Engineering facility. Three configurations of the 1:30 scale model were tested: a single-body (1DOF) heave only test, a two-body (2DOF) heave only test, and a six degree of freedom (6DOF) test. The purpose of the 1DOF test was to ensure that any irregularities between the experiment and the simulation could be characterized either by the PTO behavior or the WECs behavior. Here it was found that the friction internal to the PTO has a significant effect on the power. Due to the presence of friction, the measured PTO force is slightly larger than simulated, making the calculated mechanical power of the WEC larger. This power however is being absorbed by friction and decreases the power output from the generator. When designing the full-scale device, consideration of the internal PTO components must accounted for in order to maximize the efficiency of the PTO.

The purpose of the 2DOF test was to measure the two-body PTO performance in waves without the possibility of instability issues. If instability issues are present during multi-degree of freedom testing, the two-body heave only test allows us to compare the performance between the two configurations which will be helpful in future designs and in full-scale deployment. The experimental results of the 2DOF test matched well with the simulations results, with the exception of regular wave test M8. Here, the device performed as if the wave height was decreased while the wave period remained the same. Since M8 is a resonance point, the model will radiate a wave equal to M8's wavelength, approximately 8.8m. Since the wavelength of M8 is approximately 9m, the dimension of the wave tank, a standing wave could be generated, affecting the wave height at the model. While it is not possible to determine if this is the case, the simulation is in agreement that the wave height at the model has been affected for this particular wave period. Future simulation work to characterize this reduction in wave height is suggested, especially the modeling of the side walls test the hypothesis of a standing wave.

The previous two configurations were good for characterizing the PTO performance, but do not reflect how the overall system will perform in realistic scenarios. The behavior of the WEC in 6DOF is important for full-scale deployment of the device. As we'd hope, the powers of the 6DOF test were very similar to the 2DOF test. The efficiencies of the

6DOF test are lower however. Due to moments (roll, pitch and yaw) induced on the device, the PTO push rods will have increased torsion, leading to misalignment, and finally increased friction. For full-scale development, careful consideration of the PTO design is needed to prevent misalignment while making sure the device is not over-constrained.

While regular wave tests are insightful to characterize resonance conditions and sources of inefficiencies, they do not provide an accurate depiction of real sea waves, which are typically very irregular due to the irregularity of the wind energy. Three sets of irregular waves were tested using a Bretschneider spectrum for all three configurations of the model. The purpose of the irregular tests is to get a broad understanding of the WECs performance (both motion and power) in real seas. From these tests, we saw both the floating buoy and submerged body follow the wave quite well and will exceed the given wave height often, meaning the WEC responds well to irregular seas. These results are in good agreement with our simulated results, indicating our irregular wave model is accurate. From these irregular rests, it is clear that the two-body WEC can produce more power (~30%) than the single-body WEC.

6. Conclusion and Future Work

In this thesis, a two-body 'point absorber' type wave energy converter with a mechanical power-takeoff was investigated. Frequency domain models of both a single-body and two-body wave energy converter were used to find analytical solutions for optimal power. A case study for a designed floating buoy subjected to an incident wave with a wave period of 6s and wave height of 1.5m was conducted. It was found that the two-body WEC could achieve the same optimal power as a single-body WEC designed for resonance. The optimal condition, using a PTO spring stiffness, could reach the resonance condition for all sizes of the submerged body. The condition when no PTO spring stiffness was applied resulted in a single point where the system would reach resonance; this point is considered the optimal mass ratio. When applying a linear viscous drag term to the equations of motion, both conditions reach peak power at the same optimal mass ratio. This holds true for irregular waves too, indicating that the PTO spring stiffness can be excluded in the design of the WEC. To avoid the negative influences of drag, a two-body WEC with an inner mass was introduced. While this WEC can achieve the same power as the previous two, it's relative displacement is impractical. To minimize the large displacement, an electromagnetic tuned-mass damper can be utilized. Research has shown that the electromagnetic tuned-mass damper can only decrease the displacement by about half, which is still too large for practical applications. Next steps in the design of the electromagnetic tuned-mass damper include the optimization of the floating buoys structure.

A case study involving the optimization of three different submerged body shapes was conducted using time-domain analysis. For the specified wave energy converter design, the optimal mass ratio in regular waves (period of 6s and wave height of 1.5m) occurred at approximately 35, which is what was found in the frequency domain as well. It is found that when viscosity is not accounted for, the power of the two-body system will achieve resonance. However, not accounting for viscous effects is unrealistic, as the response of the system becomes unstable. Various drag coefficients were selected to investigate the effect of the drag coefficient on the system response and power absorption. It was found that when viscosity is included in the model, the cylinder design performs the best, exceeding the power of the sphere and plate for all drag cases. While the maximum average

power was decreased in irregular waves, the same trends that appeared in the regular wave analysis were present. Again, the cylinder design performed the best. The optimal mass ratios were also decreased to approximately 20 – 25. From these results, it can be concluded that a cylindrical submerged body, where most of the total mass is from the dry mass, is the optimal shape for a two-body wave energy converter. Future work for modelling and designing a streamlined cylinder can be done to further decrease the drag coefficient, which will increase the accuracy of the model, as well as the average absorbed power.

A 1:30 scale model of the proposed WEC and PTO system, designed by Virginia Tech, was tested at the University of Maine's Alfond W2 Ocean Engineering facility. Three configurations of the 1:30 scale model were tested: a single-body (1DOF) heave only test, a two-body (2DOF) heave only test, and a six degree of freedom (6DOF) test. The purpose of the 1DOF test was to ensure that any irregularities between the experiment and the simulation could be characterized either by the PTO behavior or the WECs behavior. Here it was found that the friction internal to the PTO has a significant effect on the power. Due to the presence of friction, the measured PTO force is slightly larger than simulated, making the calculated mechanical power of the WEC larger. This power however is being absorbed by friction and decreases the power output from the generator. When designing the full-scale device, consideration of the internal PTO components must accounted for in order to maximize the efficiency of the PTO.

The experimental results of the 2DOF test matched well with the simulations results, with the exception of regular wave test M8. Here, the device performed as if the wave height was decreased while the wave period remained the same. Since M8 is a resonance point, the model will radiate a wave equal to M8's wavelength, approximately 8.8m. Since the wavelength of M8 is approximately 9m, the dimension of the wave tank, a standing wave could be generated, affecting the wave height at the model. While it is not possible to determine if this is the case, the simulation is in agreement that the wave height at the model has been affected for this particular wave period. Future simulation work to characterize this reduction in wave height is suggested, especially the modeling of the side walls test the hypothesis of a standing wave. Results from the 2DOF test show that the two-body WEC can produce twice the power of the single-body WEC.

The powers of the 6DOF test were very similar to the 2DOF test. The efficiencies of the 6DOF test are lower however. Due to moments (roll, pitch and yaw) induced on the device, the PTO push rods will have increased torsion, leading to misalignment, and finally increased friction. For full-scale development, careful consideration of the PTO design is needed to prevent misalignment while making sure the device is not over-constrained. Future work in simulating 6DOF is necessary to accurately model and predict the moments induced on the device. A dynamic model that includes the shear stresses on the different components will be helpful in characterizing the inefficiencies.

While regular wave tests are insightful to characterize resonance conditions and sources of inefficiencies, they do not provide an accurate depiction of real sea waves, which are typically very irregular due to the irregularity of the wind energy. From these tests, we saw both the floating buoy and submerged body follow the wave quite well and will exceed the given wave height often, meaning the WEC responds well to irregular seas. These results are in good agreement with our simulated results, indicating our irregular wave model is accurate. Results from the irregular tests show that the two-body WEC can produce 30% more power from waves than a single-body WEC.

References

[1] United Nations. (2015). UN and climate change: http://www.un.org/climatechange/

[2] REN21. (2017) *Renewables 2017 Global Status Report*, Paris.

[3] EIA. (2017) *Electric Power Monthly with Data for June 2017*, US.

[4] Ross, D. (1995). Power from the waves. Oxford: Oxford University Press

[5] Stoutenburg, E. D., Jenkins, N., & Jacobson, M. Z. (2010). "Power output variations of co-located offshore wind turbines and wave energy converters in California". Renewable Energy, 2781-2791.

[6] OES (Ocean Energy Systems). (2011). An international vision for ocean energy.

[7] EPRI (Electric Power Research Institute). (2011). Mapping and assessment of the United States ocean wave energy resource. Palo Alto, CA.

[8] Thorpe, T. W. (1999). "An overview of wave energy technologies: status, performance and costs". Wave Power: moving towards commercial viability. 26: 50-120.

[9] Clark, R. W. (1977), Edison: *The man who made the future*. Macdonald and Jane's, London.

[10] Smith, C. D. (2006), Palestine and the Arab-Israeli Conflict, New York: Bedford, 329.

[11] Eadie, A. (29 April 1976). Official Report (Hansard). 910, 150-1. HMSO, London

[12] Falcão, A. (2010). "Wave energy utilization: A review of the technologies". Renewable and Sustainable Energy Reviews, 899-918.

[13] Mehlum, E. (1986). Tapchan. In D. V. Evans, Hydrodynamics of Ocean Wave-Energy Utilization. Heidelberg: Spring-Verlag Berlin.

[14] Boyle, Godfrey ed. (2012). Renewable Energy: Power for a Sustainable Future (3rd ed.). Oxford: Oxford University Press and Open University.

[15] Wells, A. A. (1976). Fluid driven rotary transducer. British patent spec, 1:595-700.

[16] OpenEI. (2013, September 13). Marine and Hydrokinetic Technology Glossary. Retrieved from OpenEI: https://openei.org/wiki/Marine_and_Hydrokinetic_Technology_Glossary

[17] Budal, K., Falnes, J. (1975). “A resonant point absorber of ocean-wave power”. Nature. 256: 478-479)

[18] Falnes, J. (1999) “Wave-energy conversion through relative motion between two single-mode oscillating bodies,” ASME OMAE, 121:32-38.

[19] Neary, V. S., Presvisic, M., Jepsen, R. A., Lawson, M. J., Yu, Y.-H., Copping, A. E., . . . Murray, D. K. (2014). *Methodology for design and economic analysis of marine energy conversion (MEC) technologies*. Albuquerque: Sandia National Laboratories.

[20] Ocean Power Technologies (OPT). (2016). PowerBuoy: http://www.oceanpowertechnologies.com

[21] Mouwen, F. (2008). Presentation on Wavebob to Engineers Ireland, Wavebob.

[22] Li, Y., Yu, Y. (2012). “A synthesis of numerical methods for modeling wave energy converter-point absorbers”. Renewable and Sustainable Energy Reviews, 4352-4364.

[23] Pierson, W. J., Moskowitz, L. (1964). “A proposed spectral form for fully developed wind seas based on the similarity theory of S. A. Kitaigorodskii”. Journal of Geophysical Research, 5181-5190.

[24] World Meteorological Organization (WMO). (1998). *Guide to wave analysis and wave forecasting*, Geneva.

[25] Tucker, M. J., & Pitt, E. G. (2001). Waves in Ocean Engineering, Volume 5. UK: Elsevier Science.

[26] Chakrabarti S., (1987). Hydrodynamics of Offshore Structures. WIT Press.

[27] Le Mehaute, B. (2013). An introduction to hydrodynamics and water waves. Springer.

[28] Dean, R. G. (1970). “Relative validities of water wave theories”. Journal of the Waterways, Harbors and Coastal Engineering Division, 105-119.

[29] Ferri, F., Mejlhede, M., Pecher, A. (2013). “Validation of a wave-body interaction model by experimental tests”. Proceedings of the twenty-third International Offshore and Polar Engineering, ISOPE, 500-507.

[30] Hedges, T. (1995). “Regions of validity of analytical wave theories”. ICE Proceedings Water Maritime and Energy, 111-114.

[31] Dean, R. G., Dalrymple, R. A. (1991). Water Wave Mechanics for Engineers and Scientists, Volume 2. World Scientific.

[32] Falnes J., (2002). Ocean Waves and oscillating systems, linear interactions including wave-energy extraction. Cambridge University Press.

[33] WAMIT. (2016) User Manual V7.2. WAMIT, Inc., Massachusetts.

[34] MultiSurf. (2011). User Manual V8.0. AeroHydro, Inc., Southwest Harbor.

[35] Evans, D. V. (1976). "A theory for wave-power absorption by oscillating bodies". Journal of Fluid Mechanics, 77:1-25.

[36] Mei, C. C. (1976). "Power extraction from water waves". Journal of Ship Research, 20:63-66.

[37] Wu, B., Wang, X., Diao, X., Peng, W., Zhang, Y. "Response and conversion efficiency of two degrees of freedom wave energy device". Ocean Engineering, 76:10-20.

[38] Beatty, S., Hall, M., Buckham, B., Wild, P., Bocking, B. (2015). "Experimental and numerical comparisons of a self-reacting point absorber wave energy converters in regular waves," Ocean Engineering, 104: 370–386.

[39] Zhang, X., Yang, J., Xiao, L. (2016). "An oscillating wave energy converter with nonlinear snap-through power-take-off systems in regular waves". China Ocean Engineering, 30:565-580.

[40] Parks, P. C. (1980). "Wedges, plates and waves – some simple mathematical models of wave power machines". Power from Waves, 251-285. Academic Press.

[41] Korde, U. A. (1999). "On providing a reaction for efficient wave energy absorption by floating devices". Applied Ocean Research, 21:235-248.

[42] Korde, U. A. (2003). "Systems of reactively loaded coupled oscillating bodies in wave energy conversion". Applied Ocean Research, 25:79-91.

[43] Lefeuvre, E., Audigier, D., Richard, C., Guoymar, D. (2007). "Buck-boost converter for sensorless power optimization of piezoelectric energy harvester". IEEE Trans. Power Electron, 22:2018-2025.

[44] Tan, X., Zuo, L. (2012). "Simultaneous energy harvesting and vibration control of structures with tuned mass dampers". J. Intell. Mater. Syst. Struct., 23:2117-2127.

[45] Liu, Y., Lin, C. C., Parker, J. Zuo, L. (2016). "Exact H2 optimal tuning and experimental verification of energy-harvesting series electromagnetic tuned-mass dampers". Journal of Vibrations and Acoustics.

[46] Dow, W. G. (1937). Fundamentals of Engineering Electronics. Wiley, New York.

[47] H. K. Trabish (2010) “Wavebob is ready to make wave energy”. Green Tech Media. https://www.greentechmedia.com/articles/read/wavebob-is-ready-to-make-wave-energy

[48] WEC-Sim (Wave Energy Converter SIMulator). (2017). National Renewable Energy Laboratory (NREL) and Sandia National Laboratories. https://wec-sim.github.io/WEC-Sim/index.html

[49] WaveDyn. (2017). DNV-GL. https://www.dnvgl.com/services/wavedyn-3800.

[50] ANSYS Aqwa. (2017). ANSYS. https://www.ansys.com/products/structures/ansys-aqwa.

[51] OrcaFlex. (2016). Orcina. https://www.orcina.com/softwareproducts/orcaflex.

[52] Cummins, W. E. (1962). “The impulse response function and ship motions”. David Taylor Model Basin.

[53] Payne, G. (2008). “Guidance for the experimental tank testing of wave energy converters”. SuperGen Marine.

[54] Qualisys. (2017). Qualisys. https://www.qualisys.com.

[55] Wave Energy Prize. (2016). “Wave Energy Prize Rules”. U.S. Department of Energy.

[56] Li, Z., Zuo, L., Kuang, J., Luhrs, G. (2013). “Energy-harvesting shock absorber with a mechanical motion rectifier”. Smart Materials and Structures.

[57] Butterworth, S. (1930). “On the theory of filter amplifiers”. Experimental Wireless and Wireless Engineer, 7:536-541.

[58] Li, X., Liang, C., Boontanom, J., Martin, D., Ngo, K., Parker, R., Zuo, L. (2017). “Design, fabrication and testing of wave energy converters (WECs) using different power take-off with mechanical motion rectifier”. 12th European Wave and Tidal Energy Conference Series.

[59] Babarit, A. (2015) “A database of capture width ratio of wave energy converters.” Renewable Energy, 80: 610-628.

Appendix A Submerged Body Hydrodynamics

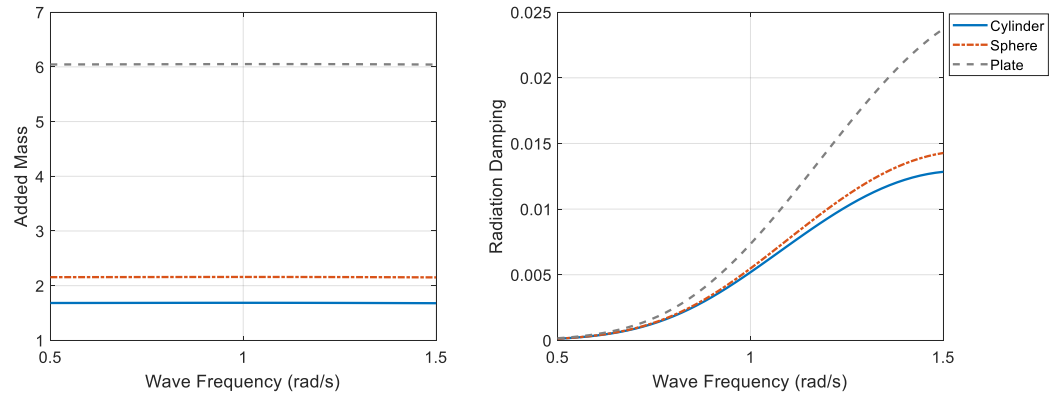

Figure A.0.1 Heave induced non-dimensional added mass and radiation damping coefficients on the submerged body. The mass ratio for these shapes are kept at 26.

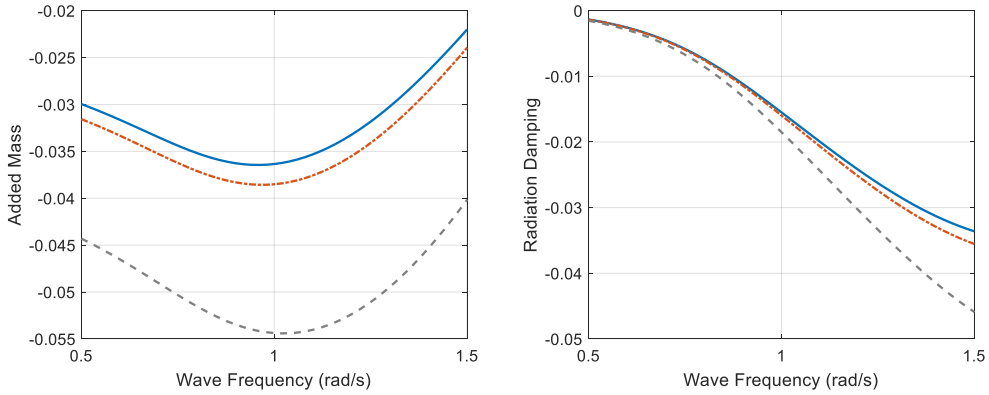

Figure A.0.2 Heave induced non-dimensional cross coupled added mass and radiation damping coefficients between the top buoy and submerged body. The mass ratio for these shapes are kept at 26.

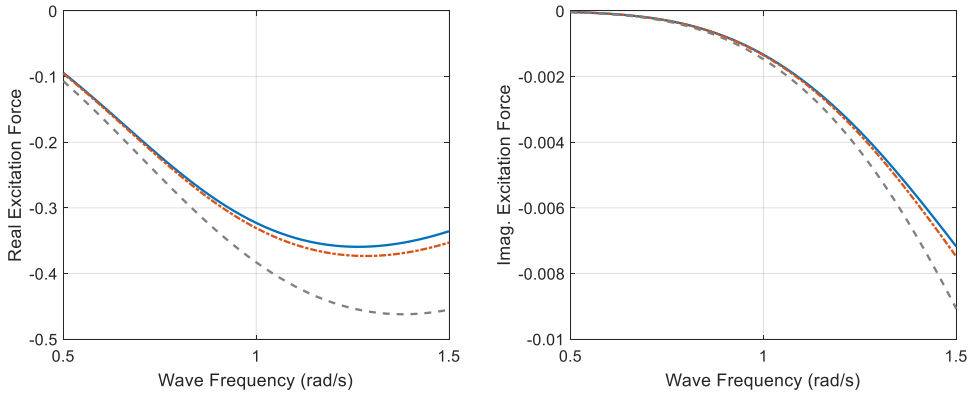

Figure A.0.3 Heave induced non-dimensional excitation force components on the submerged body. The mass ratio for these shapes are kept at 26.

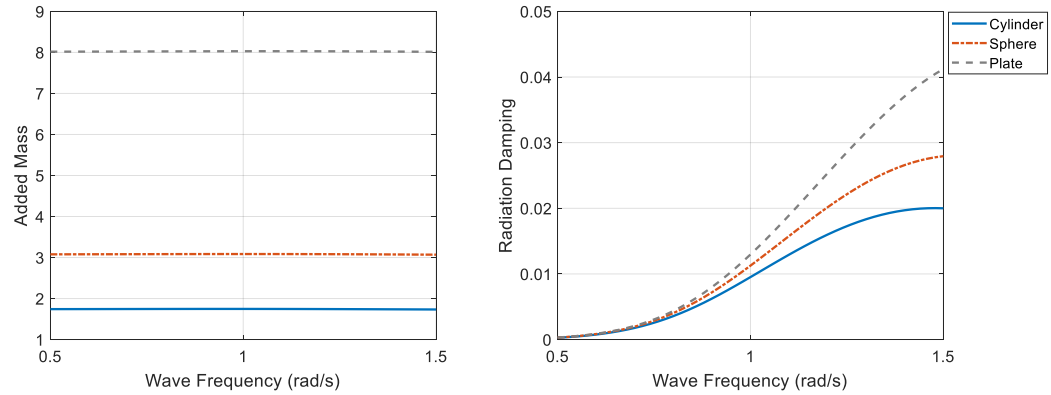

Figure A.0.4 Heave induced non-dimensional added mass and radiation damping coefficients on the submerged body. The mass ratio for these shapes are kept at 37.

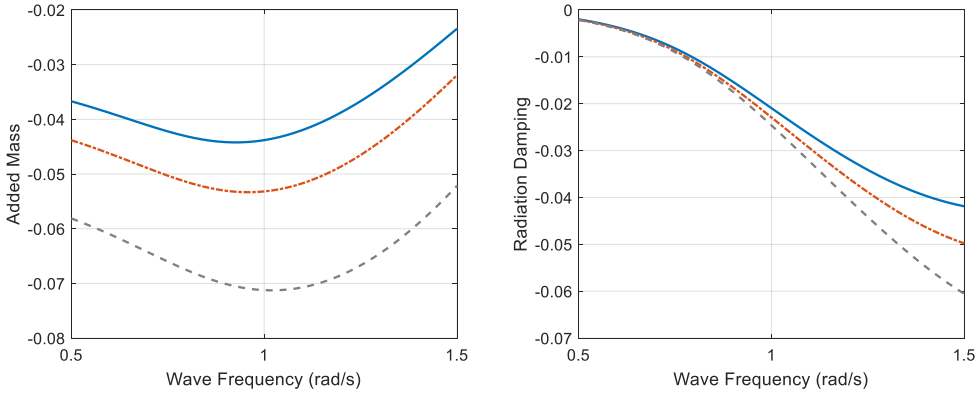

Figure A.0.5 Heave induced non-dimensional cross coupled added mass and radiation damping coefficients between the top buoy and submerged body. The mass ratio for these shapes are kept at 37.

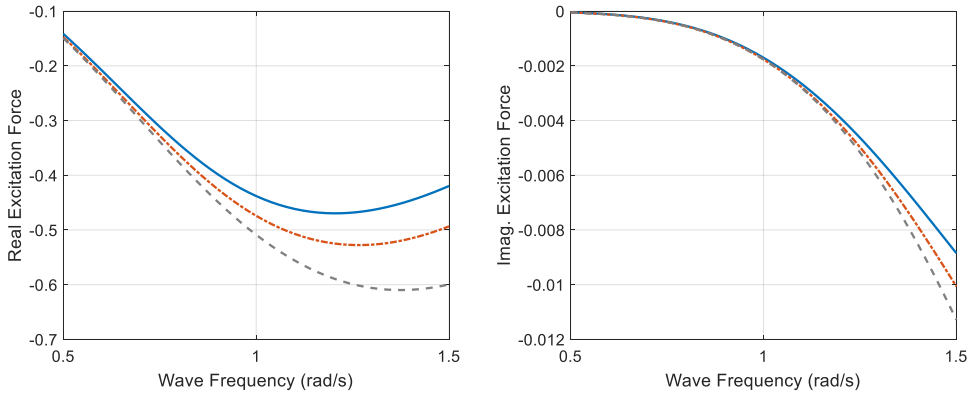

Figure A.0.6 Heave induced non-dimensional excitation force components on the submerged body. The mass ratio for these shapes are kept at 37.

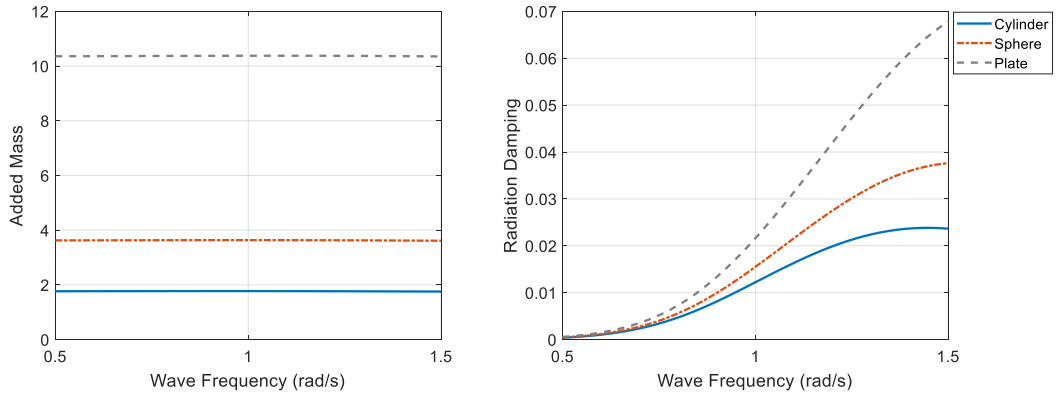

Figure A.0.7 Heave induced non-dimensional added mass and radiation damping coefficients on the submerged body. The mass ratio for these shapes are kept at 44.

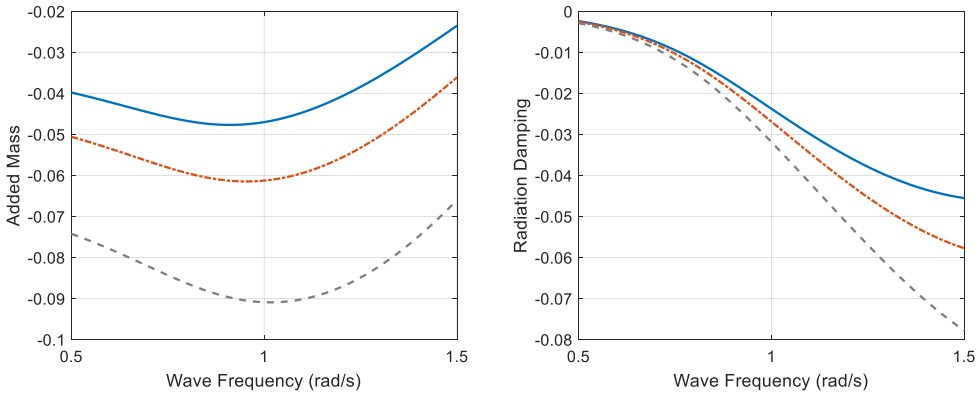

Figure A.0.8 Heave induced non-dimensional cross coupled added mass and radiation damping coefficients between the top buoy and submerged body. The mass ratio for these shapes are kept at 44.

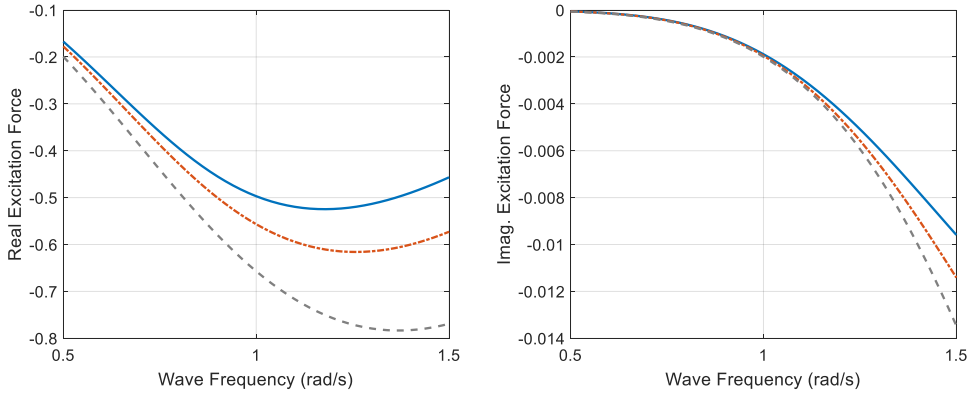

Figure A.0.9 Heave induced non-dimensional excitation force components on the submerged body. The mass ratio for these shapes are kept at 44.